WASHINGTON UNIVERSITY

Department of Physics

Dissertation Committe:

Willem H. Dickhoff, Chairperson
Claude Bernard
Thomas J. Bernatowicz
John W. Clark
Michael C. Ogilvie
Demetrios G. Sarantites
Lee G. Sobotka

EFFECTS OF SHORT-RANGE CORRELATIONS ON Λ DECAY IN NUCLEAR MATTER

by

Neil Joseph Robertson

A dissertation presented to the
Graduate School of Arts and Sciences
of Washington University in
partial fulfillment of the
requirements for the degree
of Doctor of Philosophy

August 2003

Saint Louis, Missouri

Acknowledgments

Before all others, I must thank Wim. For his guidance and support, but most of all for his patience. It goes without saying that this work would never have been completed without aid from him beyond his capacity as a "mere" research advisor. I was going to give Wim his own section here, but since he hates short paragraphs, I am going to run this acknowledgement together. Next after Wim, I wish to thank Lee for taking me on as a research assistant in his group and sharing his passion for physics. My fondest memories of graduate school are of the summer I spent with the radiochem group (Lee, Bob, Demetrios and Jim), and chief among my regrets is not continuing the relationship. Looking back farther, I need to give a nod to Benjamin Hatfield for suggesting that physics might be something interesting to study and to Marjorie Corcoran for teaching me quantum mechanics and confirming Benjamin's tip. I also must acknowledge Cliff Will and Carl Bender for being among the best of the many great teachers I have been fortunate enough to have, and experts at sharing some of the wonder and excitement physics has to offer. In regard to this thesis in particular, I am indebted to Angels, Assum, Brian, Chris, Libby and, of course, Wim, for laying the foundation upon which I have built. Gracias in particular to Angels and Assum for their integral contributions to the content of my thesis and their generous assistance whenever asked. Finally I wish to thank Mike Ogilvie, Claude Bernard, Tom Bernatowicz, Demetrios Sarantites, Lee Sobotka and especially John Clark for their contribution to my thesis through service on my dissertation committee.

Neil Joseph Robertson

Washington University in Saint Louis
August 2003

Contents

List of Tables

List of Figures

ABSTRACT OF THE DISSERTATION

Effects of Short-Range Correlations on Λ Decay in Nuclear Matter

by

Neil Joseph Robertson

Doctor of Philosophy in Physics

Washington University in St. Louis, 2003

Professor Willem H. Dickhoff, Chairperson

The effects of short-range correlations on the single-particle (sp) properties of a lambda hyperon in nuclear matter are investigated within the Green's function formalism. The calculated spectral function and quasi-particle parameters are qualitatively similar to those which have been observed for nucleons. The lambda spectral function, calculated for a realistic hyperon-nucleon interaction, indicates that about 15% of the sp strength is removed from the quasi-particle region to higher energy as a result of coupling to two-particle-one-hole states. This is compared to about 30% for a nucleon at the Fermi momentum in a similar calculation. A strong coupling between ΛN and ΣN states is known to be crucial for a correct determination of the lambda sp spectrum and gives rise to threshold effects in the self-energy and spectral function. It is also found to have a previously overlooked impact on the weak decay width. The primary decay mode for the lambda hyperon in a dense nuclear medium is a non-mesonic $\Lambda N \rightarrow NN$ decay. A consistent treatment of short-range correlations in the ΛN state, going beyond the customary use of a simple multiplicative correlation function, leads to a substantial increase in the decay width. In particular, it is observed that the $\Sigma N \rightarrow NN$ decay channel rises to prominence on the strength of the tensor coupling between ΛN and ΣN states. As a result, the contribution to the decay width from the strong conversion to the ΣN state prior to subsequent weak decay of the Σ increases the decay width by a factor of 2. This enhancement of the pion mediated $\Lambda N \rightarrow \Sigma N \rightarrow NN$ decay channel also limits the impact which a consideration of strange meson exchange can have on the important Γ_n/Γ_p ratio.

Chapter 1

Introduction

The ultimate goal of traditional nuclear physics is a fundamental theory describing the observed properties of atomic nuclei in terms of the constituent nucleons and their mutual interactions. There are two necessary ingredients for such a treatment; a characterization of the internuclear forces and a prescription for treating the complexities inherent in a system of many interacting particles. The strong interactions among nucleons are known to be emergent aspects of a more fundamental interplay between the constituent quarks and gluons of QCD. However, in the low-energy regime where nucleons and mesons are the observed excitations of QCD, this theory is not yet able to provide an adequate description of strong interactions. Instead, one constructs a theory of strong interactions in terms of the applicable degrees of freedom (nucleons and mesons). Such meson-exchange (and more generally, one-boson-exchange) interactions, when constrained by fits to low-energy nucleon-nucleon scattering, are a key ingredient in the microscopic description of nuclei. The strength of the resulting two-body interaction in turn implies the need for a non-perturbative many-body theory. The diagrammatic techniques of Green's Function Theory (GFT) are utilized in this work [1, 2].

When strangeness is considered, the entirely new branch of hypernuclear physics is open for study. The lowest mass baryon with non-zero strangeness is the lambda hyperon, essentially a heavy cousin of the neutron where a down quark has been replaced by a strange quark. Although the lambda decays weakly, its free lifetime of 260 ps is long compared with time scales for strong processes. Low production rates and short lifetimes for the hyperons make hyperon-nucleon (YN) scattering experiments difficult. Nucleon-nucleon (NN) scattering data must be used to supplement

the available data for YN scattering by invoking a broken SU(3) flavor symmetry in order to obtain a well constrained two-body interaction [3, 4, 5, 6, 7]. Limited statistics in the YN domain coupled with ambiguities in the application of SU(3) symmetries allow for significant variability in the structure of resulting YN interactions. Here a framework is developed in which the consequences of this variability for physical observables can be studied. In this work, results are based on the Nijmegen Soft-Core (NSC89) potential.

When a Λ hyperon is placed in nuclear matter it will interact with the nucleons in its environment. As a result of these strong interactions, the lambda becomes correlated with nucleons in the medium. These correlations can be accounted for in the framework of the Green's function formalism and their effects on the single-particle properties of the lambda explored. Among these effects is a net binding of the lambda in nuclear matter, and in general a new distribution of spectral strength as a result of Short-Range Correlations (SRC). Calculations of the lambda spectral strength distribution will be reported for the first time in the present work. Similar calculations of spectral functions have been performed for pure nuclear matter [8, 9, 10]. The addition of a strange test particle opens the door to comparisons with spectral functions obtained for nucleons. The weaker YN potential is expected to result in similar but less extreme modifications to the spectral distribution. However, the presence of the Λ hyperon also requires consideration of its heavier sibling, the isospin one Σ hyperon. The two hyperons have a small enough mass difference that a coupled channel problem must be solved. This is a change from the situation in pure nuclear matter, where it is permissible to ignore the effect of the Δ isobar on nucleon propagation at low energy. As a result of this channel coupling, new structure arises in the lambda spectral function.

Ultimately, the fate of the lambda in the nuclear medium is a weak decay. For heavy nuclei and their extrapolation to infinite nuclear matter, the dominant decay mode is the non-mesonic $\Lambda N \rightarrow NN$ decay [11, 12, 13, 14]. This decay has been studied by various authors both experimentally and theoretically. The handful of decay observables (partial widths, asymmetries) have varying levels of sensitivity to the particulars of Λ-N correlations. To date the experimental total decay width has been reasonably well reproduced by a number of theoretical models, but a particular ratio of partial decay channels, $\Gamma_{\Lambda n \rightarrow nn}/\Gamma_{\Lambda p \rightarrow np}$, remains a puzzle. A number of

theoretical models and experimental improvements have been suggested to resolve this dilemma, with no satisfactory solution.

The strength of the present work lies in its detailed treatment of the strong correlations experienced by a lambda during its brief lifetime of propagation in the nuclear medium prior to decay. The GFT formalism allows effective weak interactions incorporating the essential features of SRC to be constructed simply and consistently. This focus on the effects of SRC in the ΛN initial state leads to consideration of a decay mode which is typically overlooked in studies of lambda non-mesonic decay. Inclusion of the strong $\Sigma N \to NN$ decay mode serves to heighten sensitivity of the lambda's non-mesonic decay parameters to SRC.

Chapter 2 lays out the formalism used in this work. The single-particle propagator and spectral function are defined within GFT. Approximations to Dyson's equation are discussed. Input potentials and particle spectra required for the calculation are presented.

Chapter 3 presents results for the lambda spectral function. A connection is forged between the self-energy and the density of 2p1h states. Quasi-particle parameters are discussed and compared to what is found in the literature for the nucleon. Structure at the ΣN threshold and the origin of the high energy tail to the spectral function are briefly discussed.

Chapter 4 begins discussion of the weak decay. A utilitarian approximation for the non-mesonic decay width is presented. The pion-exchange potential is discussed in order to derive matrix elements for $\Sigma N \xrightarrow{\pi} NN$ transitions. The influence of vertex form factors is briefly discussed.

Chapter 5 continues treatment of the weak decay. Simple correlation functions, as typically found in the literature, are treated. Results for more complicated initial-state correlations are then presented, including decays from intermediate ΣN states. Decays of mesons heavier than the pion are discussed, with an emphasis on how they impact the Γ_n/Γ_p ratio.

Finally, Chapter 6 offers some avenues for further pursuit of topics covered by, and complementary to, this thesis.

Chapter 2

Formalism

The propagator, also called the Green's function, characterizes the excitation spectrum of a particle (or hole) created on top of the many-body ground state. For the purposes of this work, the many-body system is the ground state of Nuclear Matter (NM) [1] and the test particle of interest is the Λ hyperon.

The propagator formalism possesses features which make it especially useful for treating many-body systems consistently at various levels of approximation. Average single-particle observables as well as two-particle (tp) correlations can be extracted via the propagator formalism without the need to directly compute a many-body wavefunction. Within the framework of this theory a hierarchy of approximations exist which describe the physics with successive degrees of sophistication. The Hartree-Fock approximation is encompassed as well as other approximations more appropriate for systems (such as nuclei) which possess highly collective excitations and/or exhibit strong Short-Range Correlations (SRC).

2.1 The single-particle propagator

The single-particle (sp) propagator is defined by [2],

$$g(\alpha,\beta;t-t') \equiv -i\langle\psi_0^N \mid T[a_\alpha(t)a_\beta^\dagger(t')] \mid \psi_0^N\rangle \tag{2.1}$$

[1] An idealization of a real nucleus. The coulomb interaction is ignored, surface effects are ignored and N=Z.

where T is the time ordering operator and $a^\dagger_\beta(t')$ and $a_\alpha(t)$ are, respectively, Heisenberg creation and annihilation operators. These operators act to create (destroy) baryons on top of the exact N-body NM ground state, which is denoted by ψ^N_0, and is assumed normalized to unity. The dynamics is governed by a Hamiltonian, $\hat{H}$.

$$\hat{H} \mid \psi^N_0\rangle = E_0 \mid \psi^N_0\rangle. \tag{2.2}$$

For purposes of this work, the Hamiltonian may be considered as the sum of two parts,

$$\hat{H} \equiv \hat{H}_0 + \hat{H}_I. \tag{2.3}$$

The first term, $\hat{H}_0$, is a strictly one-body operator which may consist of optional sp potentials for each baryon species in addition to the kinetic energy component. The second term, $\hat{H}_I$, incorporates any two-body interactions. It is assumed that NM at saturation density is at sufficiently low density that three-body and higher forces are weak [15]. The labels α and β on the creation (annihilation) operators of Eq. (2.1) refer to the complete set of quantum numbers necessary for specifying the baryon sp states. It is natural to choose these sp states to be eigenstates of $\hat{H}_0$,

$$\hat{H}_0 \mid \phi^N_\alpha\rangle = \varepsilon_\alpha \mid \phi^N_\alpha\rangle. \tag{2.4}$$

In the case of a finite system, such as a real nucleus or hypernucleus, the kinetic energy operator, $\hat{T}$, does not share the natural spatial symmetry of the physical system. Under these circumstances, it is important to include an appropriate sp potential in the definition of $\hat{H}_0$ to ensure that the sp basis respects all important physical symmetries. All calculations in this work are performed in NM, which poses no particular symmetry constraint, so the choice of $\hat{H}_0 = \hat{T}$ is sufficient.

The origin of the term "propagator" becomes clear if Eq. (2.1) is rewritten as

$$\begin{aligned} g(\alpha,\beta;t-t') &= -i\langle\psi^N_0 \mid e^{i\hat{H}t}a_\alpha e^{-i\hat{H}(t-t')}a^\dagger_\beta e^{-i\hat{H}t'} \mid \psi^N_0\rangle\theta(t-t') \\ &+ i\langle\psi^N_0 \mid e^{i\hat{H}t'}a^\dagger_\beta e^{-i\hat{H}(t'-t)}a_\alpha e^{-i\hat{H}t} \mid \psi^N_0\rangle\theta(t'-t), \end{aligned} \tag{2.5}$$

where a step function implementation of the time ordering operator has been introduced as well as the explicit time dependence of the Heisenberg creation (annihilation)

operators

$$a_\alpha(t) = e^{i\hat{H}t} a_\alpha e^{-i\hat{H}t} \tag{2.6}$$

$$a^\dagger_\beta(t') = e^{i\hat{H}t'} a^\dagger_\beta e^{-i\hat{H}t'}. \tag{2.7}$$

The first term of Eq. (2.5) may be analyzed as a series of events, each admitting a simple physical interpretation. First, it should be noted that ψ_0^N already denotes a very complex state of correlated nucleons. At time t, a particle in the sp state α is added to this NM ground state. From t to t', the system evolves according to $\hat{H}$. During this interval, the test particle propagates through the nuclear medium, interacting with all of the constituent particles. As a result of these interactions, the test particle will become correlated with the medium particles. This correlation takes the form of a "dressing" as particle-hole excitations are induced. Finally, at time t', the overlap is taken between the correlated state which has evolved and a state in which a particle has been added to the NM ground state in a sp state β. The second term of Eq. (2.5) has a similar interpretation as the evolution of the NM groundstate when a particle is removed (hole added).

2.1.1 The Lehmann representation

The propagator may be cast in a more convenient form by Fourier transforming to the energy representation. To affect this transformation, complete sets of Hamiltonian eigenstates for the $N+1$ and $N-1$ particle systems are introduced

$$\hat{H} \mid \psi_n^{N+1}\rangle = E_n^{N+1} \mid \psi_n^{N+1}\rangle \tag{2.8}$$

$$\hat{H} \mid \psi_m^{N-1}\rangle = E_m^{N-1} \mid \psi_m^{N-1}\rangle \tag{2.9}$$

as well as an integral representation of the step function

$$\theta(t-t') = i \int \frac{d\omega'}{2\pi} \frac{e^{-i\omega'(t-t')}}{\omega' + i\eta}. \tag{2.10}$$

The resulting form of the propagator

$$g(\alpha,\beta;\omega) = \sum_n \frac{\langle \psi_0^N \mid a_\alpha \mid \psi_n^{N+1}\rangle\langle \psi_n^{N+1} \mid a^\dagger_\beta \mid \psi_0^N\rangle}{\omega - (E_n^{N+1} - E_0^N) + i\eta}$$

$$+ \quad \sum_m \frac{\langle \psi_0^N \mid a_\beta^\dagger \mid \psi_m^{N-1} \rangle \langle \psi_m^{N-1} \mid a_\alpha \mid \psi_0^N \rangle}{\omega - (E_0^N - E_m^{N-1}) - i\eta} \tag{2.11}$$

is known as the Lehmann (or spectral) representation [16]. Excitation energies for the particles and holes may be defined relative to the N particle ground state using $\omega' \equiv E_n^{N+1} - E_0^N$ in the first term of Eq. (2.11) and $\omega' \equiv E_0^N - E_m^{N-1}$ in the second.

Specializing to the case of an infinite number of particles, a specific choice of basis is made. From this point forward, the sp states are taken to be eigenstates of $\hat{H}_0 = \hat{T}$,

$$\mid \alpha \rangle \equiv \mid \vec{k}\, s m_s\, t m_t \rangle, \tag{2.12}$$

and the label, α, will be shorthand for momentum, spin and isospin quantum numbers. These states are also eigenstates of the full hamiltonian, $\hat{H}$, and the symmetry of the system makes the sp propagator diagonal on this basis,

$$g(\alpha, \beta; \omega) = \delta_{\alpha\beta} g(\alpha, \alpha; \omega) \equiv \delta_{\alpha\beta} g(\alpha; \omega). \tag{2.13}$$

The energy spectrum becomes continuous and the sums over states in Eq. (2.11) become integrals, transforming Eq. (2.11) to

$$g(\alpha; \omega) = \int_{\varepsilon_F}^{\infty} d\omega' \frac{S_p(\alpha; \omega')}{\omega - \omega' + i\eta} + \int_{-\infty}^{\varepsilon_F} d\omega' \frac{S_h(\alpha; \omega')}{\omega - \omega' - i\eta}. \tag{2.14}$$

The fermi energy, ε_F, has been introduced in Eq. (2.14) as the lowest energy above the ground state at which a particle may be added

$$\varepsilon_F \equiv E_0^{N+1} - E_0^N \approx E_0^N - E_0^{N-1}. \tag{2.15}$$

The spectral functions have also been introduced as

$$S_p(\alpha; \omega') \equiv \mid \langle \psi_n^{N+1} \mid a_\alpha^\dagger \mid \psi_0^N \rangle \mid^2 \frac{dn}{d\omega'} \tag{2.16}$$

$$S_h(\alpha; \omega') \equiv \mid \langle \psi_m^{N-1} \mid a_\alpha \mid \psi_0^N \rangle \mid^2 \frac{dm}{d\omega'} \tag{2.17}$$

for the particles and holes respectively. The factors $dn/d\omega'$ and $dm/d\omega'$ weight each term according to the density of states at an excitation energy of ω'. The particle spectral function (Eq. (2.16)) denotes the probability density that a particle added

to the NM groundstate, ψ_0^N, in a sp state α, with an excitation energy ω', will be in the nth eigenstate of the $N+1$ particle system. Likewise, Eq. (2.17) describes the corresponding situation where a particle is removed. As a probability density, the spectral function is real and positive. A particle (hole) occupation number may be defined for a state α as the integrated strength above (below) the fermi energy,

$$n_p(\alpha) \equiv \int_{\varepsilon_F}^{\infty} d\omega' S_p(\alpha;\omega') \tag{2.18}$$

$$n_h(\alpha) = \int_{-\infty}^{\varepsilon_F} d\omega' S_h(\alpha;\omega') \tag{2.19}$$

The total spectral strength is normalized in such a way that

$$\int_{-\infty}^{\infty} d\omega' S(\alpha;\omega') = n_p(\alpha) + n_h(\alpha) = 1, \tag{2.20}$$

which follows from the completeness of the energy eigenstates for the $N+1$ and $N-1$ particle systems and the anticommutation relations for the fermion operators,

$$\{a_\alpha^\dagger, a_\beta\} = \delta_{\alpha\beta}. \tag{2.21}$$

The standard integral relation,

$$\frac{1}{x \pm i\eta} = P\frac{1}{x} \mp i\pi\delta(x), \tag{2.22}$$

when applied to Eq. (2.14) yields the following algebraic relationship between the imaginary part of the propagator and the spectral function

$$\text{Im } g(\alpha;\omega) = \begin{cases} -\pi S_p(\alpha;\omega) & \omega > \varepsilon_F \\ \pi S_h(\alpha;\omega) & \omega < \varepsilon_F \end{cases}. \tag{2.23}$$

2.1.2 Example of a non-interacting particle

Unlike the general and strictly formal treatment performed to this point, an explicit functional form for the propagator can be obtained for the special case of a non-interacting particle. This example will further clarify the physical interpretation of the sp propagator and motivate use of its spectral representation. The Hamiltonian for the non-interacting system is simply $\hat{H}_0$, and its N particle groundstate will be denoted by Φ_0^N, which is simply a Slater determinant of sp states filled to a fermi

level denoted by F. The propagator (Eq. (2.5)) in this case is

$$\begin{aligned} g^0(\alpha,\beta;t-t') &= -i\langle\Phi_0^N \mid e^{i\hat{H}_0 t}a_\alpha e^{-i\hat{H}_0(t-t')}a_\beta^\dagger e^{-i\hat{H}_0 t'} \mid \Phi_0^N\rangle\theta(t-t') \\ &+ i\langle\Phi_0^N \mid e^{i\hat{H}_0 t'}a_\beta^\dagger e^{-i\hat{H}_0(t'-t)}a_\alpha e^{-i\hat{H}_0 t} \mid \Phi_0^N\rangle\theta(t'-t). \end{aligned} \tag{2.24}$$

Using

$$\hat{H}_0 \mid \Phi_0^N\rangle = E_0^N \mid \Phi_0^N\rangle, \tag{2.25}$$

Eq. (2.24) becomes

$$\begin{aligned} g^0(\alpha,\beta;t-t') &= -ie^{-iE_0^N(t-t')}\langle\Phi_0^N \mid a_\alpha e^{-i\hat{H}_0(t-t')}a_\beta^\dagger \mid \Phi_0^N\rangle\theta(t-t') \\ &+ ie^{-iE_0^N(t'-t)}\langle\Phi_0^N \mid a_\beta^\dagger e^{-i\hat{H}_0(t'-t)}a_\alpha \mid \Phi_0^N\rangle\theta(t'-t). \end{aligned} \tag{2.26}$$

The great simplification in this example of the non-interacting propagator occurs because the state $a_\beta^\dagger \mid \Phi_0^N\rangle$ is an exact eigenstate of the $N+1$ particle system;

$$\hat{H}_0 a_\beta^\dagger \mid \Phi_0^N\rangle = \theta(\beta-F)(E_0^N+\varepsilon_\beta)a_\beta^\dagger \mid \Phi_0^N\rangle. \tag{2.27}$$

Likewise, $a_\alpha \mid \Phi_0^N\rangle$ is an eigenstate of the $N-1$ particle system. This is not true for the much richer and more complex case of a system of interacting particles. Using Eq (2.21) and the fact that Φ_0^N is normalized to unity, the propagator reduces to the compact form

$$g^0(\alpha,\beta;t-t') = -i\delta_{\alpha\beta}\theta(\alpha-F)e^{i\varepsilon_\alpha(t-t')}\theta(t-t') + i\delta_{\alpha\beta}\theta(F-\alpha)e^{i\varepsilon_\alpha(t'-t)}\theta(t'-t). \tag{2.28}$$

The propagator of Eq (2.28) depends only on the energy of the sp state and is independent of details of the medium except for the presence of the Pauli θ-function which serves to distinguish between particle and hole states. Transforming to the energy representation yields the simple expression

$$g^0(\alpha;\omega) = \frac{\theta(\alpha-F)}{\omega-\varepsilon_\alpha+i\eta} + \frac{\theta(F-\alpha)}{\omega-\varepsilon_\alpha-i\eta}. \tag{2.29}$$

The poles of the sp propagator determine allowed excitation energies of the system containing an additional particle (or hole). For the non-interacting case, $g^0(\alpha;\omega)$ contains only a simple pole at an excitation energy corresponding to the energy of

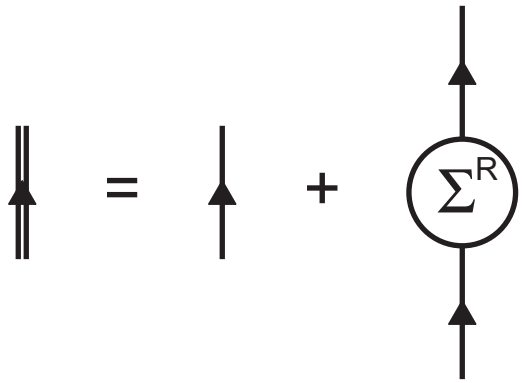

Figure 2.1: Dressed Λ propagator in terms of the reducible self-energy.

the sp state. The spectral function (Eq. (2.23)) for the non-interacting case is

$$S_p^0(\alpha;\omega) = \theta(\alpha - F)\delta(\omega - \varepsilon_\alpha) \quad (2.30)$$

$$S_h^0(\alpha;\omega) = \theta(F - \alpha)\delta(\omega - \varepsilon_\alpha). \quad (2.31)$$

Eq. (2.30) indicates, very intuitively, that a non-interacting particle may be added to the medium in a sp state α, with unit strength, at an energy corresponding to ε_α, and not at any other energy. The addition of strong interactions amongst the particles, which induce correlations, changes this picture. The dressed propagator will have a more complex analytic structure as a function of energy, which gives rise to a correspondingly rich structure in the spectral function.

2.1.3 Dyson's equation

At this point, the propagator has been manipulated into a form (the Lehmann representation) which permits a ready physical interpretation and will be useful for understanding the effects of interactions on the sp properties of a particle (or hole). It remains to connect this formal expression to known quantities in a manner which admits a tractable calculation. This task is accomplished by performing a perturbative expansion of the interacting propagator, Eq. (2.1), in terms of the explicitly known form of the non-interacting propagator, Eq. (2.29). The result is an infinite sum of terms, including all orders in the interparticle interactions contained in $\hat{H}_I$ [1]. The infinite series of terms in the propagator expansion is perhaps best visualized with the aid of Feynman diagrams. The diagrams of Fig. 2.1 correspond to the equation

$$g(\alpha;\omega) = g^0(\alpha;\omega) + g^0(\alpha;\omega)\Sigma^R(\alpha;\omega)g^0(\alpha;\omega), \tag{2.32}$$

and introduce the reducible self-energy, Σ^R, which contains all of the interaction terms which "dress" the test particle as it propagates through the medium. A representative collection of the many parts which comprise the reducible self-energy is displayed in Fig. 2.2. The diagrams may be divided into two classifications. The irreducible self-energy, Σ, encompasses all diagrams which cannot be split into two pieces by breaking a single propagator line (all except parts b and f of Fig. 2.2). The other diagrams are really just iterations of the irreducible self-energy diagrams, and the entire propagator expansion, Fig. 2.1, can be resummed, Fig. 2.3, in terms of the irreducible self-energy. It is this compact expression in terms of the irreducible self-energy which is the direct diagrammatic analog of

$$g(\alpha;\omega) = g^0(\alpha;\omega) + g^0(\alpha;\omega)\Sigma(\alpha;\omega)g(\alpha;\omega), \tag{2.33}$$

known as Dyson's equation.

Using the explicit form of the non-interacting propagator from Eq. (2.29), the Dyson equation may be solved algebraically [2] to yield

$$g(\alpha;\omega) = \frac{1}{\omega - \varepsilon_\alpha - \Sigma(\alpha;\omega)}. \tag{2.34}$$

This formal solution can be separated into particle and hole pieces for comparison with Eq. (2.29) for the non-interacting propagator,

$$g(\alpha;\omega) = \frac{\theta(\alpha - F)}{\omega - \varepsilon_\alpha - \Sigma(\alpha;\omega)} + \frac{\theta(F - \alpha)}{\omega - \varepsilon_\alpha - \Sigma(\alpha;\omega)}. \tag{2.35}$$

The only difference lies in the presence of the self-energy [3] which acts as an effective one-body potential.

$$\varepsilon_\alpha \to \varepsilon_\alpha + \Sigma(\alpha;\omega). \tag{2.36}$$

The self-energy incorporates an infinite number of terms, including all orders in the two-body interaction. A truncation of the self-energy series at some finite order in the interaction is not a viable option for the strong interactions commonly used in nuclear

[2] This simplification is a byproduct of working in an infinite system where the irreducible self-energy is diagonal on the sp basis. In general, Eq. (2.33) is a matrix equation.

[3] From this point forward, the term "self-energy" will implicitly refer to the irreducible self-energy.

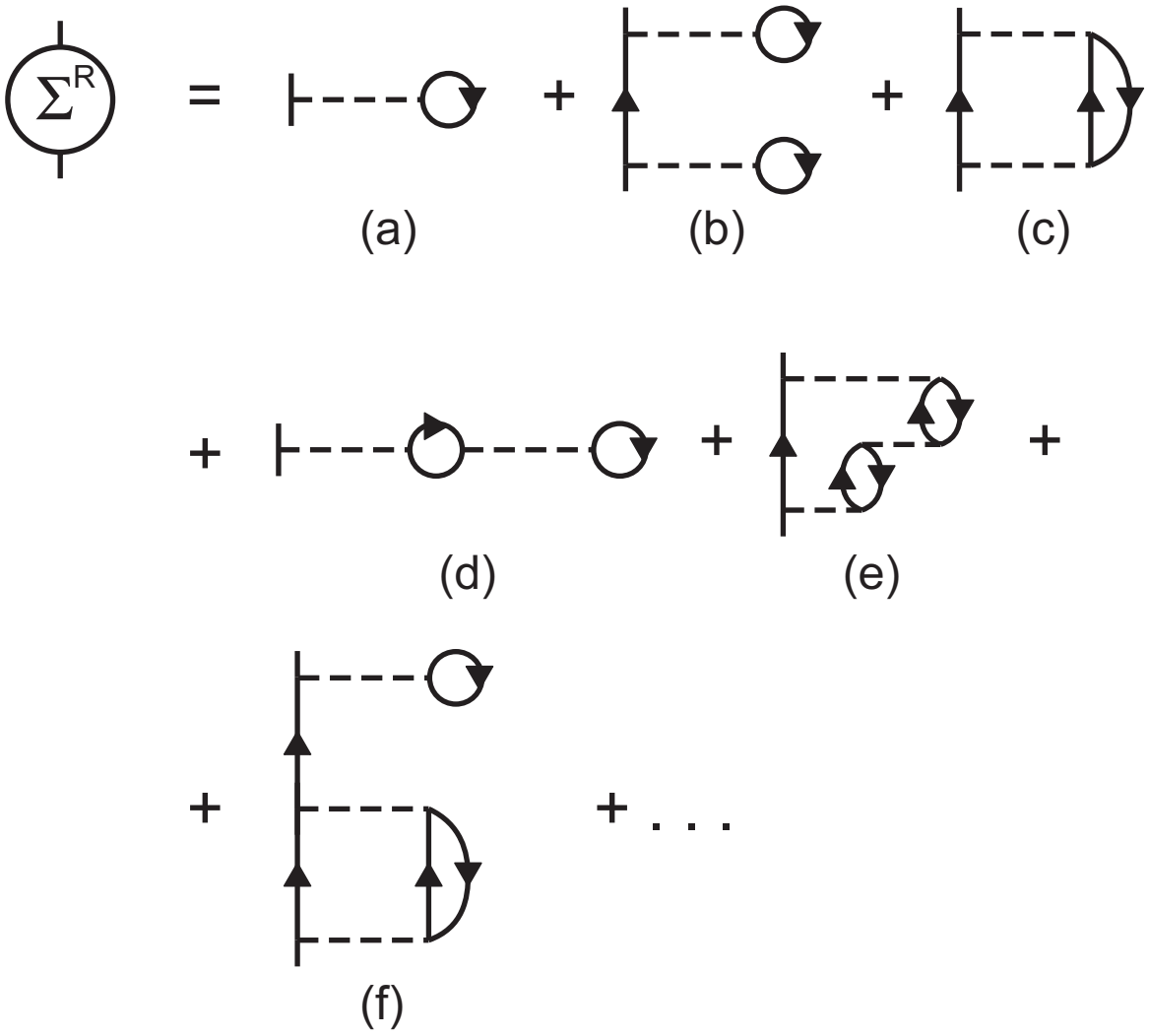

Figure 2.2: Representative collection of terms which comprise the reducible self-energy.

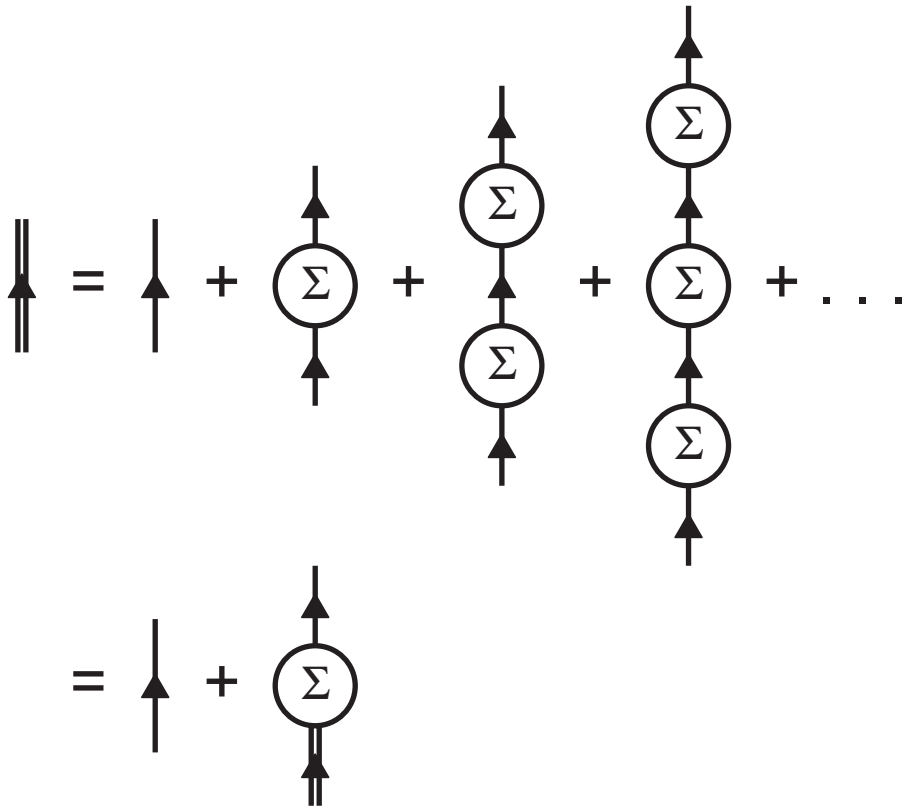

Figure 2.3: Propagator expansion in terms of the irreducible self-energy.

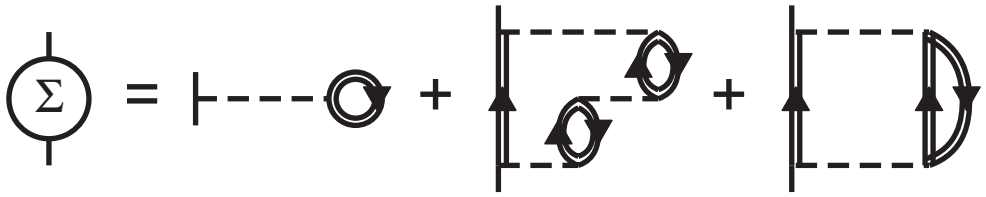

Figure 2.4: Sampling of self-energy terms, expressed with dressed propagators.

physics. The individual terms may even be divergent if interactions with hard-cores are used [17]. Instead, approximations are required which involve summing an infinite number of terms taken from those classes of diagrams deemed most important for a given calculation. The proliferation of terms may be formally reduced by another resummation, this time replacing all internal propagator lines with dressed propagators. This renormalization leaves only a few classes of diagrams in the expansion of the self-energy (Fig. 2.4).

2.2 Approximations to the Dyson equation

Although the formalism developed to this stage may be applied to a more general treatment, we specialize now to the case of a single Λ hyperon in NM. Hyperons are treated as distinct species from the nucleons which comprise the medium, so there can be no hole part to the hyperon propagator.

Every step to this point has been a formal manipulation of the propagator expansion and no approximations have been made. At this stage, each term in Fig. 2.4 is examined to ascertain its role in describing the physics of the propagating Λ-particle.

2.2.1 The Hartree-Fock approximation

The first diagram of Fig. 2.4 is the Hartree-Fock (HF) contribution to the self-energy. [4] This diagram represents the equation,

$$\Sigma_{\Lambda}^{HF}(\alpha;\omega) \;=\; \sum_{\beta} \int_{\varepsilon_F}^{\infty} \frac{d\omega'}{2\pi i} \langle \alpha\beta \mid V \mid \alpha\beta \rangle g_N^{\downarrow}(\beta;\omega') \tag{2.37}$$

[4] Typically, the HF approximation refers specifically to the case where the first term of Fig. 2.4 is the only one in the self-energy expansion. In this work, the term HF is used more generally even when the hole line is dressed (correlated HF) or to refer to the HF contribution to the self-energy in the presence of other terms.

$$= \sum_{\beta} \int_{\varepsilon_F}^{\infty} d\omega' \langle \alpha\beta \mid V \mid \alpha\beta \rangle S_N^h(\beta;\omega') \tag{2.38}$$

$$= \sum_{\beta} \langle \alpha\beta \mid V \mid \alpha\beta \rangle n_h(\beta). \tag{2.39}$$

which may be simply interpreted as an average over the interactions between the Λ and medium nucleons. A requirement of the bare YN interaction is that it provide a realistic description of free particle scattering at low energies (typically up to pion production threshold). Such an interaction will be real, violently repulsive at short range and moderately attractive at longer range. Matrix elements, taken on the uncorrelated YN basis, are on average repulsive. As a result, the HF self-energy will be real and positive, acting as a repulsive mean-field potential which shifts the Λ spectrum to

$$\varepsilon_\Lambda^{HF}(\alpha) = t_\Lambda(\alpha) + \Sigma_\Lambda^{HF}(\alpha). \tag{2.40}$$

This is not a realistic approximation in two respects.

1. Despite the strong repulsive core in realistic nuclear and hypernuclear potentials, there is a net attraction, as evidenced by the existence of bound nuclei and hypernuclei.

2. The HF approximation yields a real self-energy, which implies an Independent Particle Model (IPM). Particles occupy sp states with infinite lifetimes.

Despite its limitations, the HF approximation provides an intuitive method for generating a mean-field potential from a two-body interaction and is the simplest non-trivial approximation which allows a self-consistent treatment of the many-body problem. The deficiencies alluded to above can be overcome by replacing the bare two-body interaction, V, with an effective interaction which is both complex and has a real part which is on average attractive. An effective interaction which possesses these necessary traits may be derived from the bare interaction by going beyond the HF approximation as described in the next sections.

2.2.2 Rings and Ladders

The diagrams of Fig. 2.2 which follow the HF term (part a), are classified as Ladder diagrams (part c), Ring diagrams (part e) and diagrams which are a mixture of Rings and Ladders (not pictured). The relative importance of the various diagrams

may be determined based on the ratio, a/r_0, where a is the range of the repulsive part of the interaction and r_0 the average interparticle spacing. NM at saturation density has $a/r_0 \sim 1/3$ [1] and may be modeled as a low density, non-ideal Fermi gas. Galitskii [18] has argued that for such a system, at each order of the bare interaction, the diagrams with the fewest hole lines should dominate. For example, irreducible third-order diagrams in Fig. 2.2 each have two additional propagator lines and one more interaction line than the second-order diagrams. The third-order ring term (part e of Fig. 2.2) has one additional particle line and one more hole line. The third-order ladder term has two additional particle lines. Each propagator line implies an integral over the phase space for a particle ($k > k_F$) or hole ($k < k_F$), appropriately weighted by matrix elements of the interaction. Of course, the finite phase space for a hole is always less than the infinite phase space for a particle. It is because the integrals are weighted by matrix elements of the interaction that the combination $k_F a$ determines the relative importance of particle and hole lines.

For high-density systems, such as the electron gas where the bare Coulomb interaction has infinite range, $k_F a >> 1$, and particle-hole (ring) excitations dominate over particle-particle (ladder) excitations. The sum of ring diagrams to all orders is known as the Random Phase Approximation (RPA). For low-density systems like NM, it is the particle-particle excitations which dominate and their sum to all orders is called the Ladder Approximation (LA). To the extent that ring diagrams manifest long-range correlations, it is inappropriate to include them in a NM calculation which hopes to have relevance for finite systems. This follows from the fact that the long-range order in an infinite system is fundamentally different from that of a finite system. The effects of SRC, on the other hand, should be independent of scale and geometry and so can reasonably be expected to carry over from calculation in infinite NM to application in finite systems.

The series of Ladder diagrams defines an effective two-body interaction (Fig. 2.5a). In the limit of zero density (the interaction of two free particles) this effective interaction is just the T-matrix of scattering theory. When a nuclear medium is present, nucleon particle propagation is restricted to states above a Fermi level. If the intermediate particles are not dressed, then the effective, in-medium interaction is the Brueckner G-matrix [19]. If the intermediate propagators are dressed, this generalized version of the G-matrix will be called the Γ-matrix. Though the following discussion

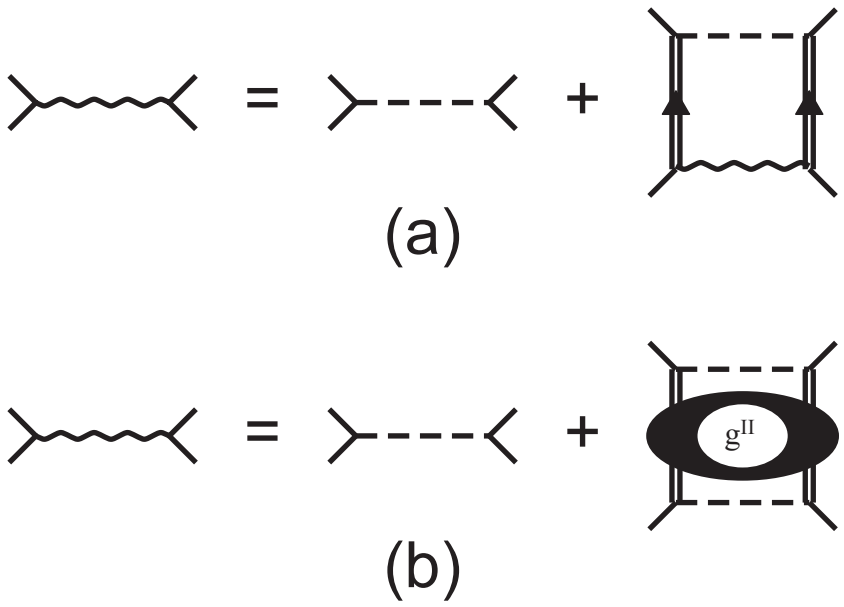

Figure 2.5: Ladder equation in terms of a) uncorrelated two particle propagator and b) correlated two particle propagator.

applies equally to the more general case of the Γ-matrix, in this work, only the simpler G-matrix form of effective interaction is used.

The Born series of ladder diagrams may be resummed in two ways (Fig. 2.5). Part (a) of Fig. 2.5 leads to an integral equation for the G-matrix in terms of V and the uncorrelated tp propagator. The particles in the intermediate state are separately dressed by interactions with the medium, but are not correlated with each other. This is the form of the G-matrix equation which will actually be solved in a subsequent section. An alternative, but entirely equivalent, resummation leads to Fig. 2.5(b). Here the G-matrix is expressed in terms of V and the correlated tp propagator. This version of the Ladder equation is useful for elucidating an important analytic property of the G-matrix. The diagrammatic expression of Fig. 2.5(b) represents

$$\langle \alpha\beta \mid G(\Omega) \mid \mu\lambda \rangle = \langle \alpha\beta \mid V \mid \mu\lambda \rangle + \sum_{\delta\gamma\eta\nu} \langle \alpha\beta \mid V \mid \delta\gamma \rangle g^{II}_{corr}(\delta\gamma, \eta\nu; \Omega) \langle \eta\nu \mid V \mid \mu\lambda \rangle. \tag{2.41}$$

The energy dependence is entirely contained in the correlated tp propagator. In direct analogy with the sp propagator development which led from the definition of Eq. (2.1)

to the Lehmann representation of Eq. (2.14), a similar procedure yields

$$g^{II}_{corr}(\delta\gamma,\eta\nu;\Omega) = \int_{\Omega_{min}}^{\infty} d\Omega' \frac{S_{pp}(\delta\gamma,\eta\nu;\Omega')}{\Omega - \Omega' + i\eta}, \tag{2.42}$$

as a Lehmann representation for the correlated tp propagator. The tp spectral density,

$$S_{pp}(\delta\gamma,\eta\nu;\Omega') \equiv \langle\psi^N_0 \mid a_\delta a_\gamma \mid \psi^{N+2}_n\rangle\langle\psi^{N+2}_n \mid a^\dagger_\eta a^\dagger_\nu \mid \psi^N_0\rangle \frac{dn}{d\Omega'} \tag{2.43}$$

has been introduced, much like the sp spectral function of Eq. (2.16). The analytic structure of the correlated tp propagator mirrors that of the sp propagator in its simplicity. In particular, the integral relation of Eq. (2.22) may be used to derive the following dispersion relation

$$g^{II}_{corr}(\delta\gamma,\eta\nu;\Omega) = \frac{-1}{\pi}\int_{\Omega_{min}}^{\infty} d\Omega' \frac{\mathrm{Im}\, g^{II}_{corr}(\delta\gamma,\eta\nu;\Omega')}{\Omega - \Omega' + i\eta}. \tag{2.44}$$

Insertion of this expression for g^{II}_{corr} into Eq. (2.41) for the G-matrix yields

$$\langle\alpha\beta \mid G(\Omega) \mid \mu\lambda\rangle = \langle\alpha\beta \mid V \mid \mu\lambda\rangle + \frac{1}{\pi}\int_{\Omega_{min}}^{\infty} d\Omega' \frac{\mathrm{Im}\langle\alpha\beta \mid G(\Omega') \mid \mu\lambda\rangle}{\Omega - \Omega' + i\eta} \tag{2.45}$$

as a dispersion relation for the G-matrix. This indicates that only the imaginary part of the G-matrix need be calculated directly (albeit for all energies) in order to completely determine the full G-matrix. Another way to view Eq. (2.45) is as a consistency check on the numerical calculation of the G-matrix.

The lambda self-energy in the LA may be compactly represented as in Fig. 2.6b. This may be compared to the HF approximation (first term in Fig. 2.4). The self-energy may still be thought of as an effective potential for the lambda generated by its average interaction with the nucleons. The difference is that the bare interaction is now replaced by the G-matrix effective interaction. The G-matrix is complex and energy dependent, satisfying the list of desirable qualities mentioned previously for an effective two-particle interaction (Section 2.2.1). In addition, it has the distinction of being derived directly in terms of the bare interaction.

The simplicity of the diagram (Fig. 2.6b) expressing the self-energy in terms of the G-matrix reflects a simple mathematical relationship between the two functions:

$$\Sigma_\Lambda(\alpha;\omega) = \sum_\beta \int_{\varepsilon_F}^{\infty} \frac{d\omega'}{2\pi i} \langle \alpha\beta \mid G(\omega+\omega') \mid \alpha\beta \rangle g_N^h(\beta;\omega'), \tag{2.46}$$

$$= \pi \sum_\beta \int_{\varepsilon_F}^{\infty} d\omega' \langle \alpha\beta \mid G(\omega+\omega') \mid \alpha\beta \rangle S_N^h(\beta;\omega'). \tag{2.47}$$

The spectral representation of the nucleon hole propagator, Eq. (2.14), was used to obtain the final expression of Eq. (2.47). Similar to the HF case, Eq. (2.39), the self-energy in the LA is just a convolution of the effective interaction with the spectral density of occupied nucleon states. Just as the G-matrix satisfies a dispersion relation, so too does the self-energy. Inserting Eq. (2.45) into Eq. (2.47) yields,

$$\Sigma_\Lambda(\alpha;\omega) = \pi \sum_\beta \int_{\varepsilon_F}^{\infty} d\omega' \langle \alpha\beta \mid V \mid \alpha\beta \rangle S_N^h(\beta;\omega')$$

$$+ \int_{\omega_{min}}^{\infty} d\omega' \frac{\mathrm{Im}\Sigma_\Lambda(\alpha;\omega)'}{\omega-\omega'+i\eta} \tag{2.48}$$

$$\Sigma_\Lambda(\alpha;\omega) = \Sigma_\Lambda^{HF}(\alpha;\omega) + \Sigma_\Lambda^{\Delta\Gamma}(\alpha;\omega). \tag{2.49}$$

2.3 Input to calculation

Having chosen the LA as a physically suitable approximation to Dyson's equation, Fig. 2.6, the framework is set for calculation of the lambda propagator. Now it is necessary to consider what inputs are required to explicitly define the calculation.

2.3.1 Bare YN and NN interactions

A major ingredient necessary for this work is the two-body interaction which describes the scattering of hyperons and nucleons. The 1989 version of the Nijmegen Soft-Core (NSC89) meson exchange potential is used [6]. This potential is the Fourier transformable, soft-core descendant of the hard-core Nijmegen D and F models [3, 4, 5]. [5] In the microscopic spirit of this work, it is based on the exchange of strange and non-strange pseudoscalar (π, η, κ) and vector (ρ, ω, κ^*) mesons. Though fit

[5] Since this work began, the NSC89 potential has been superseded by a family of potentials: NSC97 versions a-f [7].

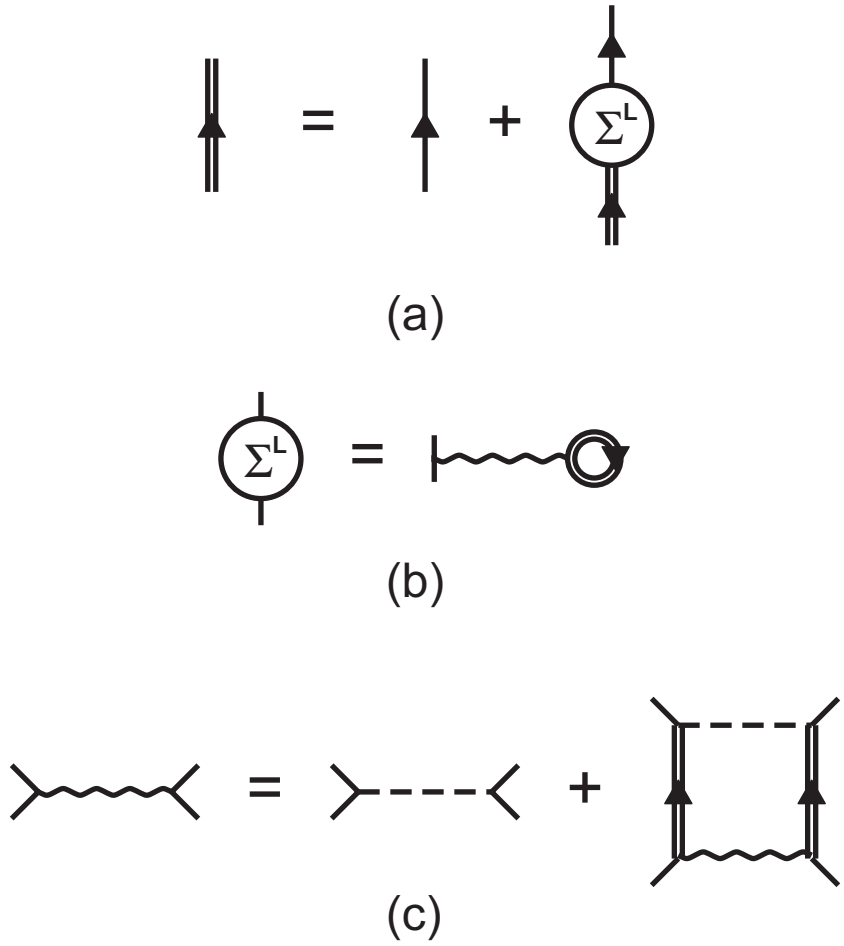

Figure 2.6: Diagrammatic representation of Dyson's equation in the Ladder approximation.

to available YN scattering data, the scarcity of such data demands a heavy reliance on SU(3) symmetries to relate poorly determined YN coupling constants to their better known NN relatives. As with all potentials of this type, the NSC89 is fit to low-energy data and its core structure is not well determined. Results which depend on the short-range behavior of the potential will reflect this deficiency but are consequently of interest as well, if they can be related to experimentally accessible quantities.

In this work comparisons are made to nucleon spectral functions derived from calculations involving the Reid Soft-Core (RSC) potential [20].

2.3.2 Nucleon propagator

The dressed nucleon hole and particle propagators appear in the self-energy equation (Fig. 2.6b) and the G-matrix equation (Fig. 2.6c) as external parameters. In principle, the dressed nucleon propagator should be determined from a coupled system of equations similar to those depicted in Fig. 2.6. The program to self-consistently calculate a nucleon propagator in NM began with Goldstone's application of diagrammatic techniques to the work of Brueckner and is ongoing [21]. In this work, the calculation is carried through with non-interacting nucleons.

2.3.3 Σ hyperon propagator

The Σ hyperon has been introduced as part of a possible YN intermediate state in the G-matrix equation (Fig. 2.6c). Its inclusion is necessitated by the relatively small mass difference of 77 MeV between the Λ and Σ. This results in a significant coupling between ΛN and ΣN intermediate states which cannot be ignored. Experimentally, the Σ is bound in heavy hypernuclei by about 10 MeV [22, 23, 11]. Compared with sp potential well depths of approximately 30 MeV for the Λ and 75 MeV for the nucleon in NM, the Σ interacts relatively weakly with the nuclear medium. For this reason, it is not too poor of an approximation to treat the Σ as a non-interacting particle as is done in this work.

$$g_\Sigma(\alpha;\omega) \to g^0_\Sigma(\alpha;\omega). \tag{2.50}$$

2.4 Self-consistency of the Λ propagator

At this point it should be noticed that although the propagator has a formal solution in terms of the self-energy, the self-energy depends internally on the dressed propagator. This means that Fig. 2.6 depicts a non-linear coupled system of equations for the dressed Λ propagator. The natural starting point is to make the zeroth order approximation

$$g_\Lambda(\alpha;\omega) \to g^0_\Lambda(\alpha;\omega). \tag{2.51}$$

Given this choice of initial Λ propagator, the G-matrix, self-energy, and next generation propagator may be calculated in turn. Ideally, we would now like to use this new propagator, $g^{(1)}_\Lambda(\alpha;\omega)$, as input to the G-matrix equation and iterate until a self-consistent solution is obtained. Examination of Eq. (2.35) reveals that the energy dependence of the dressed propagator is much more complicated than that of the free propagator, Eq. (2.29). In fact, this is already true for $g^{(1)}_\Lambda(\alpha;\omega)$, which has an analytic structure similar to that of the fully self-consistent propagator, even after only one iteration. A simplified iteration scheme is used instead.

Breaking up the self-energy into its real and imaginary parts, Eq. (2.35) for the dressed propagator can be rewritten as:

$$g_\Lambda(\alpha;\omega) = \frac{1}{[\omega - t_\Lambda(\alpha) - \text{Re }\Sigma_\Lambda(\alpha;\omega)] - i[\text{Im }\Sigma_\Lambda(\alpha;\omega)]}. \tag{2.52}$$

Comparing this to the form of the free propagator, Eq. (2.29), it can be seen that the real part of the self-energy plays the role of an energy-dependent potential. This observation motivates the definition of a new energy spectrum:

$$\varepsilon^{(1)}_\Lambda(\alpha) = t_\Lambda(\alpha) + \text{Re }\Sigma_\Lambda(\alpha;\varepsilon^{(1)}_\Lambda(\alpha)). \tag{2.53}$$

This new spectrum, which will later be identified as the quasi-particle (qp) energy spectrum, is inserted in place of the kinetic energy spectrum in Eq. (2.29), to define a new propagator

$$g^{(1)}_\Lambda(\alpha;\omega) \to \tilde{g}^{(1)}_\Lambda(\alpha;\omega) \equiv \frac{1}{\omega - \varepsilon^{(1)}_\Lambda(\alpha) + i\eta}. \tag{2.54}$$

In this way, the same simple analytic structure is always used for the lambda propagator in the G-matrix equation, and only the spectrum changes from iteration to iteration. The iteration procedure is continued until a self-consistent lambda spectrum is obtained:

$$\varepsilon_\Lambda^{(n+1)}(\alpha) = \varepsilon_\Lambda^{(n)}(\alpha). \tag{2.55}$$

It is important to calculate such a consistent spectrum in order to ensure that the final spectral function is a continuous function of energy.

2.4.1 Spectral Function

The spectral function is calculated from the imaginary part of the dressed propagator, Eq. (2.52), using the expression of Eq. (2.23).

$$S_\Lambda^p(\alpha;\omega) = \frac{1}{\pi}\frac{\mid \text{Im } \Sigma_\Lambda^{(s)}(\alpha;\omega) \mid}{[\omega - t_\Lambda(\alpha) - \text{Re } \Sigma_\Lambda^{(s)}(\alpha;\omega)]^2 - i[\text{Im } \Sigma_\Lambda^{(s)}(\alpha;\omega)]^2}. \tag{2.56}$$

The self-energy bears an 's' superscript to denote the fact that it is calculated using a self-consistent lambda spectrum. It should be emphasized that the spectral function of Eq. (2.56) is *not* truly self-consistent due to the simplifying approximation of Eq. (2.54).

A qp energy is defined as,

$$\varepsilon_\Lambda^{qp}(\alpha) = t_\Lambda(\alpha) + \text{Re } \Sigma_\Lambda^{(s)}(\alpha;\varepsilon_\Lambda^{qp}(\alpha)). \tag{2.57}$$

If the self-energy is only weakly energy dependent in the neighborhood of the qp energy, then it is evident from Eq. (2.56) that the spectral function will have a peak near $\omega = \varepsilon_\Lambda^{qp}(\alpha)$. Expanding the self-energy about $\varepsilon_\Lambda^{qp}(\alpha)$ as

$$\text{Re } \Sigma_\Lambda^{qp}(\alpha;\omega) \equiv \text{Re } \Sigma_\Lambda^{(s)}(\alpha;\varepsilon_\Lambda^{qp}(\alpha)) + \frac{\partial \text{Re } \Sigma_\Lambda^{(s)}(k;\varepsilon_\Lambda^{qp}(\alpha))}{\partial\omega}(\omega - \varepsilon_{qp}(k)), \tag{2.58}$$

$$\text{Im } \Sigma_\Lambda^{qp}(\alpha) \equiv \text{Im } \Sigma_\Lambda^{(s)}(\alpha;\varepsilon_\Lambda^{qp}(\alpha)), \tag{2.59}$$

yields the Quasi-Particle Approximation (QPA) to the spectral function. We define the following two functions

$$z(\alpha) \equiv 1 - [\frac{\partial \mathrm{Re}\ \Sigma_\Lambda^{(s)}(\alpha;\omega)}{\partial\omega}]^{-1}, \tag{2.60}$$

$$\gamma(\alpha) \equiv z(\alpha)\ |\ \mathrm{Im}\ \Sigma_\Lambda^{qp}(\alpha)\ |, \tag{2.61}$$

and make use of Eq. (2.57) to cast the QPA of the spectral function explicitly in the form of a lorentzian

$$S_\Lambda^p(\alpha;\omega) = \frac{1}{\pi}\frac{z(\alpha)\gamma(\alpha)}{[\omega - \varepsilon_\Lambda^{qp}(\alpha)]^2 + [\gamma(\alpha)]^2}. \tag{2.62}$$

Further details required to facilitate actual numerical work are included in Appendix A. Results for the Λ spectral function and qp-parameters are presented and discussed in the next chapter.

Chapter 3

Effects of Strong Correlations on Lambda Propagation in Nuclear Matter

In this chapter several aspects of the propagation of a Λ hyperon in nuclear matter are presented. In Section 3.1 the lambda spectral function is interpreted physically as a single-particle strength distribution in momentum and energy. Departure from the simple form expected for a free particle is discussed in terms of a strong coupling between 1p and 2p1h states through the self-energy. Details of how various populations of 2p1h states contribute to the imaginary part of the self-energy are examined by separating purely phase space factors from the G-matrix elements which effectively couple the states. These G-matrix elements are further dissected in an attempt to tease apart the strongly coupled channels which give rise to the complicated structure observed in the lambda self-energy.

In Section 3.2 quasi-particle parameters for the lambda are discussed and a simple model connecting them to the gross properties of the imaginary part of the self-energy is presented. Comments are made about the realm of accuracy for this approximation for the lambda. A comparison is made with similar quasi-particle results for the nucleon in nuclear matter as well as the saturation of spectral strength as a function of energy.

In Section 3.3 threshold effects associated with the ΣN channel are briefly discussed.

Finally, in Section 3.4 spectral strength at high energy is discussed.

3.1 Introduction: The Λ Spectral Function

From the definition of the spectral function in Eq. (2.16), the expression

$$a^{\dagger}_{\vec{k}}|\Psi(E_0)\rangle \tag{3.1}$$

has a physical interpretation as the state resulting from addition of a lambda with quantum numbers, $\vec{k}$, to the NM ground state. By definition, this represents a product state of a lambda sp state and the correlated NM ground state. This will not be an eigenstate as long as there are ΛN interactions present in the Hamiltonian. The actual energy eigenstates of the composite system of a lambda in NM are denoted by

$$|^{\Lambda}\Psi(E)\rangle. \tag{3.2}$$

The sp spectral function (Fig. 3.1) involves the overlap between the simple physical state of Eq. (3.1) and the complicated eigenstate of Eq. (3.2). The extent to which there is overlap illustrates how well the lambda sp state survives intact in the medium. For the case of no interactions between the lambda and the nucleons, the overlap is perfect, since the state of Eq. (3.1) is an eigenstate in this situation. This is evidenced by the delta-function spectral distribution appropriate for a free particle, as indicated by a dashed line at the kinetic energy in Fig. 3.1. Interactions between the lambda and nucleons are responsible for the transition from the simple delta-function structure to the more complex distribution of sp strength realized in NM. The mechanism behind the spreading of sp strength can be understood as the mixing of a 1p state at a given energy with 2p1h states which span a continuum of energies (Fig. 3.2). Although the sp state is no longer an eigenstate of the many-body Hamiltonian, its quantum numbers, such as total spin, isospin and momentum, are still conserved by the interaction. The total strength associated with the original sp state, though fragmented, is fixed. This is reflected in the sum rule of Eq. (2.20). Details of the strength distribution are determined by the density of 2p1h states (Fig. 3.2b) and the strength with which the interaction couples them to the unperturbed sp state (Fig. 3.2a). This information is summarized in the imaginary part of the self-energy, Fig. 3.3.

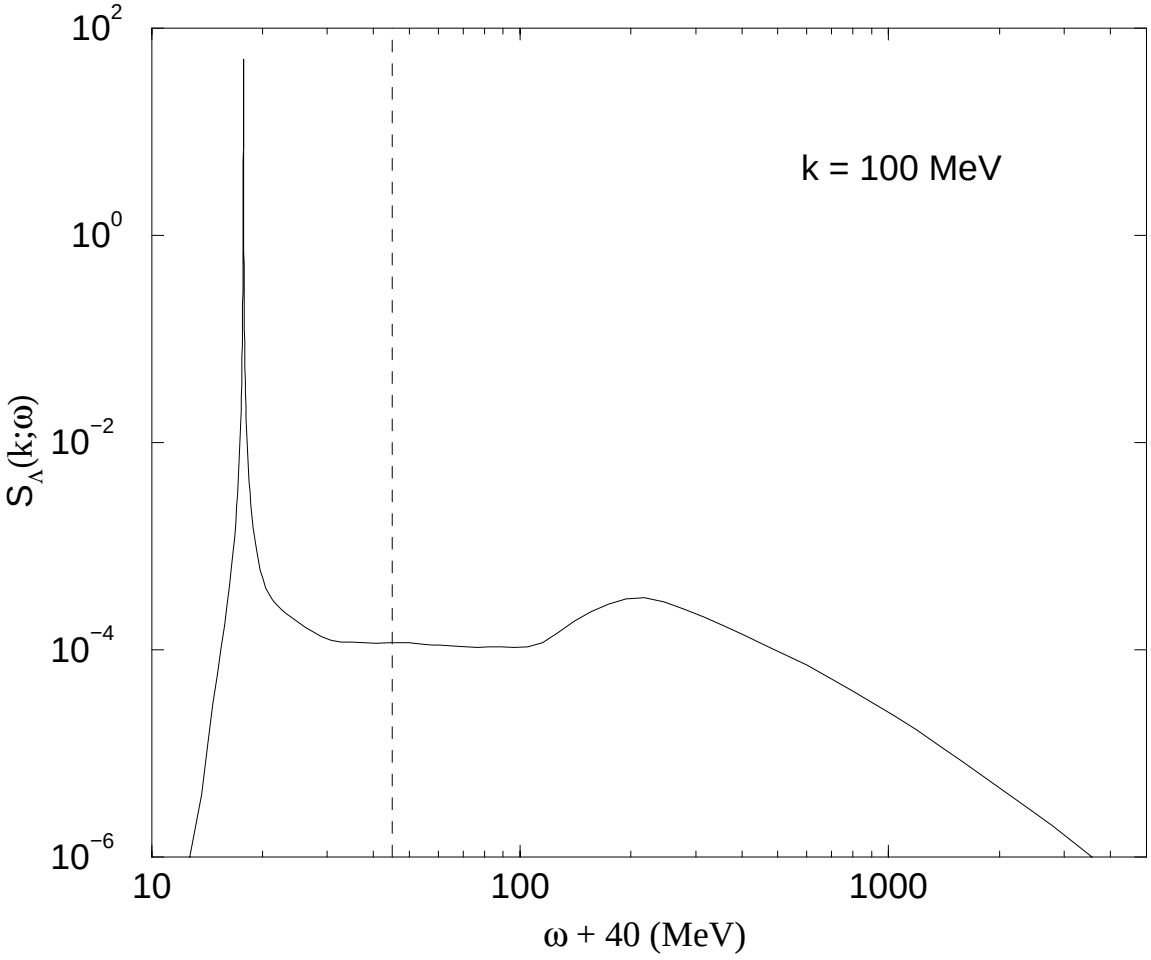

Figure 3.1: Spectral function for a lambda with $k = 100$ MeV/c. The vertical dashed line indicates the position of a delta-function spectral distribution for the limiting case of a free particle. Because of the 30 MeV binding for a lambda in nuclear matter, it is convenient to shift the horizontal axis by 40 MeV for plotting on a log scale.

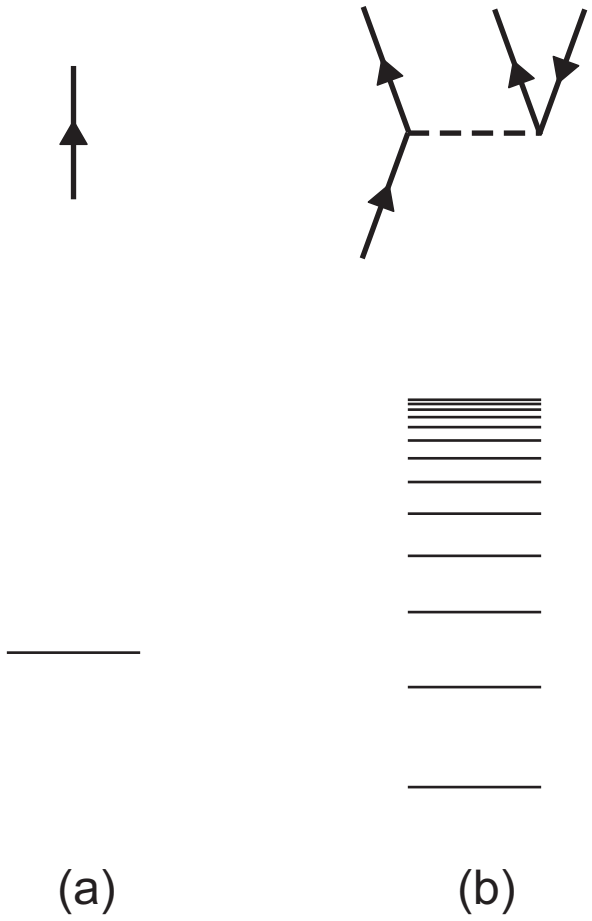

Figure 3.2: a. A free Λ occupies a sp state at a fixed energy. b. The ΛN interaction permits coupling to intermediate 2p1h states which span a range of energies, the density of states increasing with energy as schematically shown.

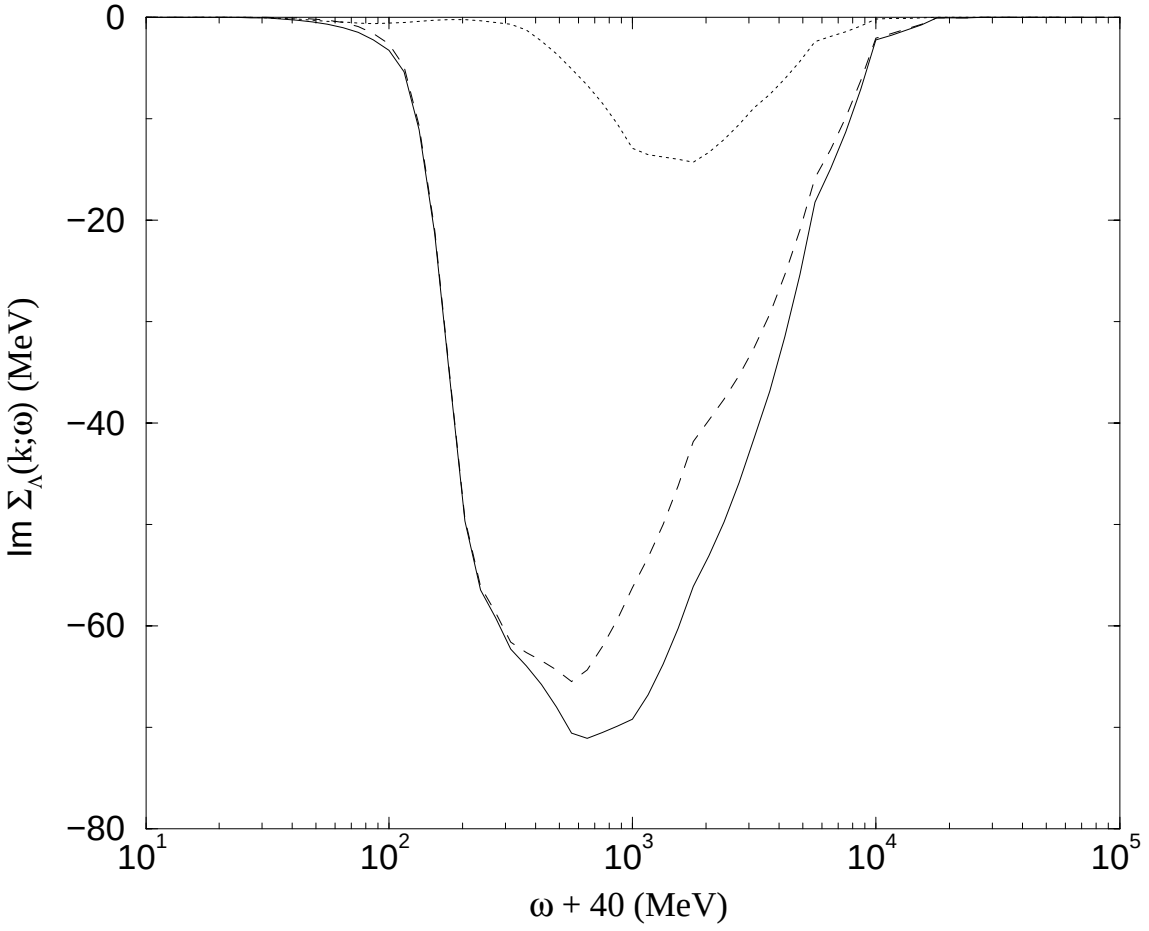

Figure 3.3: Imaginary part of lambda self-energy for $k = 100$ MeV/c. The broken curves represent contributions to the overall self-energy from the ${}^3S_1$ (dash) and ${}^1S_0$ (dot) partial wave channels.

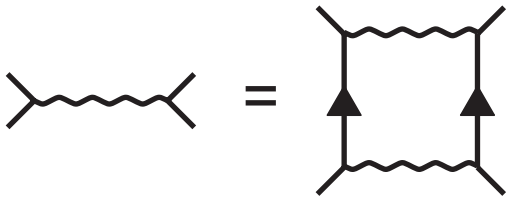

Figure 3.4: Diagrammatic representation of Eq. (3.4). Note that this equality only holds for the imaginary part of each side of the expression [24].

3.1.1 Relationship between Im Σ and density of 2p1h states

As shown in Eq. (2.47), the self-energy may be concisely expressed in terms of diagonal elements of the G-matrix,

$$\Sigma(\vec{k},\omega) \propto \int_0^{k_F^N} d^3q_N \langle \vec{k}\vec{q}_N | G(\omega + \varepsilon_N(\vec{q}_N)) | \vec{k}\vec{q}_N \rangle, \tag{3.3}$$

where an appropriate single-particle basis has been introduced explicitly (A.1). The imaginary part of these G-matrix elements may be expanded in terms of the uncorrelated two-particle propagator (Fig. 3.4),

$$\begin{aligned} \text{Im } \langle \vec{k}\vec{q}_N | G(\Omega) | \vec{k}\vec{q}_N \rangle \quad \propto \quad & \int_0^{\infty} d^3q_1 \int_{k_F^N}^{\infty} d^3q_2 |\langle \vec{k}\vec{q}_N | G(\Omega) | \vec{q}_1\vec{q}_2 \rangle|^2 \\ & \text{Im } g^{II}_{unc}(\vec{q}_1,\vec{q}_2;\Omega). \end{aligned} \tag{3.4}$$

This type of result may also be used in scattering theory to obtain the Optical Theorem [25]. In direct analogy to Eq. (2.14) for the sp propagator, the imaginary part of the uncorrelated two-particle propagator is just the two-particle spectral function,

$$\begin{aligned} \text{Im } g^{II}_{unc}(\vec{q}_1,\vec{q}_2;\Omega) \quad & \propto \quad \text{Im } \int d\Omega' \frac{S^{II}_{unc}(\vec{q}_1,\vec{q}_2;\Omega')}{\Omega - \Omega' + i\eta} \\ & \propto \quad S^{II}_{unc}(\vec{q}_1,\vec{q}_2;\Omega). \end{aligned} \tag{3.5}$$

If particles in the intermediate state are not dressed by interactions with the medium (as they would be in a fully self-consistent calculation), but rather are treated as free particles, then

$$S^{II}_{unc}(\vec{q}_1,\vec{q}_2;\Omega) \longrightarrow \delta(\Omega - \varepsilon_{2p}(\vec{q}_1,\vec{q}_2)) \tag{3.6}$$

and the two-particle spectral function reduces to a delta-function which picks out states with total energy, Ω. In this simplified case, Eq. (3.4) becomes

$$\begin{aligned} \text{Im } \Sigma(\vec{k},\omega) \quad \propto \quad & \int_0^{k_F^N} d^3q_N \int_0^{\infty} d^3q_1 \int_{k_F^N}^{\infty} d^3q_2 |\langle \vec{p}|G(\vec{Q},\Omega)|\vec{q}\rangle|^2 \delta(\omega - \varepsilon_{2p1h}) \\ & \delta(\vec{k} - [\vec{q}_1 + \vec{q}_2 - \vec{q}_N]), \end{aligned} \tag{3.7}$$

where

$$\varepsilon_{2p1h} \equiv \varepsilon_Y(\vec{q}_1) + \varepsilon_N(\vec{q}_2) - \varepsilon_N(\vec{q}_N). \tag{3.8}$$

In the above, momentum conservation has been used to write the matrix elements of the G-matrix as

$$\langle \vec{k}\vec{q}_N|G(\Omega)|\vec{q}_1\vec{q}_2\rangle = \delta([\vec{k} + \vec{q}_N] - [\vec{q}_1 + \vec{q}_2])\langle \vec{p}|G(\vec{Q},\Omega)|\vec{q}\rangle, \tag{3.9}$$

where $\vec{q}$ and $\vec{p}$ represent the relative momentum in the initial and final states respectively and $\vec{Q}$ is the conserved total momentum.

Eq. (3.7) reveals a direct connection between Im $\Sigma(\vec{k},\omega)$ and the phase-space for 2p1h states with momentum, $\vec{k}$, and energy, ω. Aside from a weighting supplied by matrix elements of the effective interaction, the imaginary part of the self-energy is directly proportional to the available 2p1h phase-space. For free, uncorrelated particles, this phase-space essentially contributes a $\sqrt{\omega}$ energy dependence to the imaginary part of the self-energy.

Interactions with particles in the medium serve to dress the intermediate particles and thereby void the assumptions leading to Eq. (3.6). They complicate the two-particle spectral function and typically lead to a diminished density of states at low energy [26]. However, this doesn't substantially alter the physical interpretation of Im Σ as expressed in Eq. (3.7). The imaginary part of the self-energy is still proportional to a weighted 2p1h phase-space, only now the intermediate particles are better thought of as quasi-particles.

For fixed parameters $\vec{k}$ and ω, the G-matrix element appearing in Eq. (3.3) varies slowly over the allowed range of $\vec{q_N}$. As a result, Eq. (3.3) may be well approximated by taking an average G-matrix element and integrating over the phase-space for nucleon holes,

$$\Sigma(k,\omega) \propto \langle k\bar{q}_N|G(\omega + \varepsilon_N(\bar{q}_N))|k\bar{q}_N\rangle \rho_N. \tag{3.10}$$

This indicates that the energy dependence of Σ is localized in a particular diagonal matrix element of G. The phase-space for nucleon holes merely contributes an overall energy-independent factor which is proportional to the nuclear density. A comparison of the imaginary part of the self-energy in Fig. 3.3 to the imaginary part of the G-matrix in Fig. 3.5 shows the close relationship of their energy dependence. In the following section, although the discussion is presented in terms of the imaginary part of the diagonal G-matrix elements for exactness, it applies well to the self-energy, if only approximately. In the end, it is the self-energy which directly determines the energy dependence of the spectral function.

3.1.2 Coupling 1p to 2p1h states

The δ-functions in Eq. (3.7) permit the integrals over intermediate state variables to be performed explicitly. Taken together with Eq. (3.3), an expression is readily derived for Im G where phase-space factors are conveniently decoupled from the weighting matrix elements,

$$\text{Im } \langle p|G(Q,\Omega)|p\rangle = -\pi \sum_{YL} |\langle p|G(Q,\Omega)|q_0\rangle|^2 \underbrace{Q_{YN}(Q,q_0) q_0^2 \left|\frac{\partial \varepsilon_{YN}}{\partial q}\right|^{-1}_{q=q_0}}_{\simeq\sqrt{\Omega}\simeq q_0}. \qquad (3.11)$$

Here p, Q and Ω are the relative momentum, total momentum and total energy for the ΛN state obtained by averaging over the nucleon hole momentum. The on-shell relative momentum, q_0, is defined by the two-particle energy through,

$$\Omega \equiv \varepsilon_{YN}(Q,q_0), \qquad (3.12)$$

and varies depending on which hyperon (Λ or Σ) is present in the intermediate state.

As indicated in Eq. (3.11), there are two sources of energy dependence for diagonal matrix-elements of Im G. There is a phase-space factor which, aside from Pauli effects and deviations from free spectra for the intermediate particles, contributes a simple, structureless energy dependence for each YN channel. The two YN channels do possess different energy thresholds and this does lead to an expectation of structure at the ΣN threshold (region near 70 MeV in Fig. 3.5) purely on the basis of phase-space considerations. However, most structure found in the energy dependence

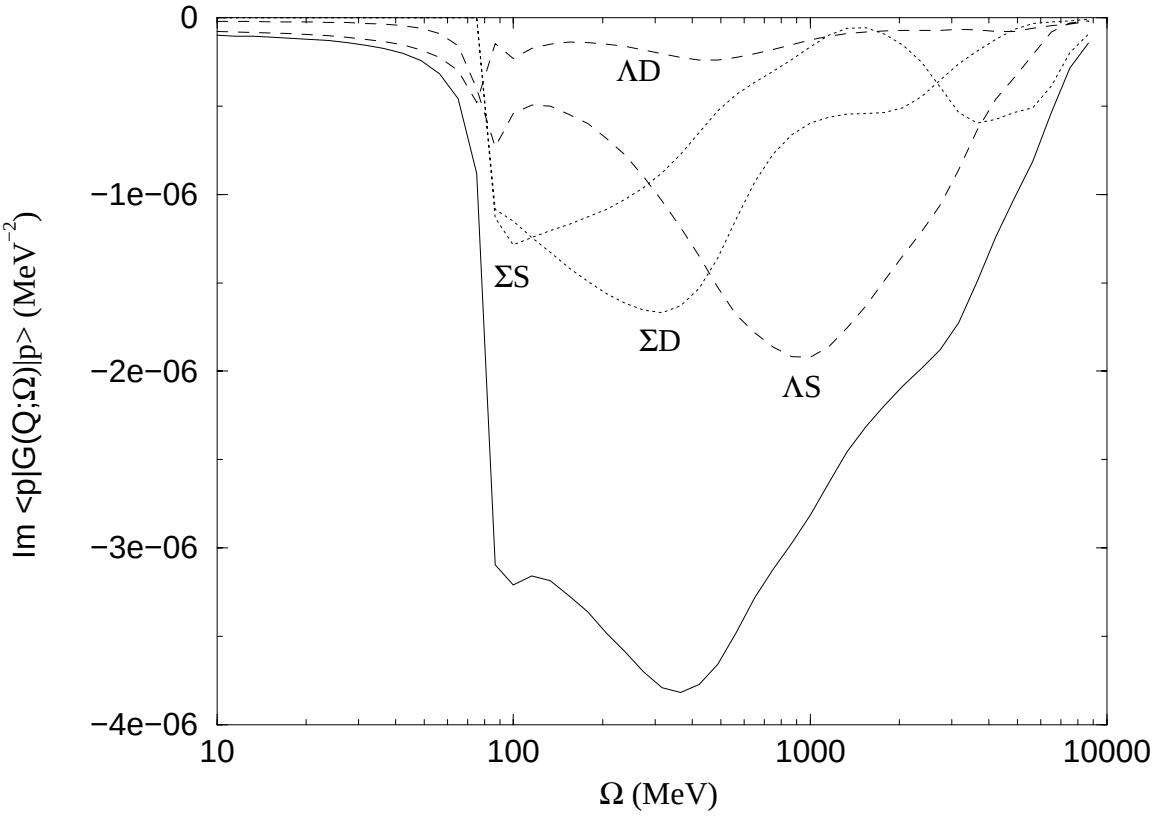

Figure 3.5: The components of Im G as defined by Eq. (3.11). One curve is associated with each YN intermediate state accessible from the initial $\Lambda N\,{}^3S_1$ state. The full curve is the sum of the four components.

of Im G can be attributed to the half-on-shell matrix elements of G which effectively couple the 1p and 2p1h states.

Taking the example of an initial $\Lambda N\,{}^3S_1$ state, Eq. (3.11) is plotted in Fig. 3.5. Contributions from each of four possible intermediate states, characterized by different YL combinations, are plotted together with their sum. All terms contribute significantly except for the $\Lambda N\,{}^3D_1$ intermediate state which couples relatively weakly to the initial state.

Though the form of Eq. (3.11) is useful for isolating purely phase-space influences on the energy dependence of Im G, a complex, non-linear tangling of states remains concealed within the half-on-shell G-matrix elements. These tangled intermediate states can be further unscrambled by considering a dissection of the pertinent G-matrix elements into a pair of complementary approximations. One may define a

"direct" approximation to a particular matrix element, $\langle\alpha|G|\beta\rangle$, by eliminating all matrix elements $\langle\gamma|V|\delta\rangle$ from the definition of the G-matrix equation *except* those where $\alpha = \gamma$ and $\beta = \delta$. The complementary "indirect" approximation to G is defined by eliminating *only* those matrix elements of V where $\alpha = \gamma$ and $\beta = \delta$. Note that complementary sets of approximate G-matrices are defined for each choice of initial and intermediate state.

As an example, consider the situation where only transitions to an intermediate $\Lambda N\,^3S_1$ state are allowed. This can be accomplished by generating a new G-matrix where all matrix elements of V are set to zero, except those which connect the initial state to the $\Lambda N\,^3S_1$ intermediate state. In this case there is only a single term in the sum of Eq.(3.11), corresponding to the lone available intermediate state. This version of Im G, where only the direct route to the $\Lambda N\,^3S_1$ intermediate state is available, is compared with the corresponding $\Lambda N\,^3S_1$ term from the result for the fully correlated G-matrix in Fig. 3.6. The shapes are very similar except in the energy range near the ΣN threshold and below. This similarity indicates that the effective couplings to the $\Lambda N\,^3S_1$ intermediate state are only modestly influenced by the presence of the other intermediates, except in the vicinity of the ΣN threshold.

The $\Lambda N\,^3S_1$-$\Sigma N\,^3D_1$ effective interaction is likewise dominated by direct coupling as shown in Fig. 3.7. This clearly shows that an energy region can be identified with states that are reached primarily via a tensor interaction (the few hundred MeV range). Contrast this with Fig. 3.6 where the $\Lambda N\,^3S_1$-$\Lambda N\,^3S_1$ term has no tensor interaction and peaks above 1 GeV. Indirect contributions factor in only marginally.

For some channels, a direct approximation is not feasible. In these cases, turning off the direct $\Lambda N\,^3S_1$-$\Lambda N\,^3S_1$ transition causes the numerical determination of the coupled channel G-matrix to become unstable. It still turns out to be useful to define and utilize a semi-direct approximation in these cases. In this approximation, the $\Lambda N\,^3S_1$-$\Lambda N\,^3S_1$ potential is retained, along with the matrix elements for the direct transition. Inclusion of these matrix elements serves to stablize the numerics while only interfering minimally (at higher order). A semi-direct approximation to $\Lambda N\,^3S_1$-$\Sigma N\,^3S_1$ channel involves turning off all tensor interactions and leaving only the two central transitions. Fig. 3.8 confirms that this approximation primarily cuts in the "tensor" region identified from Fig. 3.7 and this is where the indirect approximation gives its largest contribution.

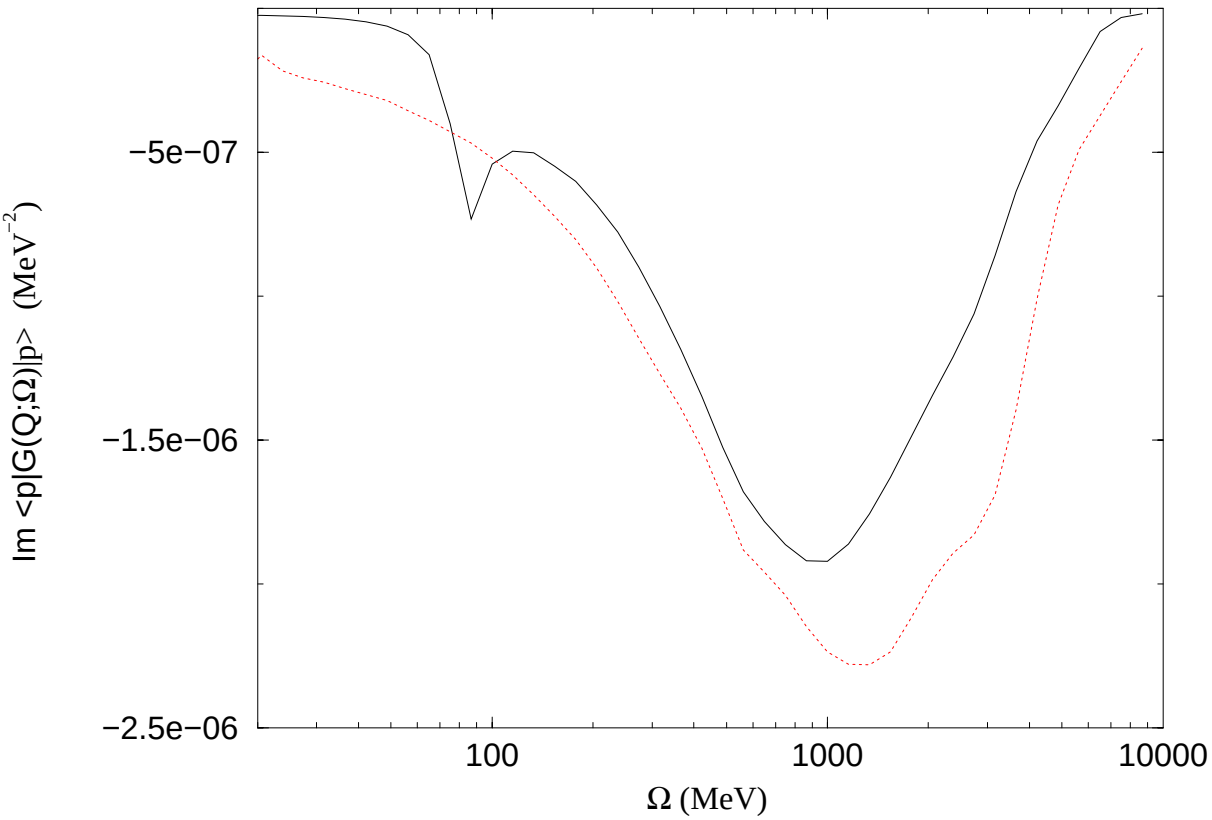

Figure 3.6: Dashed curve is the direct approximation to Im G for the $\Lambda N\,{}^3S_1$ intermediate state. The full curve is the Im G component attributed to this same intermediate state when all couplings are intact. Note that there is no indirect contribution for this channel because the direct $\Lambda N\,{}^3S_1 \to \Lambda N\,{}^3S_1$ transition turns out to be crucial for the numerical determination of the G-matrix.

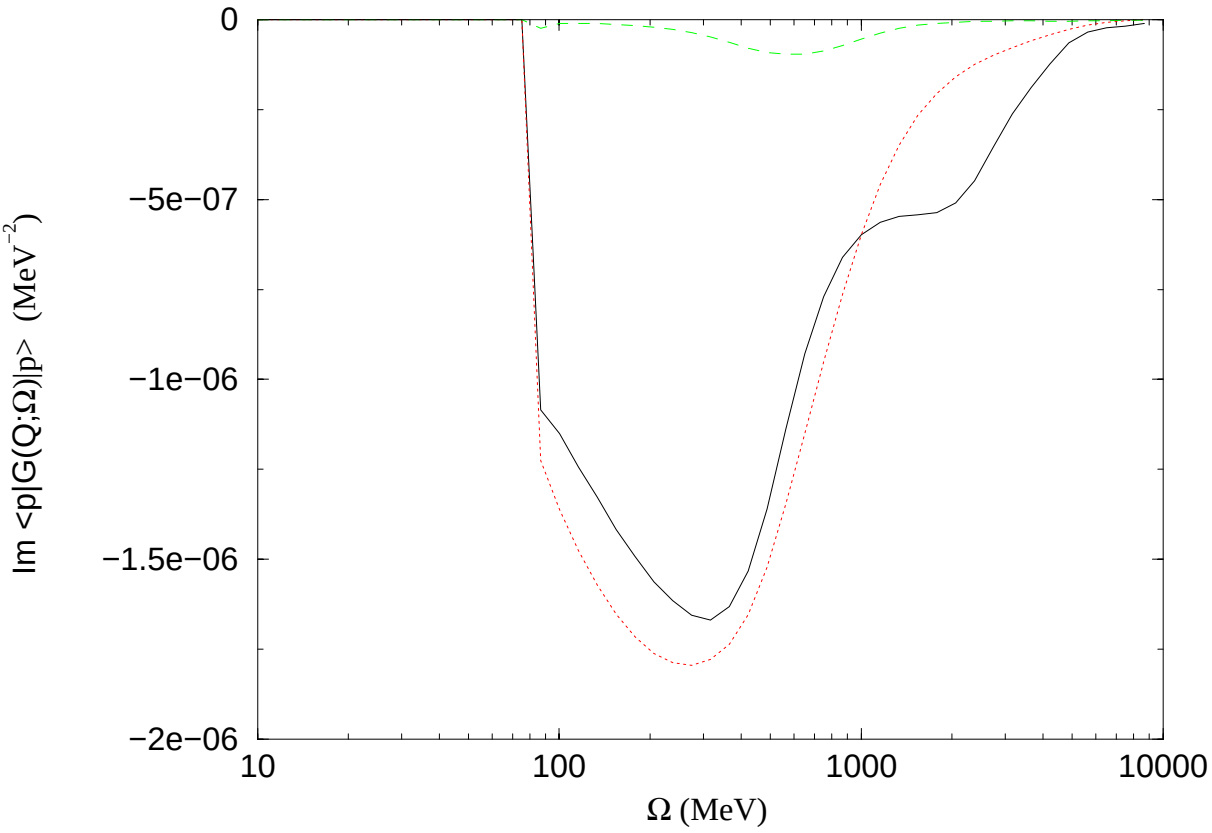

Figure 3.7: Direct (dotted) and indirect (dashed) approximations to Im G for the $\Sigma N\,{}^3D_1$ intermediate state.

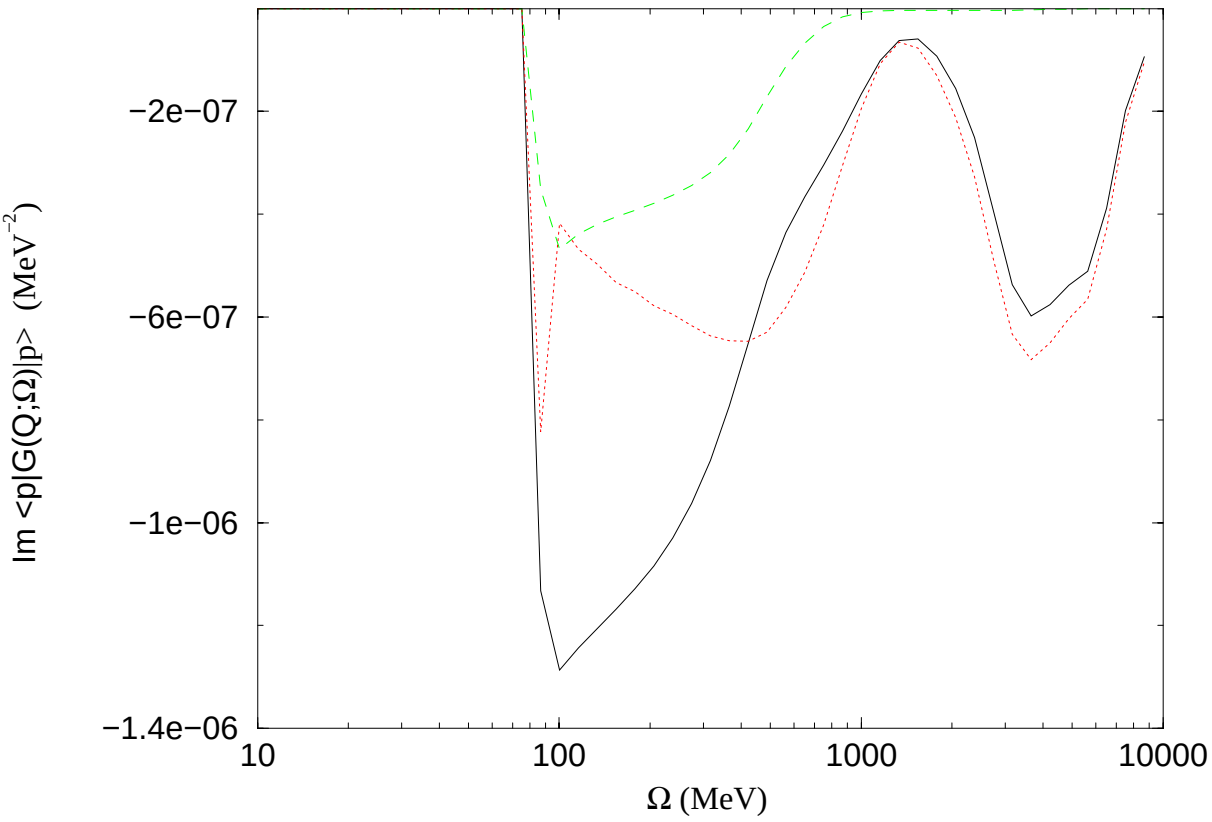

Figure 3.8: Semi-direct (dotted) and indirect (dashed) approximations to Im G for the $\Sigma N\,{}^3S_1$ intermediate state. Semi-direct because the $\Lambda N\,{}^3S_1$-$\Lambda N\,{}^3S_1$ couplings must still be included in order to obtain reasonable results.

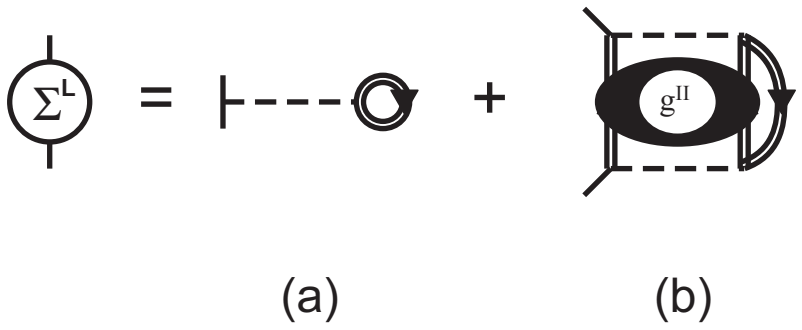

Figure 3.9: a. The HF part of the self-energy. b. Second order self-energy diagram; allows coupling to intermediate 2p1h states.

3.2 The Quasi-Particle Peak

As indicated by the spectral function peak in Fig. 3.1, an energy region with a substantial amount of sp strength survives the mixing with higher-lying 2p1h states. [1] However, this qp peak is shifted in energy, broadened and has lost some fraction of strength compared to the delta-function distribution appropriate for a non-interacting particle.

3.2.1 Location

The location of the peak is given by the qp energy as defined in Eq. (2.57). The real part of the self-energy, playing the role of a sp potential, shifts the peak from its unperturbed location at the kinetic energy. The self-energy can be split into two pieces,

$$\Sigma(k;\omega) = \Sigma_V(k) + \Sigma_\Delta(k;\omega), \tag{3.13}$$

each corresponding to a different type of physical process (Fig. 3.9).

Treating the self-energy at lowest order in the ΛN interaction (the HF approximation) only elastic scattering between the lambda and nucleons below the fermi energy is considered, Fig. 3.9a. This leads to a real, energy-independent contribution to the self-energy, $\Sigma_V(k)$. This term is relatively large and positive, on the order of 50 MeV, reflecting the repulsive character of the bare interaction.

[1] True to a lesser extent for systems at higher density or subject to stronger interactions, such as liquid helium [27].

The coupling to 2p1h intermediate states is represented by the diagram of Fig. 3.9b. Such processes induce a complex, energy-dependent component to the self-energy, $\Sigma_\Delta(k;\omega)$. This self-energy piece obeys a dispersion relation (Eq.2.49),

$$\text{Re } \Sigma_\Delta(k;\omega) = \frac{-P}{\pi}\int_{\varepsilon_F^\Lambda}^{\infty} d\omega' \frac{\text{Im } \Sigma(k;\omega')}{\omega - \omega'}. \tag{3.14}$$

This means that the real part of the self-energy in the neighborhood of some particular energy, such as ε_{qp}, requires knowledge of Im $\Sigma(k;\omega)$ at all energies. The imaginary part of the self-energy is dominated by a broad, smooth peak at high-energy, as seen in Fig. 3.3. In contrast, the qp peak resides at a much lower energy, $\varepsilon_{qp}(k)$; far removed from the bulk of the strength in Im $\Sigma(k;\omega)$, which is centered at some energy, ω_0, in the GeV range. If the only appreciable contribution to Eq. (3.14) evaluated at $\omega = \varepsilon_{qp}(k)$ comes from ω' near ω_0, then the denominator in the integrand may be approximated as a constant: $\varepsilon_{qp}(k) - \omega_0$. This leaves

$$\begin{aligned} \text{Re } \Sigma_\Delta(k;\varepsilon_{qp}(k)) &\simeq \frac{-1}{\pi}\frac{1}{\varepsilon_{qp}(k)-\omega_0}\int_{\varepsilon_F^\Lambda}^{\infty} d\omega' \text{Im } \Sigma(k;\omega') &(3.15)\\ &= \frac{-1}{\pi}\frac{I_0}{\varepsilon_{qp}(k)-\omega_0}, &(3.16)\end{aligned}$$

where I_0 is just the integrated strength in Im $\Sigma(k;\omega)$. In this approximation Re $\Sigma_\Delta(k;\varepsilon_{qp}(k))$ depends on only two parameters which together characterize the gross properties of Im $\Sigma(k;\omega)$; the integrated strength, I_0, and the centroid of the high energy peak, ω_0. [2] These two parameters define a model for a simple low-energy approximation to Re Σ_Δ,

$$\text{Re } \Sigma_\Delta^{\text{model}}(k;\varepsilon_{qp}(k)) \equiv \frac{-1}{\pi}\frac{I_0}{\varepsilon_{qp}(k)-\omega_0}. \tag{3.17}$$

The full structure of the self-energy is shown in Fig. 3.10 with the two-parameter model for comparison.

Decreasing the density of 2p1h states and/or the strength of coupling to these states is analogous to a decrease in the parameter I_0. This simply scales down the real part of the self-energy for all energies, thereby reducing the binding contribution to ε_{qp}. Alternatively, moving the 2p1h states to higher energy can be mimicked by

[2] Though nominally k dependent, the parameters I_0 and ω_0 should vary only slowly with k since they characterize the gross structure of Im $\Sigma(k;\omega)$ at high energy; structure which is far removed from the low energy realm of the qp peak.

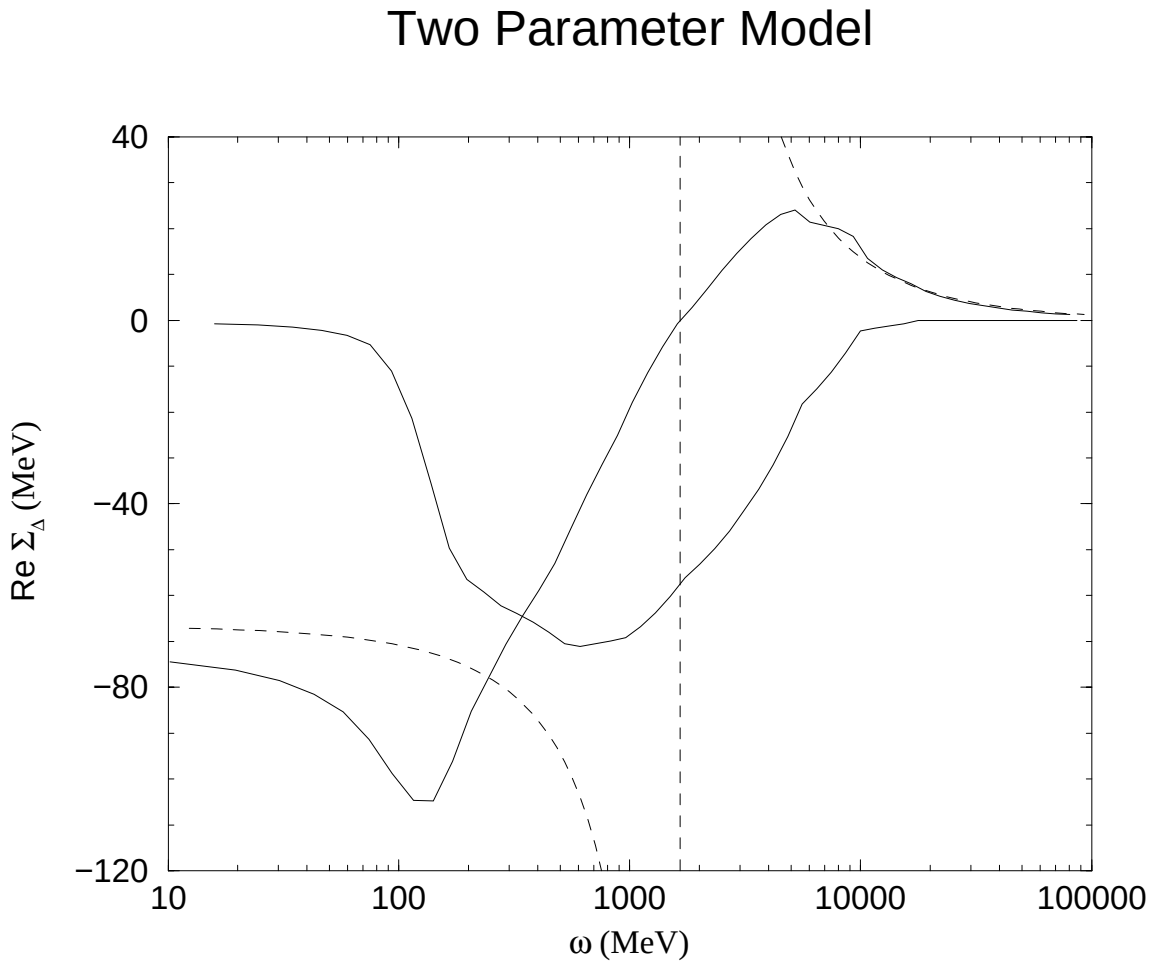

Figure 3.10: Real and imaginary parts of the exact self-energy are plotted with the solid lines and the real part from the model is plotted as a dashed curve for comparison.

an increase in the parameter ω_0, which likewise results in a reduction in the real part of the self-energy at ε_{qp} and a consequent decrease in qp binding. [3]

The success of this simple model, limited as it is, indicates that ε_{qp} is dominantly determined by high-energy 2p1h states, but at the same time is relatively insensitive to details of the coupling to these states. To quantify the insensitivity of ε_{qp} to low-lying excited states, one can isolate the low-energy tail of Im $\Sigma(k;\omega)$ in Eq. (3.14), and examine its effect on ε_{qp}. The first 100 MeV of Im $\Sigma(k;\omega)$ above the lambda threshold only contributes to ε_{qp} at the level of a few percent. The disparity of about 10 MeV between the model and the full result can be attributed to the finite width of the peak, and especially the low-energy shoulder in the range of a few 100 MeV where coupling to the ΣN channel is most important. It should be noted that these results are contingent on Im $\Sigma(k;\omega)$ being of a form similar to that depicted in Fig. 3.3. The imaginary part of the self-energy is dominated by its structure at high energy precisely when SRC dominate the ΛN effective interaction from which it is derived. This depends in part on the short-range behavior of the bare interaction, but also on the approximation method selected when defining the effective interaction. The ladder approximation adopted in this work is specifically chosen because it incorporates the essential features of SRC while de-emphasizing LR behavior and more collective states which naturally occur at low excitation energy. A realistic calculation for a finite hypernucleus, utilizing the same bare interaction, but going beyond the ladder approximation might well show greater sensitivity to low-lying states [28].

Since $I_0 < 0$, the real part of the self-energy will be negative for any energy below ω_0, including the "on-shell" region near the qp peak. This means that the self-energy term which represents the coupling to high-energy 2p1h states (Fig. 3.9b) will always *lower* the energy of the qp state. This result is familiar from perturbation theory, where a second-order correction to the energy always serves to lower the energy of the ground state. This binding more than offsets the HF contribution to ε_{qp} and leads to a monotonically increasing qp spectrum. A sp potential, $U(k)$, defined by

$$\varepsilon_{qp}(k) \equiv t(k) + U(k), \tag{3.18}$$

is plotted in Fig. 3.11 together with the sp potential employed for the nucleons.

[3] Though ε_{qp} will be shifted as well, this change is insignificant compared to a change on the energy scale of ω_0.

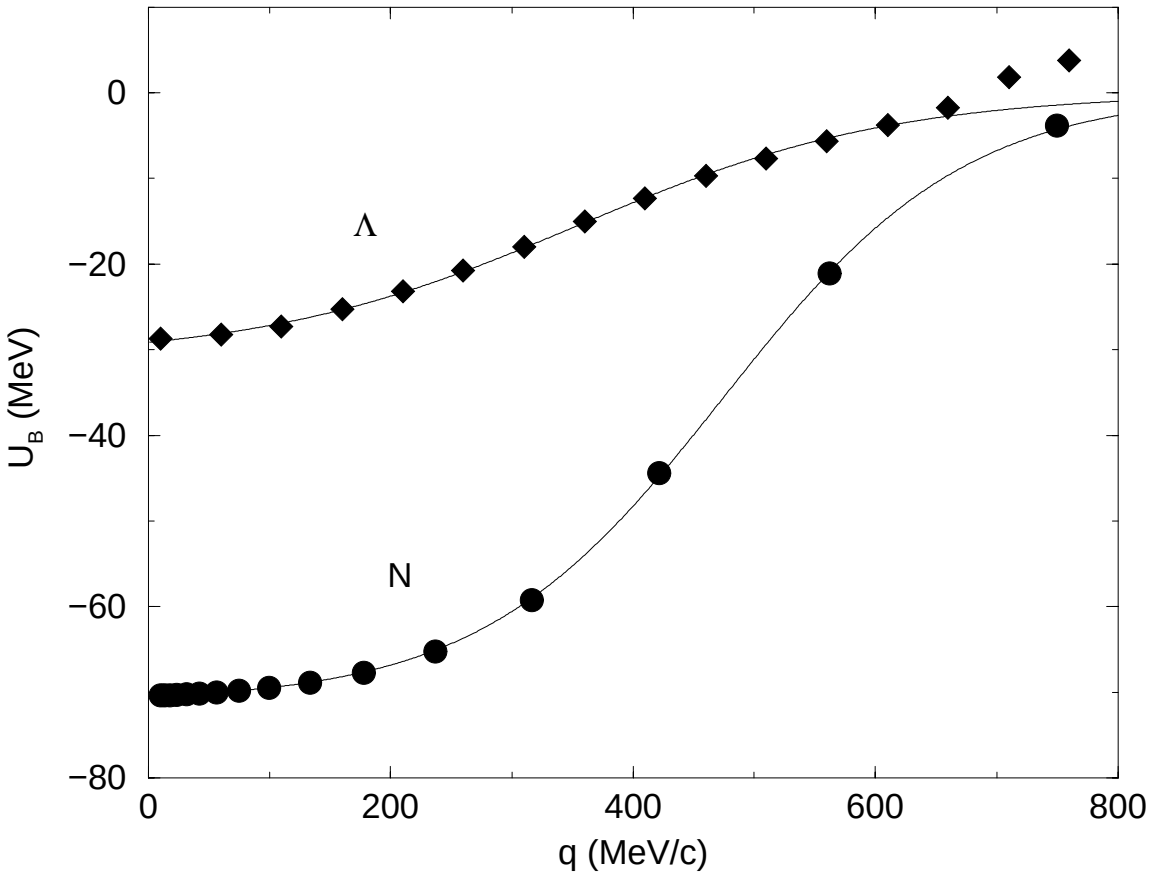

Figure 3.11: Potentials of Wood-Saxon form are fitted to calculated data for the Λ and the nucleon. The analytic approximation is useful when the derivative of a particle spectrum is required.

The net binding of 30 MeV for a lambda at rest in NM is consistent with other calculations [13] as well as an extrapolation from experimentally measured s-shell binding energies for hypernuclei [29]. Only the S-waves are included in this work. Higher partial waves yield corrections to ε_{qp} on the order of no more than 10% and even at this level tend to cancel each other out [30].

3.2.2 Width

In contrast to the position of the qp peak, which is essentially determined by the structure of the imaginary part of the self-energy at very high energies, the width of the peak is directly proportional to the local value of Im Σ at the qp energy (Eq. 2.61). To the extent that coupling to these low-lying 2p1h states is only weakly momentum dependent (for low values of k), the width is directly proportional to the local density of 2p1h states. Phase space restrictions near the 2p1h threshold determine the low-energy structure of the imaginary part of the self-energy [31].

$$\text{Im } \Sigma(k;\omega) \simeq c(k)[\omega - \varepsilon_F]^2 \quad \omega \to \varepsilon_F^+. \tag{3.19}$$

For values of k such that $\varepsilon_{qp}(k)$ is low enough to fall in the energy range where Eq. (3.19) is valid, the qp width can be simply expressed as a function of the peak position,

$$\gamma(k) \simeq c'(k)[\varepsilon_{qp}(k) - \varepsilon_F]^2. \tag{3.20}$$

This approximation is shown together with the calculated width as a function of momentum in Fig. 3.12, where the factor $c'(k)$ has been approximated as a constant, independent of k. Although this model for the qp width is not precisely accurate except very near $k = 0$, it does suggest the origin of the growth of $\gamma(k)$ with increasing k.

If the qp part of the spectral function is interpreted as a distinct sp-like state, then $\gamma_{qp}(k)$ is the width induced by coupling to a population of nearby states.

Overlaying the QPA to the spectral function on top of the full spectral function, Fig. 3.13, demonstrates the utility of the QPA for low k. A quantitative discussion of the QPA range of validity is provided in Appendix B. A sharp rise in Im $\Sigma(k;\omega)$ occurs in the vicinity of $\omega \simeq 200$ MeV as can be seen in Fig 3.3. When $\varepsilon_{qp}(k)$ reaches this energy range, the QPA is no longer a reasonable approximation. This occurs for

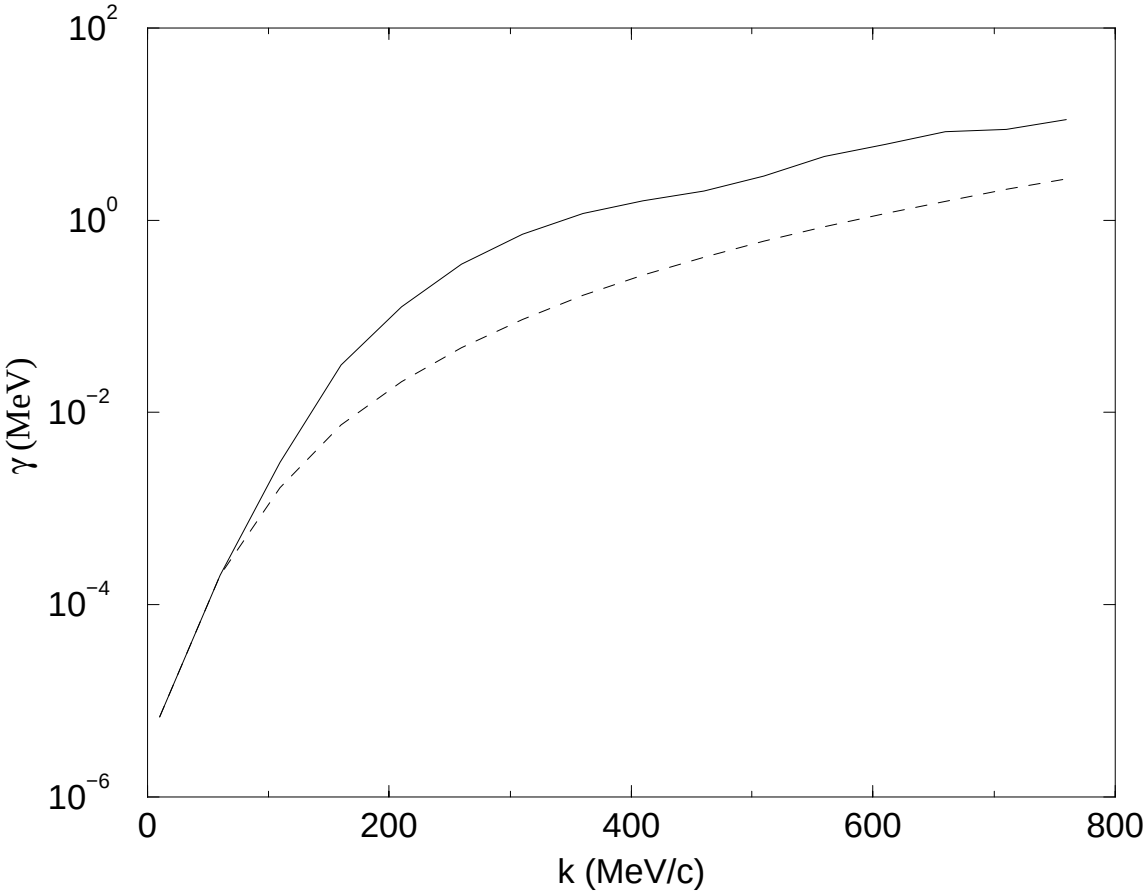

Figure 3.12: The solid curve represents the qp width as a function of k. The dashed curve represents an approximation to the width based on the local density of 2p1h states.

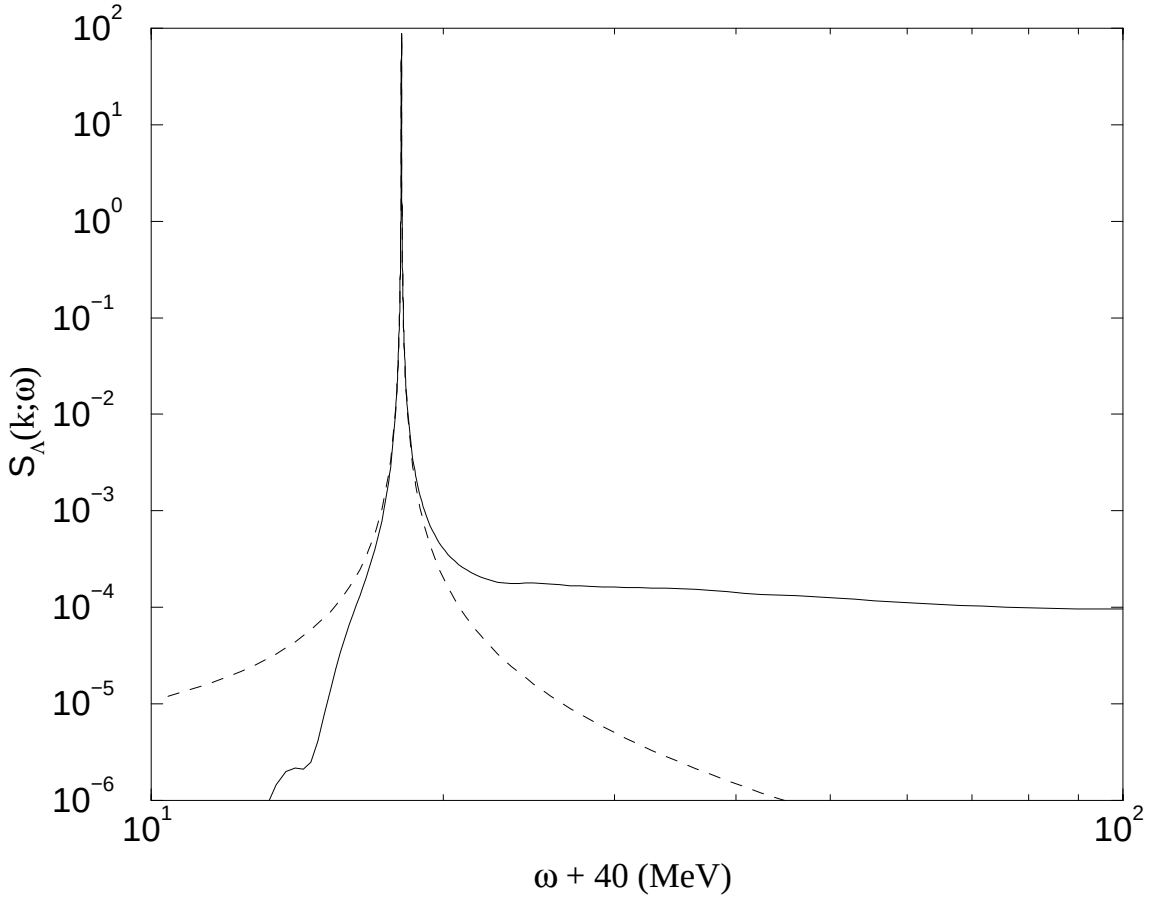

Figure 3.13: Solid curve is the full spectral function for $k = 110$ MeV/c. The dashed curve is the QPA.

a lambda with momentum in the neighborhood of $k \simeq 600$ MeV/c and is a sign that another energy threshold has been crossed. This threshold is discussed in Section 3.3.

3.2.3 Strength

According to Eq. (2.60), the amount of spectral strength concentrated in the qp peak is given by the derivative of Re $\Sigma_\Delta(k;\omega)$ with respect to ω locally at ε_{qp}. In terms of the dispersion relation for Re $\Sigma_\Delta(k;\omega)$, Eq. (2.60) becomes

$$z(k) = \left[1 - \frac{P}{\pi}\int_{\varepsilon_F}^{\infty} d\omega' \frac{\text{Im } \Sigma(k;\omega')}{(\varepsilon_{qp}(k) - \omega')^2}\right]^{-1}. \tag{3.21}$$

Comparing to Eq. (2.49), the strength in the qp peak, $z(k)$, is seen to exhibit a greater sensitivity to the structure of Im $\Sigma(k;\omega)$ than does the peak position, ε_{qp}. The z-factor (Fig. 3.14) is most accurate as a measure of strength in the peak of the spectral function for low values of k, as discussed in Appendix B.

A nuclear matter calculation for nucleons similar to this one [32] yields a particle spectral function like Fig. 3.15, for a momentum just above k_F^N. The z-factor obtained from this calculation is $z_N(k_F^N) = 0.72$, which is substantially reduced compared to $z_\Lambda(k_F^\Lambda) = 0.87$ for a similar lambda qp state. These two momentum values are compared because each qp sits at the lowest possible excitation energy for a qp in the respective systems. In Ref. [32], the depletion of the qp strength is explained in terms of couplings to 2h1p states, which moves approximately 10% of the sp strength to energies below ε_F^N, and coupling to 2p1h states, which distributes another 18% to higher energies in the particle domain. The corresponding fraction of sp strength in the particle domain is 13% for the lambda, compared to 18% for nucleons. A more detailed look at the distribution of strength as a function of energy is given in Fig. 3.16.

The relative effects of tensor and short-range correlations can be untangled to some extent. Turning off the $^3S_1 - ^3D_1$ tensor coupling in the Reid potential for nucleons indicates that this interaction is responsible for depleting the qp strength by about 6.5%, almost all within 1000 MeV of ε_F^N. Similarly, turning off the ΛN-ΣN coupling in the NSC89 potential reveals that tensor effects are responsible for almost half of the reduction in the lambda qp strength. A value of $z_\Lambda(k_F^\Lambda) = 0.94$ is obtained when coupling to ΣN states is cut off.

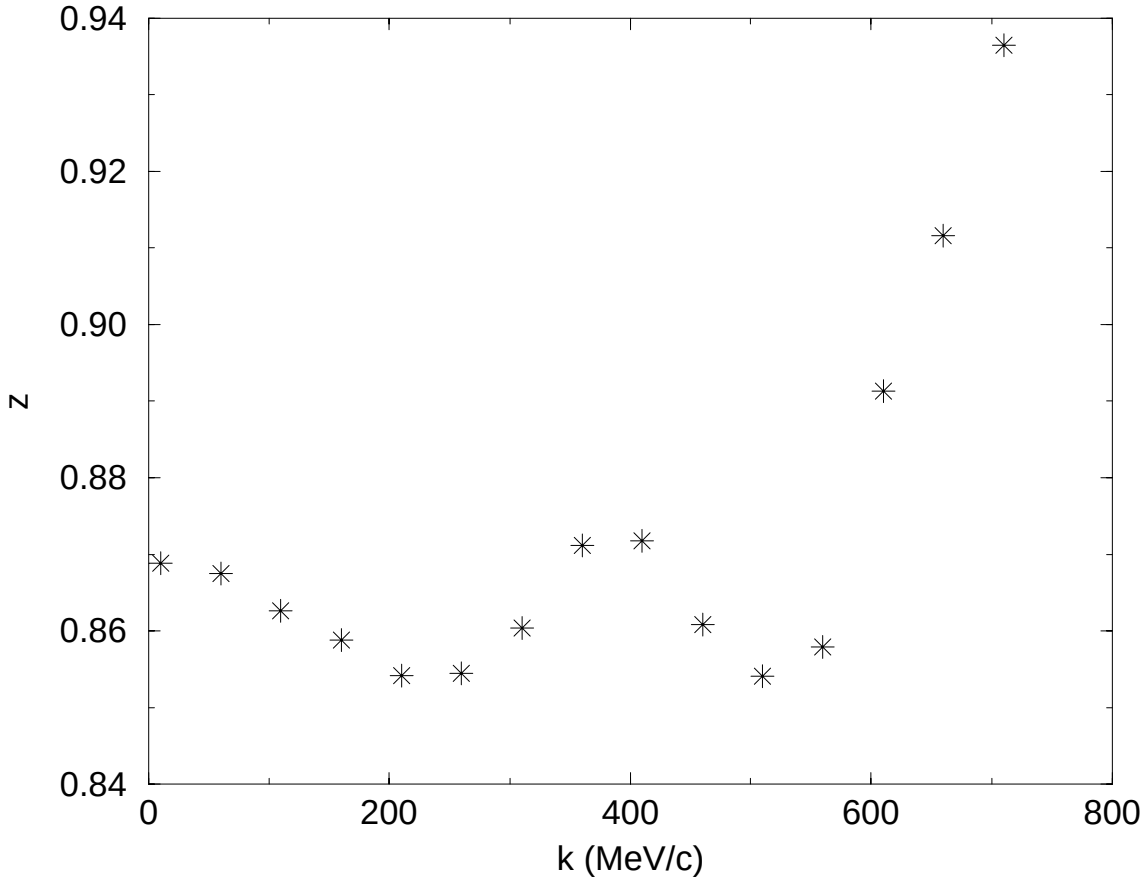

Figure 3.14: Quasi-particle strength as a function of k.

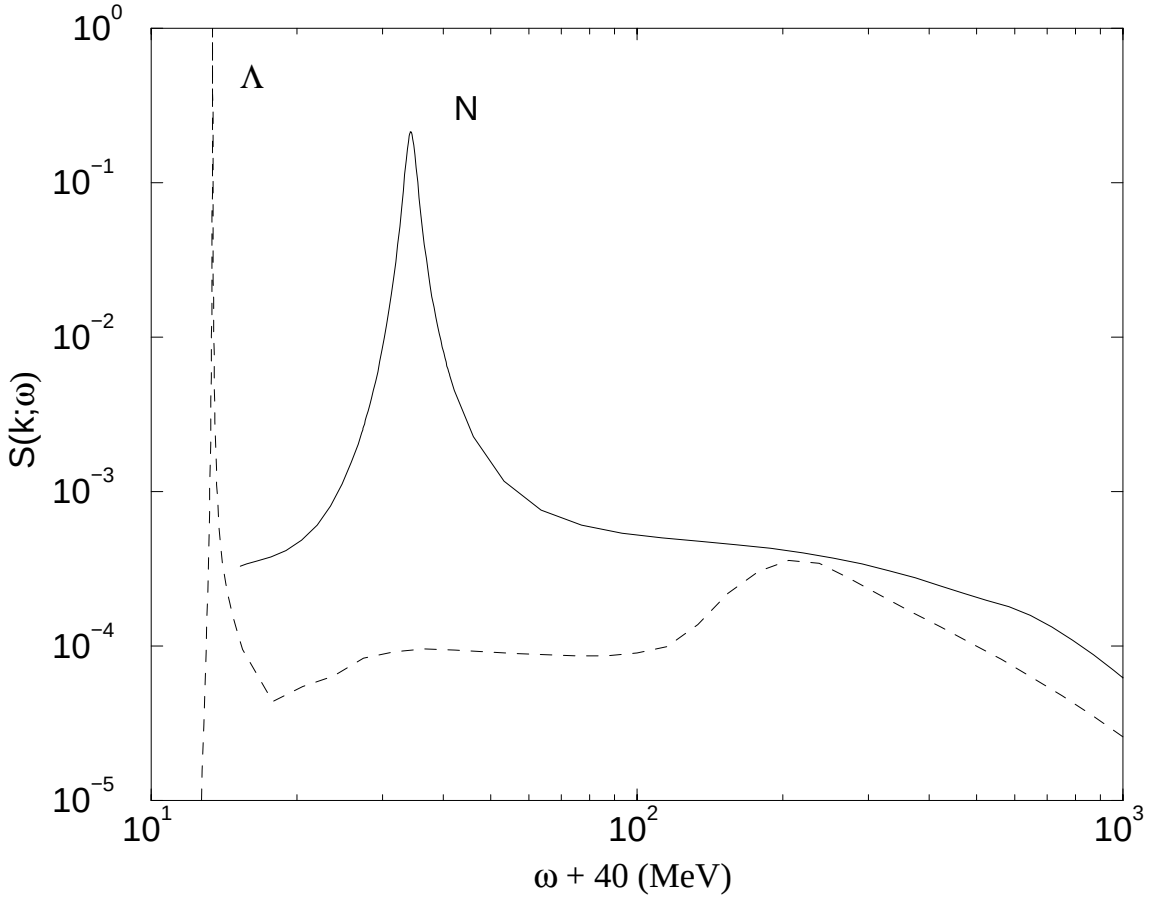

Figure 3.15: Nucleon particle spectral function (solid) for $k = 316$ MeV/c with lambda spectral function (dashed) at $k = 60$ MeV/c for comparison.

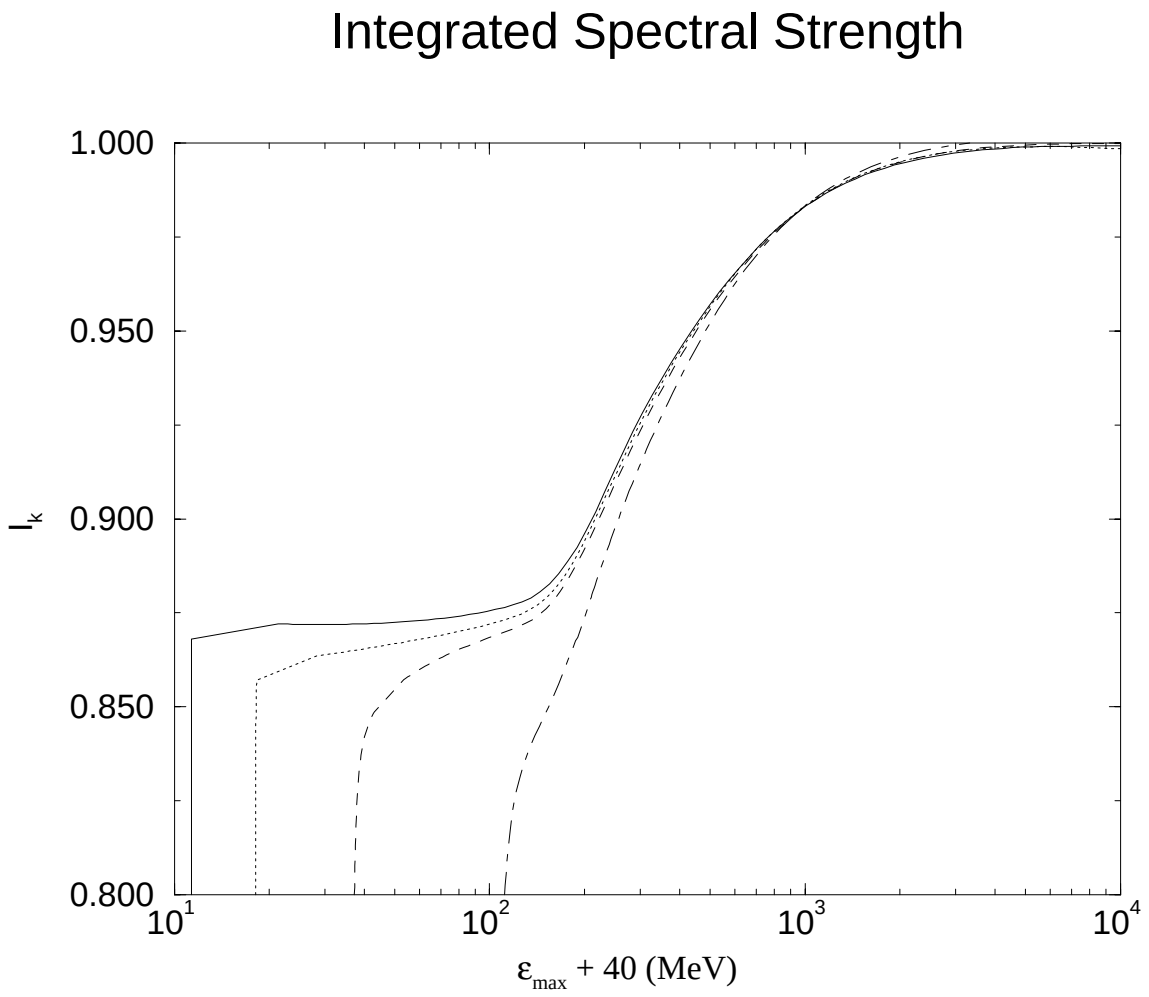

Figure 3.16: Single-particle strength integrated from ε_F^{Λ} to ε_{max} as a function of ε_{max} for different momenta. $k = 10$ MeV (solid), $k = 110$ MeV (dot), $k = 210$ MeV (dash), $k = 310$ MeV (dot-dash).

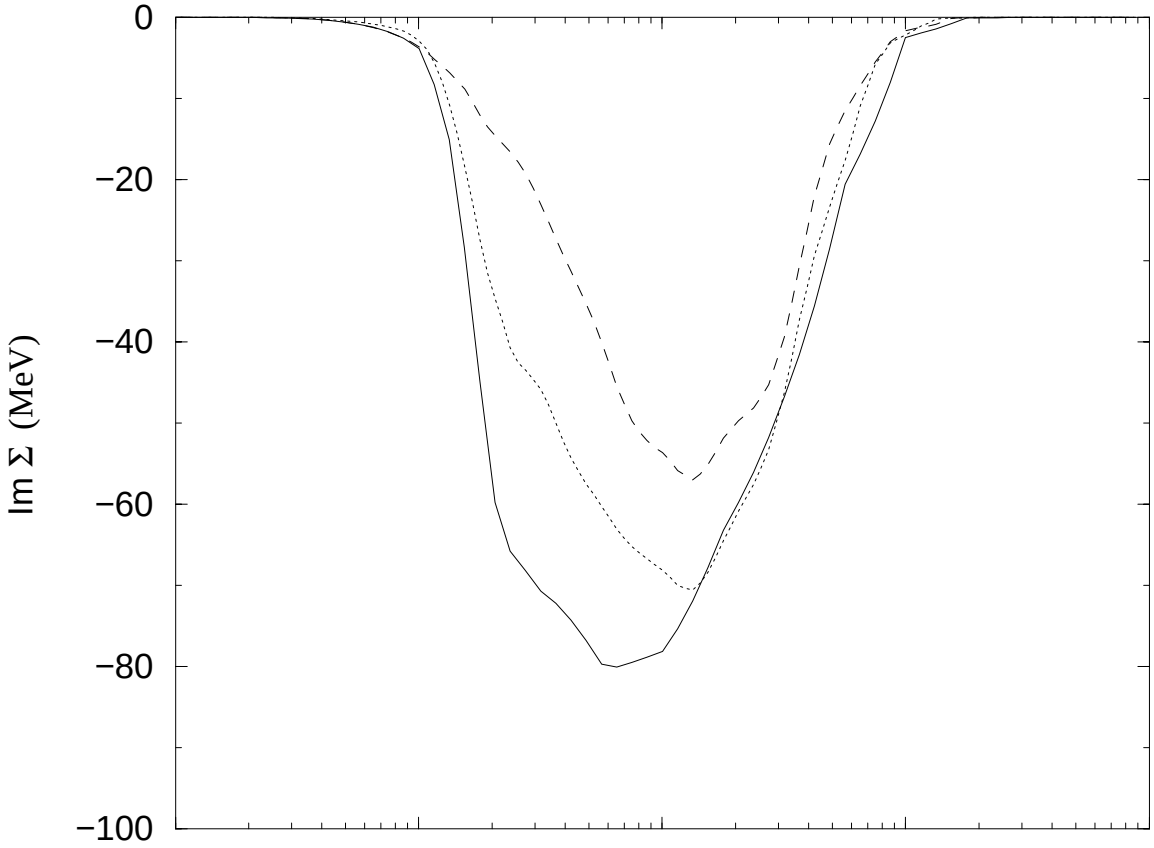

Figure 3.17: Im Σ for the case where ΛN - ΣN coupling is included (solid curve), without coupling (dashed) and when π-exchange is turned off in V (dotted). Plotting with respect to self-consistently determined Λ threshold energy ensures that the ΣN threshold is in the same location for each curve. $k = 10$ MeV/c.

3.3 The ΣN Threshold

In NM the ΣN threshold opens at an energy about 90 MeV above the self-consistently determined ΛN threshold. [4] Again, the imaginary part of the self-energy provides a picture of how the ΣNN^{-1} 2p1h states influence Λ sp properties. The imaginary part of the self-energy is plotted in Fig. 3.17 for the case where coupling to the ΣN states is turned off. Turning off the ΣN coupling leads to a recovery of 7% of the strength in the qp peak as the z-factor increases from 0.86 to 0.93. A reduction in spectral strength is observed at all energies, but is particularly apparent at, and just above, the ΣN threshold. There are two reasons ΣNN^{-1} 2p1h states are most influential in

[4] The mass difference is $m_\Sigma - m_\Lambda = 77$ MeV, but the Λ is bound in NM by about 30 MeV whereas the Σ binding is about half as much.

this energy region. First, a "threshold effect" is responsible for the sharp cusp in Im Σ near 100 MeV. This behavior may be understood physically in the same way as the cusp observed in the ΣN elastic scattering cross-section [33]. In scattering theory, the elastic cross-section may be calculated from the bare two-body interaction via the on-shell elements of the T-Matrix. In NM, an effective interaction, such as the G-Matrix is a generalization of the free-space T-Matrix. Structure arises in the ΛN G-matrix as a consequence of the strong coupling to the nearby ΣN channel [34]. From Eq. (2.47), the imaginary part of the self-energy shares the same structure as the imaginary part of the G-Matrix.

Secondly, isospin conservation in the strong ΛN interaction forbids excitation of nuclear ph states via π-exchange. However, this is a strongly allowed process for the ΣN interaction, preferentially exciting $\Sigma N N^{-1}$ 2p1h states in the energy range of a few hundred MeV. Turning off the π-exchange component of the bare interaction (Fig. 3.17) demonstrates that it is partly responsible for the ΣN channel's influence on the Λ, but apparently the non-tensor part of the ΛN-ΣN coupling plays just as significant a role, even in the "tensor" region. The nucleon spectral function manifests a similar feature of an energy range dominated by the tensor interaction [35].

The effect on the spectral function is to induce additional structure in the vicinity of the threshold energy (Fig. 3.18). The spectral signature of this new channel is a reduction of strength just below threshold followed by an enhancement immediately above threshold which slowly dies out at increasing energy. The location of the ΣN threshold is dependent on the total momentum of the ΛN pair. The self-energy involves an average over all values of Q that can be realized for a Λ with a given momentum, k, and a nucleon hole which can have a range of momentum according to the nuclear density. This averaging smears out the location of the "cusp" structure in the self-energy and in the spectral function.

3.4 The High Energy Region

Away from the qp peak, at high-energy, the size and structure of the spectral function is primarily determined by two factors. The density of 2p1h states increases like $\omega^{1/2}$ at high energy. This growth in spectral strength with energy is moderated by the strength of the coupling to these high energy states. A lambda with a reasonably low momentum couples to a nucleon hole state only with a low relative momentum. The

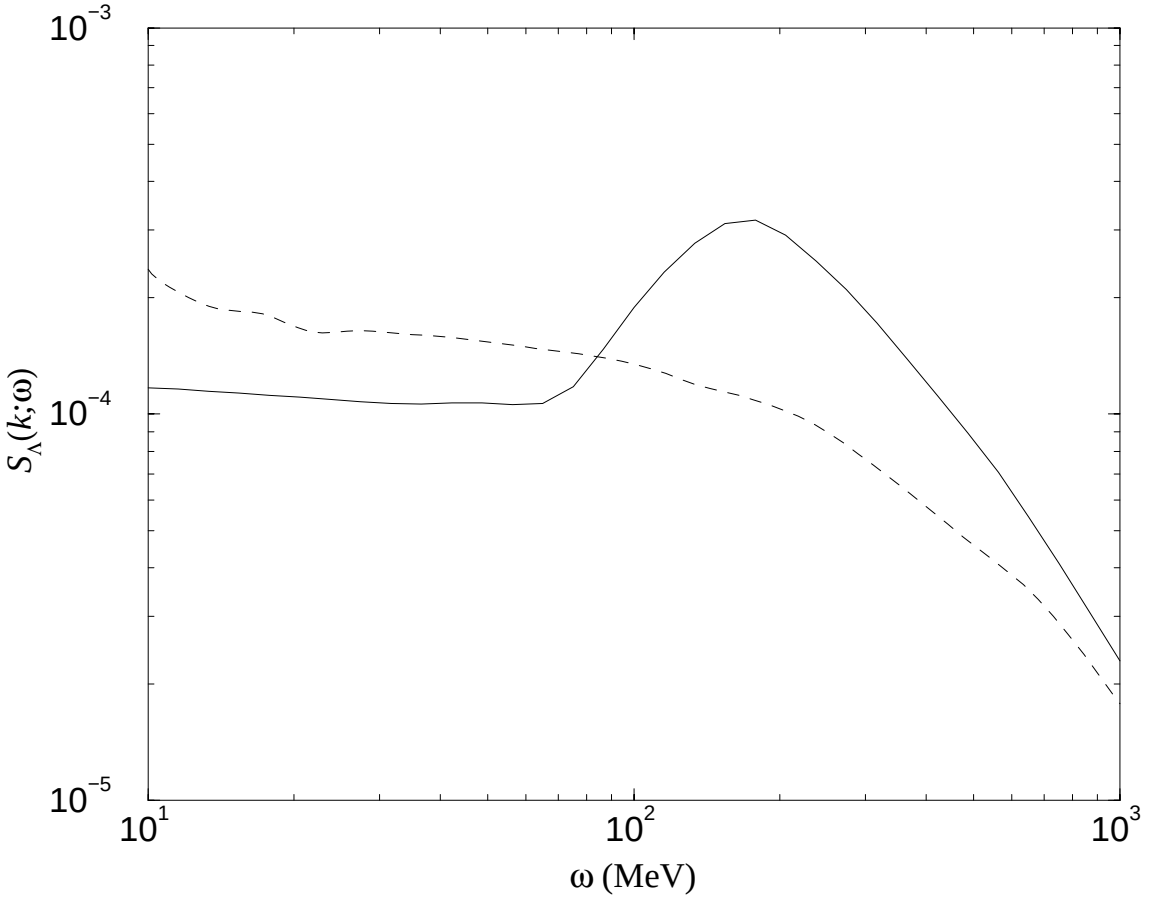

Figure 3.18: Spectral function in the vicinity of the ΣN threshold with ΛN-ΣN coupling (solid) and without (dashed). Note that the Λ threshold differs by about 30 MeV between the two cases. $k \approx 100$ MeV/c.

high energy ΛN two-particle states couple most strongly to high relative momentum and the strength of the potential matrix elements between these two states depends on the short-range characteristics of the two-body interaction. A harder core allows a stronger coupling between states and correspondingly more spectral strength at high energy (Section 3.4.1). The fact that structure in the high-energy region of the spectral function is primarily determined by the short-range behavior of the two-body interaction should be tempered by the knowledge that the short-range part of baryon-baryon interactions are poorly known. Typical potentials are designed, within whatever model, to fit only low-energy experimental data which does little to constrain the details of the repulsive core. This situation can be taken in two ways. On the one hand, the high-energy tail of the spectral function is just as uncertain in detail as the core of the interaction from which it is derived. On the other hand, it is also just as experimentally inaccessible and any observable which can be related to the detail of the tail in the spectral strength distribution could be used to gain insight into the behavior of the bare two-body interaction at short-range.

In Fig. 3.19 the similarities of the tail of the spectral strength for different momenta is illustrated.

3.4.1 Sum Rule

There exists a sum rule relating the energy weighted integral of the spectral function to the matrix elements of V in a very direct manner [36]. Writing the result from Ref. [36] for the case of a Λ in NM,

$$\int_{\varepsilon_F}^{\infty} d\omega\omega S_p^{\Lambda}(k;\omega) = \frac{k^2}{2m} + \frac{1}{(2\pi)^3}\int d^3k' n(k')\langle\vec{k}\vec{k'}|V|\vec{k}\vec{k'}\rangle, \tag{3.22}$$

where $n(k)$ is the occupation probability of the sp nucleon state with momentum k,

$$n(k) = \int_{\infty}^{\varepsilon_F} d\omega S_h^N(k,\omega). \tag{3.23}$$

Note that the two terms comprising the RHS of Eq. (3.22) are just the kinetic energy, $t(k)$, and the energy independent part of the self-energy, $\Sigma_V(k)$, respectively. The LHS of Eq. (3.22) may be formally divided into two pieces,

$$\int d\omega\omega S_p(k;\omega) \equiv \int d\omega\omega S_{qp}(k=0;\omega) + \int d\omega\omega S_{tail}(k=0;\omega), \tag{3.24}$$

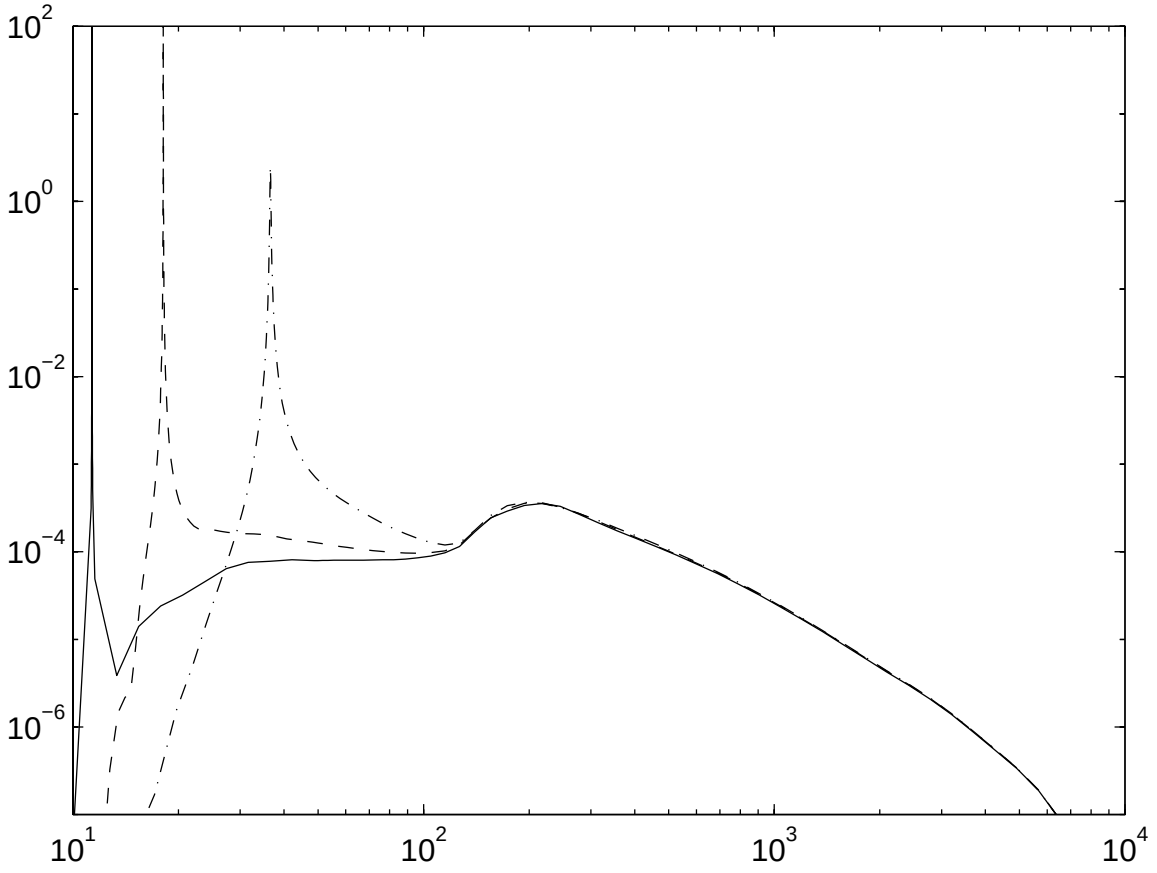

Figure 3.19: Spectral function for three values of k_Λ show the k-independence of the high energy. k = 10.0 MeV/c (solid curve), 110.0 MeV/c (dashed), 210.0 MeV/c (dash-dot).

the first corresponding to the qp peak and the second a "tail" primarily composed of strength at energies above ε_{qp}. Specializing to the case of $k = 0$ for simplicity, Eq. (3.22) becomes,

$$z(0)\varepsilon_{qp}(0) + I_{tail}(0) = \Sigma_V(0), \tag{3.25}$$

where,

$$\int d\omega\omega S_{tail}(k;\omega) \equiv I_{tail}(k), \tag{3.26}$$

and

$$\int d\omega\omega S_{qp}(k;\omega) = z(k)\varepsilon_{qp}(k). \tag{3.27}$$

Furthermore

$$S_{qp}(k;\omega) = z(k)\delta(\omega - \varepsilon_{qp}(k)) \tag{3.28}$$

has been used to obtain the contribution from the qp peak explicitly. The qp energy may be divided into two parts as in Eq. (3.13),

$$\varepsilon_{qp}(0) = \Sigma_V(0) + \Sigma_{2p1h}(0). \tag{3.29}$$

Now Eq. (3.25) may be rewritten as

$$z(0)\Sigma_V(0) + [z(0)\Sigma_{2p1h}(0) + I_{tail}(0)] = \Sigma_V(0). \tag{3.30}$$

For the lambda, $z(0) = 0.87$ which is close enough to unity that Eq. (3.30) implies

$$z(0)\Sigma_{2p1h}(0) \approx -I_{tail}(0). \tag{3.31}$$

This may be interpreted to mean that the coupling to 2p1h states at high energy shifts the qp peak from its HF value to lower energy. It may further be observed that for a strongly repulsive potential, $\Sigma_V(0)$ will be large and positive, as pointed out in Ref. [36]. For the NSC89 potential used in this work, the value is approximately 50 MeV. If the lambda is to be bound at the experimentally observed level of approximately 30 MeV, then the larger $\Sigma_V(0)$ is, the larger $\Sigma_{2p1h}(0)$ must be to compensate. This in turn requires a larger value of $I_{tail}(0)$ to satisfy the sum rule. This constitutes an indirect association between the strength of the repulsive bare interaction and the required distribution of strength at high energy.

Chapter 4

Non-Mesonic Weak Decay in Nuclear Matter

An overview of weak decay properties of the lambda is presented. The presence of a nuclear medium forces a shift from the mesonic to the non-mesonic decay mode, which becomes the focus for the rest of this work. In Section 4.2 the non-mesonic decay width is linked to the self-energy. Approximations are made which yield a simple expression for the decay width in terms of weak interaction matrix elements.

The weak meson-exchange potential is discussed in Section 4.3. The structure of the $\Lambda N \to NN$ interaction is examined and used to construct a $\Sigma N \to NN$ as required for the next chapter.

Results of a calculation of the lambda decay width without vertex form factors or initial-state correlations are presented in Section 4.4. Comparison is made with a key result from the literature as a check. Vertex form factors are included in Section 4.5 and their effects are discussed before moving on to a detailed examination of initial-state correlations in the next chapter.

4.1 Weak Decay of the Lambda

In free space the lambda decays primarily through the weak pionic modes (Fig. 4.1a),

$$\Lambda \to p + \pi^- + 38\,\mathrm{MeV} \quad (64\%) \tag{4.1}$$

$$\Lambda \to n + \pi^0 + 41\,\mathrm{MeV} \quad (36\%), \tag{4.2}$$

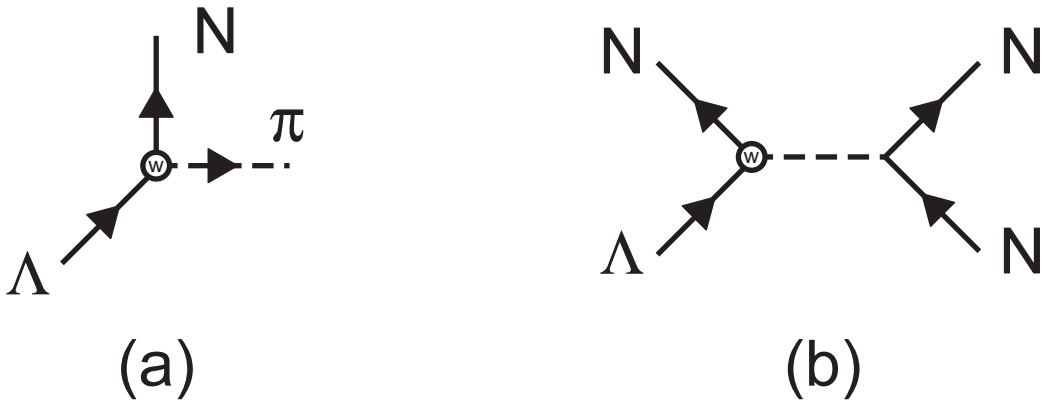

Figure 4.1: a. Mesonic decay. b. Non-mesonic decay.

with a lifetime of

$$\tau_\Lambda = 2.63\,\mathrm{x}10^{-10}\,\mathrm{s} \tag{4.3}$$

which corresponds to a decay width of

$$\Gamma_\Lambda = 2.5\,\mathrm{x}10^{-12}\,\mathrm{MeV}. \tag{4.4}$$

In the center-of-mass of the decaying lambda, the final state particles have momenta of about 100 MeV/c.

The presence of a nuclear medium forces fundamental changes in the lambda decay mode. If one imagines producing a lambda at rest in a Fermi gas of nucleons (k_F = 270 MeV/c), then the final state nucleon in Fig. 4.1a is Pauli blocked, resulting in complete suppression of the mesonic decay mode. In a realistic nuclear medium correlations among the nucleons "softens" the sharp momentum distribution characteristic of a Fermi gas [37]. Although this might seem to indicate a significant easing of the Pauli restriction, energy and momentum conservation requirements for the decay still ensure that the mesonic decay width in heavy hypernuclei is well below the free width [38].

If interactions between the lambda and nucleons in the medium are considered, then a new two-body decay mode becomes possible, Fig. 4.1b. The weak vertex is the same as in Fig. 4.1a, but now the meson is subsequently absorbed by a nucleon from the medium resulting in a net $YN \rightarrow NN$ transition. Since this non-mesonic mode involves a virtual meson exchange, the entire Λ-N mass difference of 176 MeV is made available for the kinetic energy of the final state particles. This translates

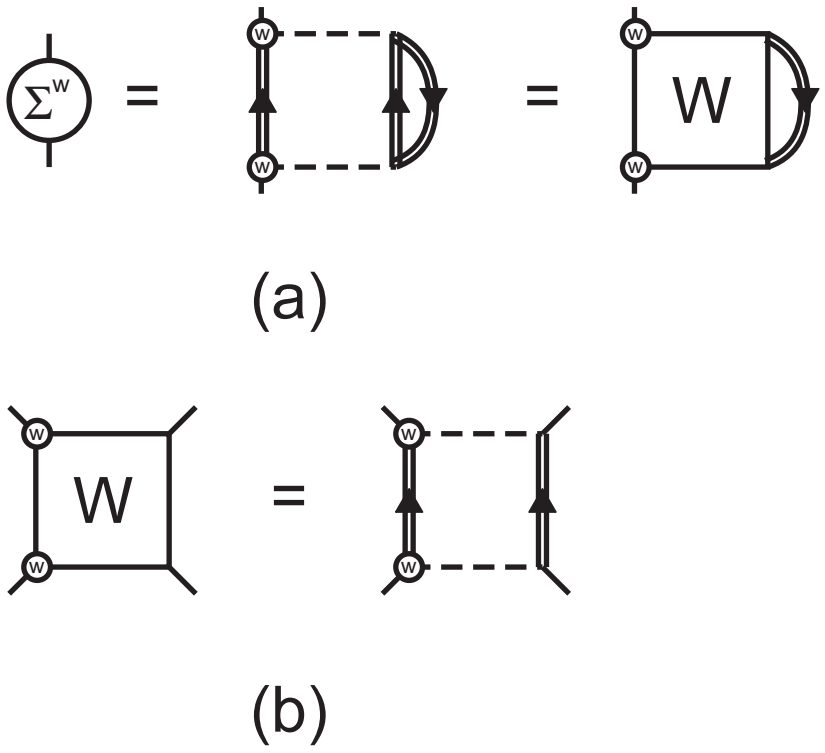

Figure 4.2: a. Lowest order self-energy diagram for non-mesonic lambda decay. External lines represent lambda particles and internal lines represent nucleons, which should, in principle, be dressed by the medium (double lines). b. Transition is second order in the weak interaction. Note: For strange meson exchange the weak and strong vertices are switched in both diagrams.

into a momentum of about 400 MeV/c for the final state nucleons, overcoming any Pauli blocking. Since the non-mesonic decay is catalyzed by a nucleon from the medium, the decay rate is expected to be proportional to the nuclear density. Conversely, the mesonic decay is suppressed at high nuclear densities and it follows that the non-mesonic mode will dominate for sufficiently heavy hypernuclei. Experimentally, it is found that the non-mesonic mode dominates for all but the very lightest hypernuclei [12].

4.2 Self-Energy and the Weak Decay Width

The non-mesonic decay width may be expressed in terms of the second order self-energy diagram [39] depicted in Fig. 4.2a,

$$\Gamma_{\Lambda}^{(nm)}(k) = -2\mathrm{Im}\ \Sigma_{\Lambda}^{(nm)}(k). \tag{4.5}$$

The self-energy is evaluated on-shell and averaged over the lambda spin,

$$\Sigma_{\Lambda}^{(nm)}(k) \equiv \frac{1}{2}\sum_{\alpha} \Sigma_{\Lambda}^{(nm)}(k\,\alpha; \varepsilon_{\Lambda}(k)), \tag{4.6}$$

where single-particle spin and isospin quantum numbers have been denoted by

$$|\alpha\rangle \equiv |s m_s\, t m_t\rangle. \tag{4.7}$$

Using standard Feynman diagram rules, the self-energy of Fig. 4.2a is given by

$$\Sigma_{\Lambda}^{(nm)}(k) = \frac{1}{2}\sum_{\alpha\beta}\int\frac{d\omega'}{2\pi i}\int\frac{d^3p}{2\pi^3}\langle\vec{k}\alpha;\vec{p}\beta|W(Q;\varepsilon_{\Lambda}(k)+\omega')|\vec{k}\alpha;\vec{p}\beta\rangle g_N(p;\omega'), \tag{4.8}$$

where the second order weak transition matrix (Fig. 4.2b) is defined by

$$\begin{aligned}\langle\vec{k}\alpha;\vec{p}\beta|W(Q;\Omega)|\vec{k}\alpha;\vec{p}\beta\rangle &= -\frac{1}{2}\sum_{\mu\lambda}\int d^3q_1\int d^3q_2\langle\vec{k}\alpha;\vec{p}\beta|V^{(w)}|\vec{q}_1\mu;\vec{q}_2\lambda\rangle \\ &\quad g_{NN}^{II}(\vec{q}_1,\vec{q}_2;\Omega)\langle\vec{q}_1\mu;\vec{q}_2\lambda|V^{(w)}|\vec{k}\alpha;\vec{p}\beta\rangle. \end{aligned}\tag{4.9}$$

The nucleon hole propagator is taken to have the form appropriate for a non-interacting particle,

$$g_N(p;\omega') = \frac{\Theta(k_F - p)}{\omega' - \varepsilon_N(p) - i\eta}. \tag{4.10}$$

Changing to total spin and isospin,

$$\vec{S} = \vec{s}_{\Lambda} + \vec{s}_N \tag{4.11}$$

$$\vec{T} = \vec{t}_{\Lambda} + \vec{t}_N, \tag{4.12}$$

and to total and relative momentum,

$$\vec{Q} \equiv \vec{k} + \vec{p} \tag{4.13}$$

$$\vec{q} \equiv \left(\frac{\mu_{\Lambda}}{m_N}\right)\vec{p} - \left(\frac{\mu_{\Lambda}}{m_{\Lambda}}\right)\vec{k}, \tag{4.14}$$

leads to

$$\frac{1}{2}\sum_{\alpha\beta}\langle\vec{k}\alpha;\vec{p}\beta|W(Q;\Omega)|\vec{k}\alpha;\vec{p}\beta\rangle = \frac{1}{4}\sum_{ST}\sum_{M_S M_S'}(2T+1)\langle\vec{q}SM_ST|W(Q;\Omega)|\vec{q}SM_S'T\rangle. \tag{4.15}$$

Making a change in the integration variable from $\vec{p}$ to $\vec{Q}$, performing the integration over the nucleon hole energy and expanding on a partial-wave basis transforms Eq. 4.8 into

$$\begin{aligned}\Sigma_\Lambda^{(nm)}(k) &= \frac{1}{4}\sum_{JLT}(2J+1)(2T+1)\int dQQ^2\int_{\xi_Q^{min}}^{1}\frac{d\xi_Q}{2} \\ &\quad \langle qJ(LS)T|W(Q;\varepsilon_\Lambda(k)+\varepsilon_N(p))|qJ(LS)T\rangle,\end{aligned} \tag{4.16}$$

where

$$q = q(k,Q,\xi_Q) \tag{4.17}$$

$$p = p(k,Q,\xi_Q), \tag{4.18}$$

ξ_Q is the cosine of the angle between $\vec{Q}$ and $\vec{k}$, and

$$\begin{aligned}\langle qJ(LS)T|W(Q;\Omega)|qJ(LS)T\rangle &= -\frac{1}{2}\sum_{L'}\int d^3q'|\langle qJ(LS)T|V^w|q'J(L'S')T\rangle|^2 \\ &\quad \bar{g}_{NN}^{II}(q',Q;\Omega).\end{aligned} \tag{4.19}$$

Eqs. 4.5, 4.16 and 4.19 yield the following expression for the decay width

$$\begin{aligned}\Gamma_\Lambda^{(nm)}(k) &= -\frac{1}{8}\sum_{JLL'T}(2J+1)(2T+1)\int dQQ^2\int_{\xi_Q^{min}}^{1}\frac{d\xi_Q}{2} \\ &\quad \int d^3q'|\langle qJ(LS)T|V^w|q'J(L'S')T\rangle|^2 \\ &\quad \text{Im }\bar{g}_{NN}^{II}(q',Q;\Omega).\end{aligned} \tag{4.20}$$

4.2.1 Approximate Expression for Weak Decay Width

To facilitate comparison with other work and simplify the numerical calculation, Eq. (4.20) is further modified in this section. The two-particle energy, $\Omega \equiv \varepsilon_\Lambda(k) + \varepsilon_N(p)$, is dependent on the integration variables through the nucleon hole momentum

as indicated in Eq. 4.18. The nucleon hole propagator in Eq. 4.10 contains a Pauli-function which restricts the nucleon momentum to a range below k_F. The two-nucleon propagator in Eq. 4.19 may be evaluated at a single energy if an average value of the nucleon momentum,

$$\bar{p} \equiv \frac{3k_F}{5} \tag{4.21}$$

is used as an approximation.

Using the non-interacting particle approximation for the intermediate nucleons, the angle-averaged two-particle propagator is

$$\bar{g}^{II}_{NN}(q,Q;\Omega) = \frac{-\Theta_{NN}(q,Q;k_F)}{\Omega - \bar{\varepsilon}_{NN}(q,Q) + i\eta}. \tag{4.22}$$

The imaginary part is then given by

$$\begin{aligned} \text{Im } \bar{g}^{II}_{NN}(q,Q;\Omega) &= \pi\delta(\Omega - \bar{\varepsilon}_{NN}(q,Q)) \\ &= \pi \left| \frac{\partial \bar{\varepsilon}_{NN}}{\partial q} \right|^{-1}_{q=q_0} \delta(q - q_0), \end{aligned} \tag{4.23}$$

where q_0 is defined by

$$\bar{\varepsilon}_{NN}(q_0, Q) \equiv \Omega + (M_\Lambda - M_N). \tag{4.24}$$

The two-particle energy, Ω, as determined from the initial ΛN state using the average momentum, $\bar{p}$, for a nucleon hole and $k = 0$ for the lambda is

$$\Omega = \varepsilon_\Lambda(k) + \varepsilon_N(\bar{p}) \approx -80\,\text{MeV}. \tag{4.25}$$

Using this value of the two-particle energy, the angle-averaged value of the final state two-nucleon energy is

$$\begin{aligned} \bar{\varepsilon}_{NN}(q_0, Q) &= 2\varepsilon_N(\bar{q}_N) \approx -80 + (1116 - 939)\,\text{MeV} \\ \varepsilon_N(\bar{q}_N) &\approx 52\,\text{MeV}, \end{aligned} \tag{4.26}$$

which yields a value of the relative momentum, $\bar{q}_N \approx 420$ MeV/c.

For a lambda at rest, the total momentum is just $Q = \bar{p} \approx 160$ MeV/c, which is sufficiently small compared to $\bar{q}_N$ that $\bar{q}_N(q_0;Q) \approx q_0$ to a good approximation.

The derivative of the two-nucleon energy in Eq. 4.23 may be evaluated as

$$\frac{\partial \bar{\varepsilon}_{NN}(q_0, Q)}{\partial q} \approx 2\frac{\partial \varepsilon_N(q_0)}{\partial q} \equiv 2\frac{q_0}{M_N^*}, \tag{4.27}$$

where a nucleon effective mass, M_N^*, has been introduced. The nucleon energy spectrum is

$$\varepsilon_N(q) \equiv t_N(q) + U_N(q), \tag{4.28}$$

where a Wood-Saxon parameterization is used to fit a numerically determined nucleon sp potential. The ratio, M_N/M_N^*, is approximately 1.37 for $q_0 = 420$ MeV/c, and goes to unity as q_0 becomes large enough that the potential term in Eq. 4.28 can be neglected.

The resulting expression for the imaginary part of the two-nucleon propagator is

$$\text{Im } \bar{g}_{NN}^{II}(q, \bar{Q}; \bar{\Omega}) = \frac{i\pi M_N^*}{2q_0}\delta(q - q_0), \tag{4.29}$$

and the W-matrix is

$$\langle qJ(LS)T|W(\bar{Q}; \bar{\Omega})|qJ(LS)T\rangle = -\frac{\pi M_N^* q_0}{4}\sum_{L'} |\langle qJ(LS)T|V^w|q_0J(L'S')T\rangle|^2. \tag{4.30}$$

The remaining dependence on the integration variables, Q and ξ_Q, can be eliminated by taking an average value of the relative momentum, $q(Q, \xi_Q; k)$, in the initial ΛN state. The imaginary part of the on-shell self-energy from Eq. 4.16 is

$$\begin{aligned} \text{Im } \bar{\Sigma}_\Lambda^{(nm)}(k) &= \frac{1}{4}\sum_{JLT}(2J+1)(2T+1) \\ &\quad \frac{k_F^3}{3}\left[-\frac{\pi M_N^* q_0}{4}\sum_{L'}|\langle \bar{q}J(LS)T|V^w|q_0J(L'S')T\rangle|^2\right] \end{aligned} \tag{4.31}$$

with $\bar{q} \approx 70$ MeV/c. This yields a simple approximation for the non-mesonic decay width

$$\bar{\Gamma}_\Lambda^{(nm)}(0) = \frac{3\pi^3}{16}(q_0 M_N^* \rho)\sum_{JLL'T}(2J+1)(2T+1)|\langle \bar{q}J(LS)T|V^w|q_0J(L'S')T\rangle|^2, \tag{4.32}$$

where ρ denotes the nuclear density. Calculation of the weak decay width is now reduced to evaluating a few matrix elements of the $\Lambda N \to NN$ transition potential. This approach is similar to that used in Ref. [40].

4.3 The Weak Meson-Exchange Potential

A weak meson-exchange interaction may be constructed formally in much the same way as the strong Nijmegen potential. Parameters of the strong interaction are determined by fits to YN scattering data (and NN scattering data through the use of flavor symmetries). This procedure determines coupling constants for the strong NNm vertices which may be carried over directly to the weak interaction. The only experimentally accessible quantities which can be readily related to needed weak coupling constants are hyperon decay amplitudes and these only provide information for the $YN\pi$ vertices. Exchange of heavier mesons occurs only as a virtual process and weak coupling constants must be derived in the context of some theoretical model.

Except where noted, $\Lambda N \to NN$ potential matrix elements are generated using a code provided by A. Parreño and A. Ramos based on their work as presented in Ref. [41]. Necessary $\Sigma N \to NN$ matrix elements are related to the $\Lambda N \to NN$ matrix elements as discussed in Section 4.3.2.

4.3.1 Weak Coupling Constants from Experimental Decay Amplitudes

The amplitude for the $Y \to N\pi$ decay may be written [42] as

$$M_{Y\to N\pi} = \bar{U}_N(A + B\gamma_5)\phi_\pi U_Y. \tag{4.33}$$

The hyperon and nucleon fields are represented by U_Y and U_N, and the pion field by ϕ_π. A and B are coupling constants for the Parity Violating (PV) and Parity Conserving (PC) amplitudes respectively. The partial width for this decay is found to be [42],

$$\Gamma_{Y\to N\pi} = \frac{q(E_N + m_N)}{4\pi m_Y}\left[|A|^2 + \left(\frac{E_N - m_N}{E_N + m_N}\right)|B|^2\right], \tag{4.34}$$

with

$$E_N = (m_N^2 + q^2)^{1/2}. \tag{4.35}$$

$Y \to N\pi$	A	B
$\Lambda \to p\pi^-$	1.47	-10.00
$\Lambda \to n\pi^+$	-1.07	7.15
$\Sigma^+ \to p\pi^0$	-1.48	-12.04
$\Sigma^+ \to n\pi^+$	0.06	-19.10
$\Sigma^- \to n\pi^-$	1.93	0.65

Table 4.1: Coupling constants in units of $G_F m_\pi^2 = 2.21\,\mathrm{x}10^{-7}$ are taken from Table XII-5 in Ref. [42], except the sign of the B values has been flipped to correspond with the Bjorken and Drell [43] sign convention for γ_5. Coupling constants are calculated from data in Ref. [44]. The latest experimentally determined lifetimes, from which these coupling constants are generated, have errors less than 1% [33].

The constants A and B are obtained from experimental partial decay rates (which determine only the magnitudes) and polarization measurements (required to determine the signs). These are listed in Table 4.1.

Although isospin is not conserved in weak interactions, it is empirically observed to change only in a restricted manner. As an example, Eq. 4.2 is consistent with a purely $T = 1/2$ final state even though the nucleon and pion can in principle also couple to $T = 3/2$. This empirical $\Delta T = 1/2$ rule is also observed in kaon and sigma hyperon decays [45]. Although the reason for this rule is not well understood, it may be incorporated in the weak decay formalism to find relationships among the coupling constants of Table 4.1, reducing the number of independent amplitudes from 10 to 6.

The Spurion Formalism

The $\Delta T = 1/2$ rule may be implemented by associating with each hyperon state, $|Y\rangle$, a corresponding "spurion" state [45],

$$|\tilde{Y}\rangle \equiv |\tfrac{1}{2}\,-\tfrac{1}{2}\rangle \otimes |Y\rangle. \tag{4.36}$$

Coupling to the "spurious" $|\frac{1}{2}\,-\frac{1}{2}\rangle$ isospin state enforces a change of $1/2$ in the total isospin while conserving charge. The resulting isospin structure of the lambda spurion is

$$\begin{aligned} |\tilde{\Lambda}\rangle &\equiv |\tfrac{1}{2}\,-\tfrac{1}{2}\rangle \otimes |0\,0\rangle \\ &= |\tfrac{1}{2}\,-\tfrac{1}{2}\rangle. \end{aligned} \tag{4.37}$$

Note that the lambda spurion has the same quantum numbers as a neutron. The spurion field may be used in place of the hyperon field to construct an isospin conserving weak vertex, effectively mimicking a $\Delta T = 1/2$ transition. The amplitude of Eq. 4.33, modified to make use of the isospin 1/2 spurion field, becomes

$$M_{\Lambda \to N\pi} = \bar{U}_N (A_\Lambda + B_\Lambda \gamma_5) \vec{\tau} \cdot \vec{\phi_\pi} U_{\tilde{\Lambda}}, \tag{4.38}$$

where the vertex operator is now explicitly an iso-scalar and A_Λ and B_Λ are isospin-independent "reduced" couplings for lambda decay. Aside from inclusion of the PV amplitude on the same footing as the PC amplitude, Eq. 4.38 for the weak vertex is exactly the same form as is typically used for the strong $NN\pi$ vertex.

The isospin structure of the sigma spurion is constructed in analogy with Eq. 4.37 (see Section C.1) and yields

$$\begin{aligned} |\tilde{\Sigma}^+\rangle &= \sqrt{\frac{2}{3}} |\tfrac{1}{2}\ \tfrac{1}{2}\rangle - \sqrt{\frac{1}{3}} |\tfrac{3}{2}\ \tfrac{1}{2}\rangle, \\ |\tilde{\Sigma}^0\rangle &= -\sqrt{\frac{1}{3}} |\tfrac{1}{2}\ -\tfrac{1}{2}\rangle + \sqrt{\frac{2}{3}} |\tfrac{3}{2}\ -\tfrac{1}{2}\rangle, \\ |\tilde{\Sigma}^-\rangle &= |\tfrac{3}{2}\ -\tfrac{3}{2}\rangle. \end{aligned} \tag{4.39}$$

Note that the sigma spurions are a combination of isospin 1/2 and 3/2 components. As an example, the $\tilde{\Sigma}^+$ has a $t = 1/2$ component with the same isospin as a proton and a $t = 3/2$ component with the isospin of a Δ^+ isobar. In light of this isospin structure, the weak iso-scalar vertex appropriate for sigma decay contains two terms,

$$\begin{aligned} M_{\Sigma \to N\pi} &= \bar{U}_N (A_\Sigma^{(1)} + B_\Sigma^{(1)} \gamma_5) \vec{\tau} \cdot \vec{\phi_\pi} U_{\tilde{\Sigma}} \\ &+ \bar{U}_N (A_\Sigma^{(3)} + B_\Sigma^{(3)} \gamma_5) \vec{T} \cdot \vec{\phi_\pi} U_{\tilde{\Sigma}}. \end{aligned} \tag{4.40}$$

The first term has the same form as Eq. 4.38 and accounts for decay from the isospin 1/2 component of the sigma spurion. The second term involves the isospin transition operator, T, in place of τ and accounts for decay from the isospin 3/2 component of the sigma spurion. The $\vec{T} \cdot \vec{\phi}$ operator is the form which is also used for a $\Delta N\pi$ vertex [46].

The spurion formalism implements the $\Delta T = 1/2$ rule, but also results in a weak decay amplitude with a compact isospin structure which describes the $YN\pi$

Decay	A	B
$\Lambda \to p\pi^-$	1.04	-7.07
$\Lambda \to n\pi^0$	1.07	-7.15
Average	1.05	-7.11

Table 4.2: Reduced coupling constants in units of $G_F m_\pi^2$ as determined from the lambda pionic decays.

vertex with a minimal number of coupling constants. These six independent constants (A_Λ, $A_\Sigma^{(1)}$, etc ...) may be determined from the data in Table 4.1 by evaluating the isospin operator for the various decay modes. Amplitudes for the two lambda decay channels may be expressed in terms of an isospin factor times an isospin-independent "reduced" amplitude,

$$a(\Lambda \to N\pi) \equiv \langle \tilde{\Lambda} | \vec{\tau} \cdot \vec{\phi} | N\pi \rangle \tilde{a}(\Lambda \to N\pi). \tag{4.41}$$

Evaluating the isospin factor for each decay channel (see Section C.2) leads to

$$a(\Lambda \to p\pi^-) = \sqrt{2}\tilde{a}(\Lambda \to N\pi), \tag{4.42}$$

$$a(\Lambda \to n\pi^0) = -\tilde{a}(\Lambda \to N\pi). \tag{4.43}$$

These relationships hold separately for the PV and PC amplitudes and allow the reduced coupling constants (Table 4.2) to be found.

For sigma decay, the amplitude for a particular decay channel may be expressed in terms of reduced amplitudes for each of the two isospin components which comprise the sigma spurion.

$$\begin{aligned} a(\Sigma \to N\pi) &\equiv a^{(1)}(\Sigma \to N\pi) + a^{(3)}(\Sigma \to N\pi) \\ &\equiv \langle \tilde{\Sigma} | \vec{\tau} \cdot \vec{\phi} | N\pi \rangle \tilde{a}^{(1)}(\Sigma \to N\pi) \\ &+ \langle \tilde{\Sigma} | \vec{T} \cdot \vec{\phi} | N\pi \rangle \tilde{a}^{(3)}(\Sigma \to N\pi). \end{aligned} \tag{4.44}$$

where

$$|\tilde{\Sigma}\rangle = \alpha |\tfrac{1}{2}\, m_{\tilde{\Sigma}}\rangle + \beta |\tfrac{3}{2}\, m_{\tilde{\Sigma}}\rangle, \tag{4.45}$$

1st Decay	2nd Decay	$A^{(1)}$	$A^{(3)}$	$B^{(1)}$	$B^{(3)}$
$\Sigma^+ \to p\pi^0$	$\Sigma^+ \to n\pi^+$	-0.57	1.52	-15.94	-1.47
$\Sigma^+ \to p\pi^0$	$\Sigma^- \to n\pi^-$	-0.70	1.36	-14.37	0.46
$\Sigma^+ \to n\pi^+$	$\Sigma^- \to n\pi^-$	-0.51	1.36	-16.73	0.46
Average		-0.59	1.41	-15.68	-0.18

Table 4.3: Reduced coupling constants in units of $G_F m_\pi^2$ as determined from the sigma pionic decays.

with constants α and β given in Eq. 4.39. Evaluating the isospin factor for each decay channel (see Section C.3) leads to

$$a(\Sigma^+ \to p\pi^0) = \sqrt{\frac{2}{3}}\tilde{a}^{(1/2)}(\Sigma \to N\pi) - \frac{\sqrt{2}}{3}\tilde{a}^{(3/2)}(\Sigma \to N\pi), \quad (4.46)$$

$$a(\Sigma^+ \to n\pi^+) = \frac{2}{\sqrt{3}}\tilde{a}^{(1/2)}(\Sigma \to N\pi) + \frac{1}{3}\tilde{a}^{(3/2)}(\Sigma \to N\pi), \quad (4.47)$$

$$a(\Sigma^0 \to p\pi^-) = -\sqrt{\frac{2}{3}}\tilde{a}^{(1/2)}(\Sigma \to N\pi) + \frac{\sqrt{2}}{3}\tilde{a}^{(3/2)}(\Sigma \to N\pi), \quad (4.48)$$

$$a(\Sigma^0 \to n\pi^0) = \frac{1}{\sqrt{3}}\tilde{a}^{(1/2)}(\Sigma \to N\pi) + \frac{2}{3}\tilde{a}^{(3/2)}(\Sigma \to N\pi), \quad (4.49)$$

$$a(\Sigma^- \to n\pi^-) = \tilde{a}^{(3/2)}(\Sigma \to N\pi). \quad (4.50)$$

Constants from two decay modes are required to determine both $T = 1/2$ and $T = 3/2$ sets of reduced coupling constants. Only three of the five possible decay modes given in Eqs. 4.46 - 4.50 have entries in Table 4.1. This is because the Σ^0 decays primarily through an electromagnetic mode which masks the weak mesonic decay. The three remaining decay channels represented by Eqs. 4.46, 4.47 and 4.50 still overdetermine the desired couplings. Determining couplings from each pair of decay channels leads to the results of Table 4.3. Note that there is more variation among the reduced coupling values for the sigma in Table 4.3 than for the lambda in Table 4.2. This suggests that the $\Delta T = 1/2$ rule is not as well satisfied for sigma decays.

4.3.2 Isospin Operators on the Baryon-Baryon Basis

The two-baryon state composed of a lambda spurion, $|\frac{1}{2}\,-\frac{1}{2}\rangle$, and a nucleon, $|\frac{1}{2},\pm\frac{1}{2}\rangle$, can couple to total isospin 1 or 0,

$$|\tilde{\Lambda}N\rangle = |\tfrac{1}{2}\,-\tfrac{1}{2}\rangle \otimes |\tfrac{1}{2}\,m_N\rangle = \delta_{m_N\,\frac{1}{2}}\left\{\frac{1}{\sqrt{2}}[|10\rangle - |00\rangle]\right\} + \delta_{m_N\,-\frac{1}{2}}|1{-}1\rangle. \tag{4.51}$$

If the $|\tilde{\Lambda}N\rangle$ state now undergoes a strong transition to the $|\tilde{\Sigma}N\rangle$ state, how much of the $|\tilde{\Sigma}N\rangle = |1m\rangle$ state is $|(\frac{3}{2}\,\frac{1}{2})1m\rangle$ and how much is $|(\frac{1}{2}\,\frac{1}{2})1m\rangle$? Each of these states decays differently, so the decomposition is important. This apparent ambiguity arises because the strong interaction used in this work (NSC89) does not treat the hyperons as spurions. For purposes of the strong interaction, the isospin of the ΛN state is

$$|\Lambda N\rangle = |00\rangle \otimes |\tfrac{1}{2}\,m\rangle = |\tfrac{1}{2}\,m\rangle, \tag{4.52}$$

and couples unambiguously to a ΣN state with the same isospin,

$$|\Sigma N\rangle = |\tfrac{1}{2}\,m\rangle. \tag{4.53}$$

This state can be decomposed into $|1m_\Sigma\rangle \otimes |\frac{1}{2}\,m_N\rangle$ product states. Now the sigma spurion can be introduced,

$$|1m_\Sigma\rangle \to |\tfrac{1}{2}\,-\tfrac{1}{2}\rangle \otimes |1m_\Sigma\rangle, \tag{4.54}$$

and coupled to the nucleon. This completes the $|\Sigma N\rangle \to |\tilde{\Sigma}N\rangle$ transformation in an unambiguous manner, and paves the way for calculation of the necessary $\tilde{Y}N \to NN$ weak transition matrix elements. The final result is,

$$\begin{aligned} |\Sigma N\rangle = |\tfrac{1}{2}\,m\rangle \to |\tilde{\Sigma}N\rangle \;&=\; \delta_{m\frac{1}{2}}\left\{\frac{2}{3}|(\tfrac{3}{2}\,\tfrac{1}{2})10\rangle - \frac{\sqrt{2}}{6}|(\tfrac{1}{2}\,\tfrac{1}{2})10\rangle - \frac{1}{\sqrt{2}}|(\tfrac{1}{2}\,\tfrac{1}{2})10\rangle\right\} \\ &+\; \delta_{m-\frac{1}{2}}\left\{\frac{\sqrt{8}}{3}|(\tfrac{3}{2}\,\tfrac{1}{2})1-1\rangle - \frac{1}{3}|(\tfrac{1}{2}\,\tfrac{1}{2})1-1\rangle\right\}. \end{aligned} \tag{4.55}$$

The details are presented in Appendix C.

Eq. 4.55 may be formally rewritten in the same form as Eq. 4.51 for the $|\tilde{\Lambda}N\rangle$ state,

$$|\tilde{\Sigma}N\rangle = \delta_{m\frac{1}{2}}\left\{\frac{1}{\sqrt{2}}[|10\rangle - |00\rangle]\right\} + \delta_{m-\frac{1}{2}}|1{-}1\rangle, \tag{4.56}$$

by defining,

$$|1m\rangle \equiv \sqrt{\frac{8}{9}}|(\tfrac{3}{2}\tfrac{1}{2})1m\rangle - \sqrt{\frac{1}{9}}|(\tfrac{1}{2}\tfrac{1}{2})1m\rangle, \tag{4.57}$$

$$|00\rangle \equiv |(\tfrac{1}{2}\tfrac{1}{2})00\rangle. \tag{4.58}$$

Matrix elements for π-exchange

The transition potential for weak decay via virtual pion exchange is given by [42]

$$V_\pi(\vec{q}) = -G_F m_\pi^2 \frac{g_{NN\pi}}{2M_N}\left(A + \frac{B}{2\bar{M}_Y}\vec{\sigma}_1\cdot\vec{q}\right)\frac{\vec{\sigma}_2\cdot\vec{q}}{q^2+\mu^2}\hat{T}_{12} \tag{4.59}$$

where

$$\bar{M}_Y \equiv \frac{M_N + M_Y}{2} \tag{4.60}$$

and

$$\hat{T}_{12} = \begin{cases} \vec{\tau}_1\cdot\vec{\tau}_2 & t = 1/2 \\ \vec{T}_1\cdot\vec{\tau}_2 & t = 3/2 \end{cases} \tag{4.61}$$

For the isospin transition operator, $\hat{T}$, used in this work, the matrix elements of $\hat{T}_{12}$ on the two-baryon basis are determined to be,

$$\langle(\tfrac{1}{2}\tfrac{1}{2})0m|\vec{\tau}_1\cdot\vec{\tau}_2|(\tfrac{1}{2}\tfrac{1}{2})0m\rangle = -3 \tag{4.62}$$

$$\langle(\tfrac{1}{2}\tfrac{1}{2})1m|\vec{\tau}_1\cdot\vec{\tau}_2|(\tfrac{1}{2}\tfrac{1}{2})1m\rangle = 1 \tag{4.63}$$

$$\langle(\tfrac{1}{2}\tfrac{1}{2})1m|\vec{T}_1\cdot\vec{\tau}_2|(\tfrac{3}{2}\tfrac{1}{2})1m\rangle = \frac{-4}{\sqrt{3}}. \tag{4.64}$$

These expressions, together with Eq. 4.59 and Eqs. 4.57 and 4.58 relate the $\Sigma N \to NN$ matrix elements to those for $\Lambda N \to NN$.

$$T=1: \quad \frac{\langle\tilde{\Sigma}N|V_{PV}|NN\rangle}{\langle\tilde{\Lambda}N|V_{PV}|NN\rangle} = \left[\sqrt{\frac{8}{9}}\frac{A_\Sigma^{(3)}\langle T=1|\vec{T}_1\cdot\vec{\tau}_2|T=1\rangle}{A_\Lambda\langle T=1|\vec{\tau}_1\cdot\vec{\tau}_2|T=1\rangle} - \sqrt{\frac{1}{9}}\frac{A_\Sigma^{(1)}}{A_\Lambda}\right] \tag{4.65}$$

$$= [-2.92 + 0.19] = -2.74$$

	π		κ	κ^*	
	$T=0$	$T=1$		spin-dep	spin-ind
PC	2.12	-0.76	-0.29	-0.16	0.58
PV	-0.56	-2.74	-0.30	-0.16	

Table 4.4: Ratio of the weak matrix elements $V_{\Sigma N\to NN}$ to $V_{\Lambda N\to NN}$ for meson exchanges for which coupling constants are available. The ratio is different for the spin-independent and spin-dependent parts of the central potential, but this only affects the PC part of the κ^* meson.

$$\frac{\langle\tilde{\Sigma}N|V_{PC}|NN\rangle}{\langle\tilde{\Lambda}N|V_{PC}|NN\rangle} = \frac{\bar{M}_\Lambda}{\bar{M}_\Sigma}\left[\sqrt{\frac{8}{9}}\frac{B_\Sigma^{(3)}\langle T=1|\vec{T}_1\cdot\vec{\tau}_2|T=1\rangle}{B_\Lambda\langle T=1|\vec{\tau}_1\cdot\vec{\tau}_2|T=1\rangle} - \sqrt{\frac{1}{9}}\frac{B_\Sigma^{(1)}}{B_\Lambda}\right] \quad (4.66)$$

$$= [-0.05 + -0.71] = -0.76$$

$$T=0: \quad \frac{\langle\tilde{\Sigma}N|V_{PV}|NN\rangle}{\langle\tilde{\Lambda}N|V_{PV}|NN\rangle} = \frac{A_\Sigma^{(1)}}{A_\Lambda} = -0.56 \quad (4.67)$$

$$\frac{\langle\tilde{\Sigma}N|V_{PC}|NN\rangle}{\langle\tilde{\Lambda}N|V_{PV}|NN\rangle} = \frac{\bar{M}_\Lambda}{\bar{M}_\Sigma}\frac{B_\Sigma^{(1)}}{B_\Lambda} = 2.12. \quad (4.68)$$

These ratios, collected in Table 4.4, show that the $\Sigma N \to NN$ transition is comparable to the $\Lambda N \to NN$ transition. Note that the $t = 3/2$ contribution to Eq. 4.66 is small compared to the $t = 1/2$ contribution. This is fortunate because $B_\Sigma^{(3)}$ is poorly determined (see Table 4.3).

Exchange of Strange Mesons

It is also possible to generate potentials for $\Sigma N \to NN$ transitions which proceed via an exchange of strange mesons (κ and κ^*). The connection to the related $\Lambda N \to NN$ potential is simpler in this case because the weak coupling is at the NN vertex, which is the same for each case. Only the strong $\Sigma N\kappa$ couplings are required to relate the two decay modes. Table 4.4 shows that unlike for the pion case, weak decays from a ΣN intermediate are always weaker than from a ΛN state when mediated by strange mesons. Furthermore, except for the spin-independent part of the κ^* central potential, all the ratios in Table 4.4 are negative. This results in a destructive interference between decays from different YN states. For κ^* the spin-dependent and spin-independent components of the $T = 1$ central channel interfere destructively and are delicately balanced against each other already in the $\Lambda N \to NN$ potential. So,

while this channel actually gets a boost from the ΣN decay mode, this can only occur because it was small (insignificantly so) to begin with.

Partial Widths

Assuming an initial s-state for the ΛN pair, six matrix elements contribute to the sum in Eq. 4.32:

$$\begin{aligned} T=0: \quad & {}^3S_1 \to {}^3S_1; \qquad {}^3S_1 \to {}^3D_1; \qquad {}^3S_1 \to {}^1P_1 \\ T=1: \quad & {}^1S_0 \to {}^1S_0; \qquad {}^1S_0 \to {}^3P_0; \qquad {}^3S_1 \to {}^3P_1. \end{aligned} \tag{4.69}$$

Partial widths for purely central ($S \to S$), tensor ($S \to D$) and PV ($S \to P$) decays may be defined by summing an appropriate subset of terms. Partial widths of definite isospin may also be defined by

$$\Gamma_{tot} = \frac{1}{2}\sum_T (2T+1)\Gamma_T. \tag{4.70}$$

These partial widths are closely related to an important observable: the ratio of the neutron-induced decay width, Γ_n, to the proton-induced decay width, Γ_p. From Eq. 4.51,

$$\begin{aligned} \Gamma_n &= \Gamma_1 \\ \Gamma_p &= \frac{1}{2}(\Gamma_0 + \Gamma_1). \end{aligned} \tag{4.71}$$

4.4 Lambda Decay Width: No Form Factor or Correlations

The simplest approximation to non-mesonic lambda decay in NM involves a weak interaction incorporating only π-exchange and no consideration of vertex Form Factors (FF) or correlations. This calculation has been performed previously by several other authors [40, 13] as a starting point on the way to more comprehensive treatments of the non-mesonic decay. Only transitions from an initial relative S-state are considered. The decay width is divided into central, tensor and parity-violating partial widths in Table 4.5. For comparison, results from Ref. [40] are presented in Table 4.7

FF	SRC	$S \to S$	$S \to D$	$S \to P$	Total
None	None	0.01	1.54	0.68	2.23
sing	None	0.18	0.69	0.31	1.18
dbl	None	0.27	1.01	0.45	1.74
dbl	f_{HC}	0.02	1.12	0.43	1.57
dbl	f_{SC}	0.11	0.96	0.39	1.46
dbl	tensor	0.21	1.05	0.43	1.69
dbl	sigma	1.30	1.75	0.35	3.40

Table 4.5: Partial decay widths in units of Γ_{free}, considering only π-exchange. Various combinations of FF and initial state correlations are considered, but no final state correlations.

FF	SRC	Γ_0	Γ_1	Γ_n/Γ_p
None	None	3.77	0.23	0.11
sing	None	1.88	0.16	0.16
dbl	None	2.75	0.24	0.16
dbl	f_{HC}	2.69	0.15	0.11
dbl	f_{SC}	2.39	0.18	0.14
dbl	tensor	2.87	0.17	0.11
dbl	sigma	6.36	0.15	0.05

Table 4.6: Partial decay widths in units of Γ_{free}, considering only π-exchange. Various combinations of FF and initial state correlations are considered, but no final state correlations.

FF	SRC	$S \to S$	$S \to D$	$S \to P$	Total
None	None	0.01	3.12	1.00	4.13

Table 4.7: Partial decay widths in units of Γ_{free} from Table II in Ref. [40]. Compare with first line of Table 4.5.

for what is essentially the same calculation.

It should be noted that in the absence of strong SRC, the central contribution to the total decay width is sensitive to the delta-function part of the π-exchange potential. Typically it is assumed that SRC cause the relative YN wavefunction to vanish at small distance, eliminating the delta-function contribution. As a result, it is often customary to exclude the delta-function part of the π-exchange potential, a priori, when calculating the decay width for the unphysical case of no FF and no SRC. This custom is followed in Tables 4.5, 4.6 and 4.7.

The evident discrepancy between the first line of Table 4.5 and Table 4.7 is the result of a number of conspiring factors. In order of importance:

- The decay width is directly proportional to the mass of the nucleon which "catalyzes" the decay (Eq. 4.32). In Ref. [40] the free nucleon mass is used, while Eq. 4.32 employs an effective mass which is 27% smaller.

- A factor of $\bar{M}_Y{}^{-1}$ appears in the PC term of the weak π-exchange potential, Eq. 4.59, which is the result of a non-relativistic reduction from a well-defined amplitude. In Ref. [40], the replacement $\bar{M}_Y \to M_N$ is made, resulting in a 20% increase in the PC partial widths.

- A slightly larger strong coupling constant is used in Ref. [40]; $g_{NN\pi} = 14.4$ compared to $g_{NN\pi} = 13.3$.

- A slightly larger weak PC coupling constant is used in Ref. [40]; $B_\pi = -7.21$ compared to $B_\pi = -7.15$.

Taking these differences into account, the results of Tables 4.5 and 4.7 can be reconciled to within 10%.

4.5 Vertex Form Factor

Without a FF, the π-exchange potential is singular at the origin, not merely in the central channel where there is a delta-function, but in the tensor channel as well. This unphysical behavior comes from treating the BBm vertex as pointlike. Inclusion of a FF damps the potential smoothly at high relative momentum, effectively taking into account the internal structure and finite size of the BBm vertex. A standard, mathematically convenient choice for the vertex FF is a monopole form,

$$\Phi(q^2; m_\pi, \Lambda_\pi) = \frac{\Lambda_\pi^2 - m_\pi^2}{\Lambda_\pi^2 + q^2}, \tag{4.72}$$

with a cutoff mass, $\Lambda_\pi = 1300$ MeV, taken from the Jülich YN potential [47]. Following Ref. [41], a monopole FF is used at each vertex. Other authors [40, 48] use a single monopole FF for both vertices, but also a smaller cutoff mass, $\Lambda_\pi = 626$ MeV. The effect of a FF, with these cutoff masses, on the various channels of the weak π-exchange potential can be seen directly in Figs. 4.3, 4.4 and 4.5.

The FF regularization effectively broadens the delta-function component of the central potential as can be inferred from Fig. 4.3. This yields a more diffuse interaction which will not be as sharply cut by a strong central correlation. Since the π-exchange potential is no longer singular after inclusion of a FF, contributions derived from the delta-function part of the central potential must be included. For this reason, no direct comparison for the central channel can be made between the results of Table 4.5 derived with and without a FF. Though less singular than the central potential, the tensor and parity-violating channels are also suppressed at short range ($r < 2$ fm) by the FF. This effect, seen clearly in Figs. 4.4 and 4.5, is mirrored in the results of Table 4.5.

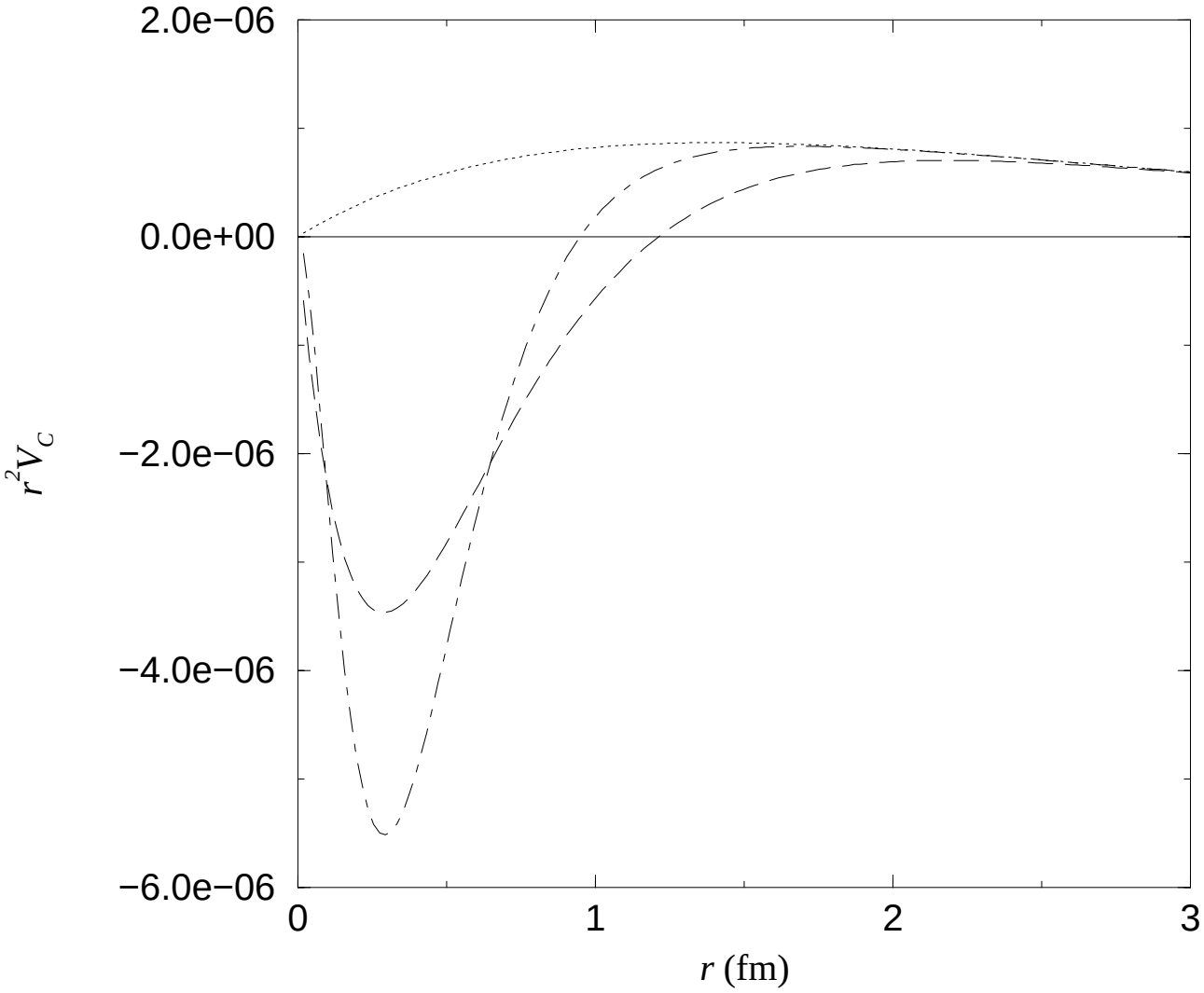

Figure 4.3: Weak π-exchange potential in the central channel. Each curve corresponds to a different choice of FF: none (dot), single monopole (dash) and double monopole (dot-dash). When comparing plots of the central potential with and without FF, it is important to remember that there is an attractive delta-function component to the potential without FF which is not shown in the above figure.

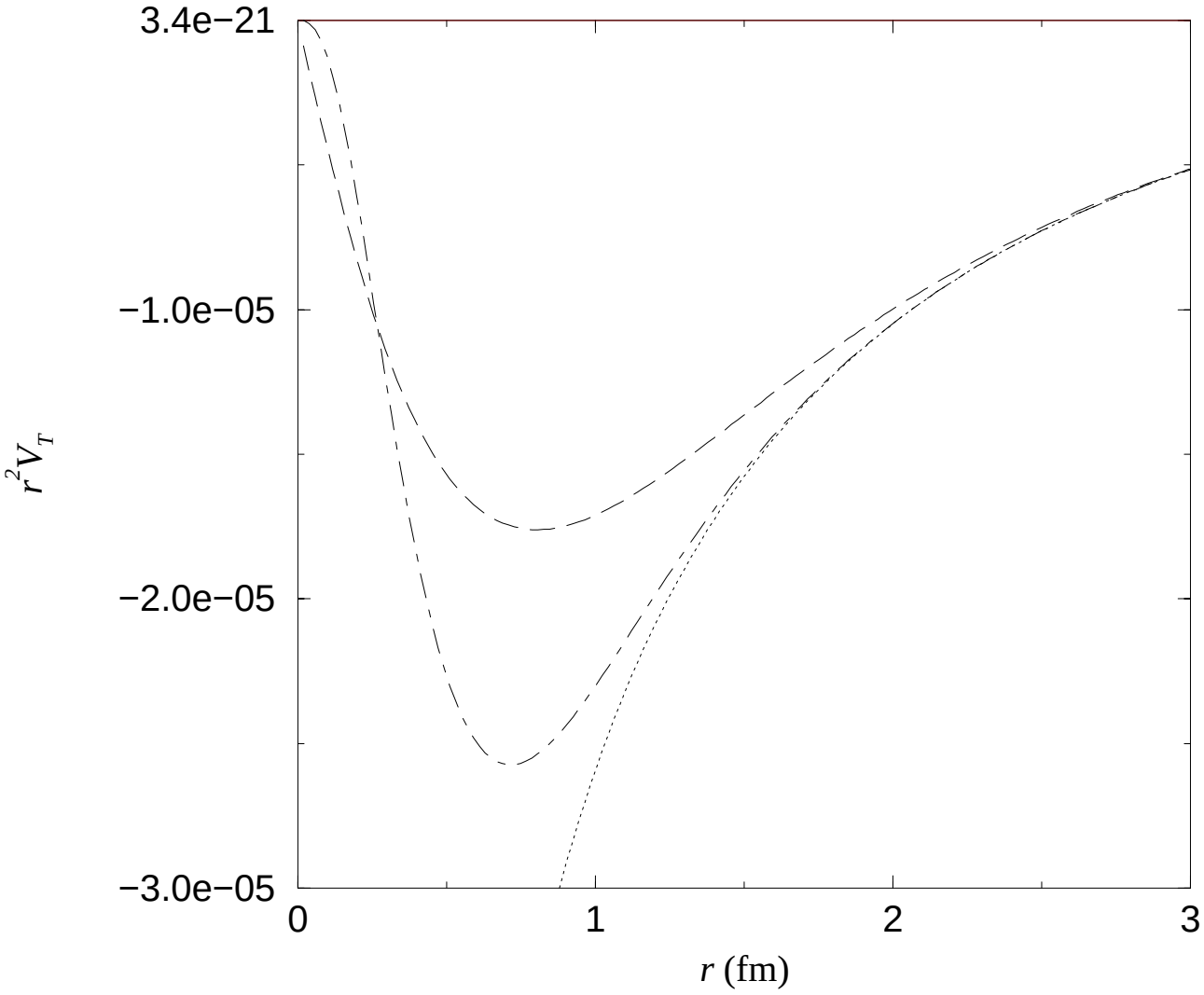

Figure 4.4: Weak π-exchange potential in tensor the channel. Each curve corresponds to a different choice of FF: none (dot), single monopole (dash) and double monopole (dot-dash).

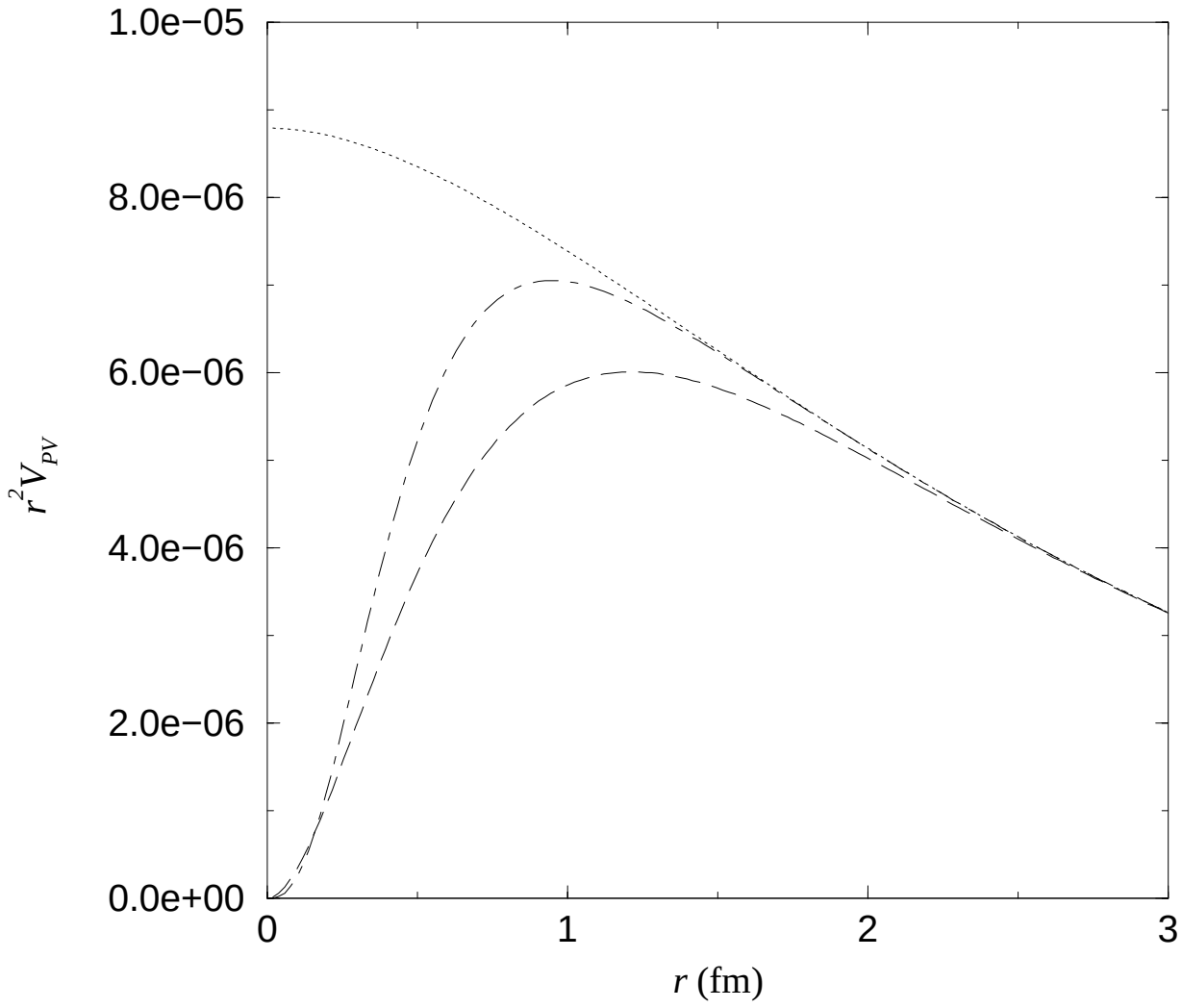

Figure 4.5: Weak π-exchange potential in the parity-violating channel. Each curve corresponds to a different choice of FF: none (dot), single monopole (dash) and double monopole (dot-dash).

Chapter 5

Effects of Strong Correlations on Weak Decay

Strong interactions result in the ΛN pair becoming correlated prior to non-mesonic decay. The situation is illustrated in Fig. 5.1 where an effective weak interaction is defined by allowing the initial ΛN pair to be correlated by the G-matrix effective strong interaction.

5.1 Simple Correlations

The momentum-space matrix elements which determine the decay width (Eq. 4.32) may be expressed in terms of wavefunctions for the initial and final states,

$$\langle q' J(L'S')T|V^w|qJ(LS)T\rangle = \int drr^2 \underbrace{\phi_{L'}(q'r)}_{\text{final}} \langle rJ(L'S')T|V^w|rJ(LS)T\rangle \underbrace{\phi_L(qr)}_{\text{initial}}. \tag{5.1}$$

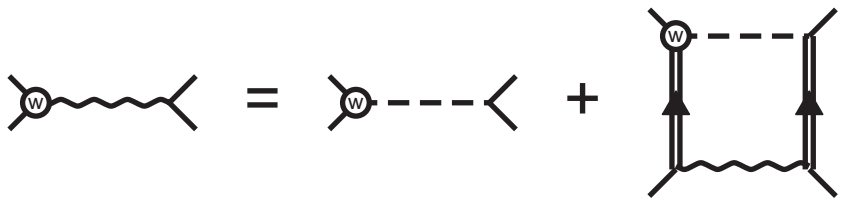

Figure 5.1: Effective weak interaction incorporating strong correlations in the initial ΛN state.

In a typical calculation of the decay width, correlations in the initial ΛN state are accounted for by making the replacement

$$\phi_L(qr) \rightarrow \Psi_L^{JT}(qr) \equiv f_L^{JT}(r)\phi_L(qr), \tag{5.2}$$

where a state-dependent correlation function, $f_L^{JT}(r)$, has been introduced.

As an example, Ref. [41] implements such a scheme to account for initial state correlations in the non-mesonic decay of p-shell hypernuclei. They use a correlation function obtained from a microscopic NM calculation [49] which utilizes the Nijmegen D hard-core potential. At least for this particular hard-core potential, a state-independent parameterization provides a good fit to correlation functions derived for either S-state. Because a potential with an infinite core is used in the derivation, the resultant correlation function vanishes at small distance, as can be seen in Fig. 5.2. The effect of this simple, "hard-core," correlation function, f_{HC}, on the decay width is presented in Table 4.5.

Correlation functions derived in a similar manner, but using the NSC potential, are plotted in Fig. 5.2 and their effect on the decay width is presented in Table 4.5 under the heading f_{SC}. The softness of the NSC potential means weaker correlation functions and different shapes for the two S-states.

The decay width can be sensitive to these modifications at small r because the weak interaction is intrinsically short range in nature. The high final state momentum sets a range on the order of

$$r_0 \sim \frac{\hbar c}{q_f} \approx 0.5 \text{ fm}. \tag{5.3}$$

The central potential is of shortest range and is expected to be most significantly affected by a correlation function. Table 4.5 shows that this is indeed the case, especially for f_{HC}, which virtually eliminates the contribution from the central channel. However, the total decay width is dominated by the $S \rightarrow D$ transition which is affected more modestly by the presence of a correlation function. The net result is a decrease in Γ_{tot} of 10-15% when a correlation function is used. Actually, the stronger correlation function, f_{HC}, decreases Γ_{tot} less than f_{SC}. The reason for this can be seen in Fig. 5.2. At short range (dominantly the central channel) f_{HC} cuts more sharply than f_{SC}, but at longer range (tensor channel) f_{HC} provides a compensating enhancement over f_{SC}.

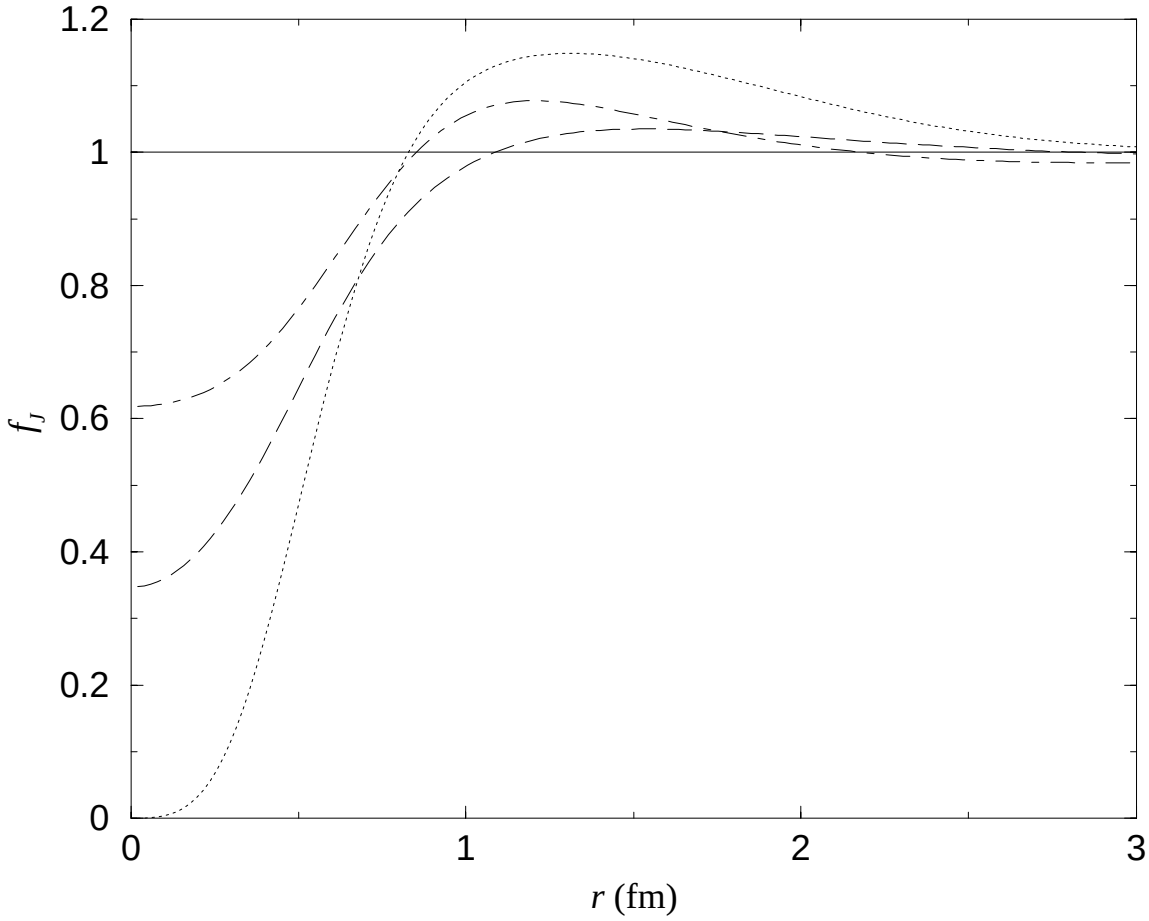

Figure 5.2: Correlation functions for the ${}^1S_0$ (dot-dash) and ${}^3S_1$ (dash) channels, together with the spin-independent parameterization (dot) used in ref. [41].

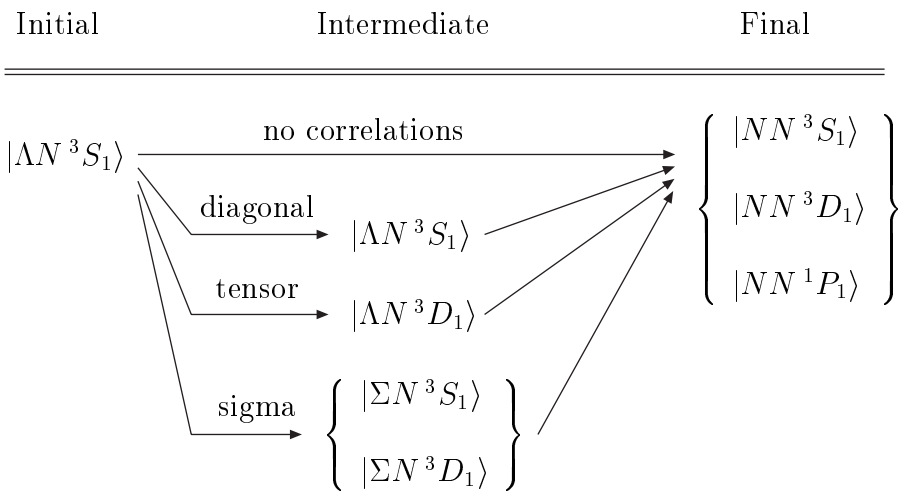

Figure 5.3: Strong correlations between the ΛN pair prior to weak decay leads to several intermediate states from which the weak transition can subsequently proceed.

5.2 Beyond Diagonal Correlations

The treatment of correlations presented in the previous section is conveniently simple to implement, but incomplete and ultimately inadequate for describing non-mesonic decay. The essential problem is the coupling of channels by the strong interaction which correlates the YN system. There is a significant tensor component to the NSC89 potential which mixes angular momentum states, and a strong coupling between ΛN and ΣN channels as well. A consequence of this strong coupling is the possibility of significant D-state and/or ΣN components mixed into the correlated initial ΛN S-state, as illustrated schematically in Fig. 5.3.

In order to determine what fraction of the correlated ΛN S-state is composed of "other" components and whether or not their admixture is large enough to result in a non-negligible contribution to the non-mesonic decay parameters, an examination of the correlated wavefunction is required.

5.2.1 Correlated Relative Wavefunction

The effective weak interaction (Fig. 5.1) may be expressed in operator form as

$$V^w_{eff} = V^w + V^w \frac{\Theta_{YN}}{\Omega - H_0 + i\eta} G. \tag{5.4}$$

When this operator acts on an uncorrelated ΛN state, $|\phi_i\rangle$, the expression

$$V^w_{eff}|\phi_i\rangle = V^w|\phi_i\rangle + V^w|\phi_j\rangle \frac{\Theta_{YN}}{\Omega - E_j + i\eta}\langle\phi_j|G|\phi_i\rangle \tag{5.5}$$

is obtained. The repeated index indicates a sum over a complete set of YN states, $\{|\phi_j\rangle\}$, which have been inserted in the last term. The correlated state, $|\Psi_i\rangle$, is naturally defined by,

$$V^w_{eff}|\phi_i\rangle \equiv V^w|\Psi_i\rangle, \tag{5.6}$$

which leads to the following expression for the correlated wavefunction

$$\begin{aligned} |\Psi_i\rangle &= |\phi_i\rangle + |\phi_j\rangle \frac{\Theta_{YN}}{\Omega - E_j + i\eta}\langle\phi_j|G|\phi_i\rangle \\ &\equiv (\delta_{ij} + c_{ij})|\phi_j\rangle. \end{aligned} \tag{5.7}$$

The implicit sum extends over all states which can couple to the initial state via the strong interaction. For example, if the initial state is $\Lambda N\ ^3S_1$, then the correlated state has four components, $\Lambda N\ ^3S_1$, $\Lambda N\ ^3D_1$, $\Sigma N\ ^3S_1$ and $\Sigma N\ ^3D_1$ (Fig. 5.3). In contrast, the simple correlation function of Section 5.1 yields a correlated wavefunction of the form

$$|\Psi_i\rangle = f\delta_{ij}|\phi_j\rangle, \tag{5.8}$$

and can only account for diagonal correlations, $i = j$, implicitly ignoring other terms which appear in Eq. (5.7).

5.2.2 Defect Wavefunction

A decision on which terms in Eq. (5.7) should be kept requires some measure by which they can be compared. It is convenient to isolate the parts of the correlated

wavefunction which are due solely to the presense of SRC by defining the defect state

$$\begin{aligned} |\chi_i\rangle &\equiv |\Psi_i\rangle - |\phi_i\rangle \\ &= c_{ij}|\phi_j\rangle. \end{aligned} \tag{5.9}$$

The defect wavefunction has the virtue of being non-zero only in a finite range where the strong SRC are in effect (Figs. 5.4 and 5.5). These components of the correlated wavefunction are integrable and are the basis for defining a measure of the strength of correlations in each channel: the wound integral [50]. Details of the wound integral calculation are presented in Appendix D.

The magnitude of the defect wavefunction corresponding to a given channel is not enough by itself to determine whether or not the channel in question will contribute significantly to the decay width. The relative strength and range of the weak potential for each channel is also critically important in determining its overall impact on the decay width.

5.2.3 Components of the Weak Effective Matrix Element

The effective weak matrix element is related to the correlated wavefunction by convolution with a matrix element of the bare weak interaction. Eq. (5.1), generalized for this case of an effective weak interaction containing a more intricately correlated initial state, becomes

$$\begin{aligned} &\langle q' J(L'S')T|V^{w_{eff}}_{YY'}(Q,\Omega)|qJ(LS)T\rangle = \\ &\quad \sum_{L''Y''} \int dr r^2 \phi_{L'}(q'r)\langle rJ(L'S')T|V^{w}_{Y'Y''}|rJ(LS)T\rangle \Psi^{JTYY''}_{LL''}(qr;Q,\Omega). \end{aligned} \tag{5.10}$$

The π-exchange portion of the ΣN-NN transition potential is derived in Section 4.3 and found to be comparable to the ΛN-NN potential (Table 4.4). Since this is the case, the transition through the intermediate ΣN state cannot be ignored and may yield a significant contribution to both the overall decay rate and its isospin structure. The integrand of Eq. (5.10) is split into two pieces, the correlated initial state wavefunction as one component and the balance of the integrand for the other. They are plotted together as a function of r in Figs. 5.6-5.8, one plot for each of the four possible YN states intermediate between an initial ΛN $^3S_1$ state and final NN $^3S_1$, $^3D_1$ and $^1P_1$ states. The amplitudes for decay through each available

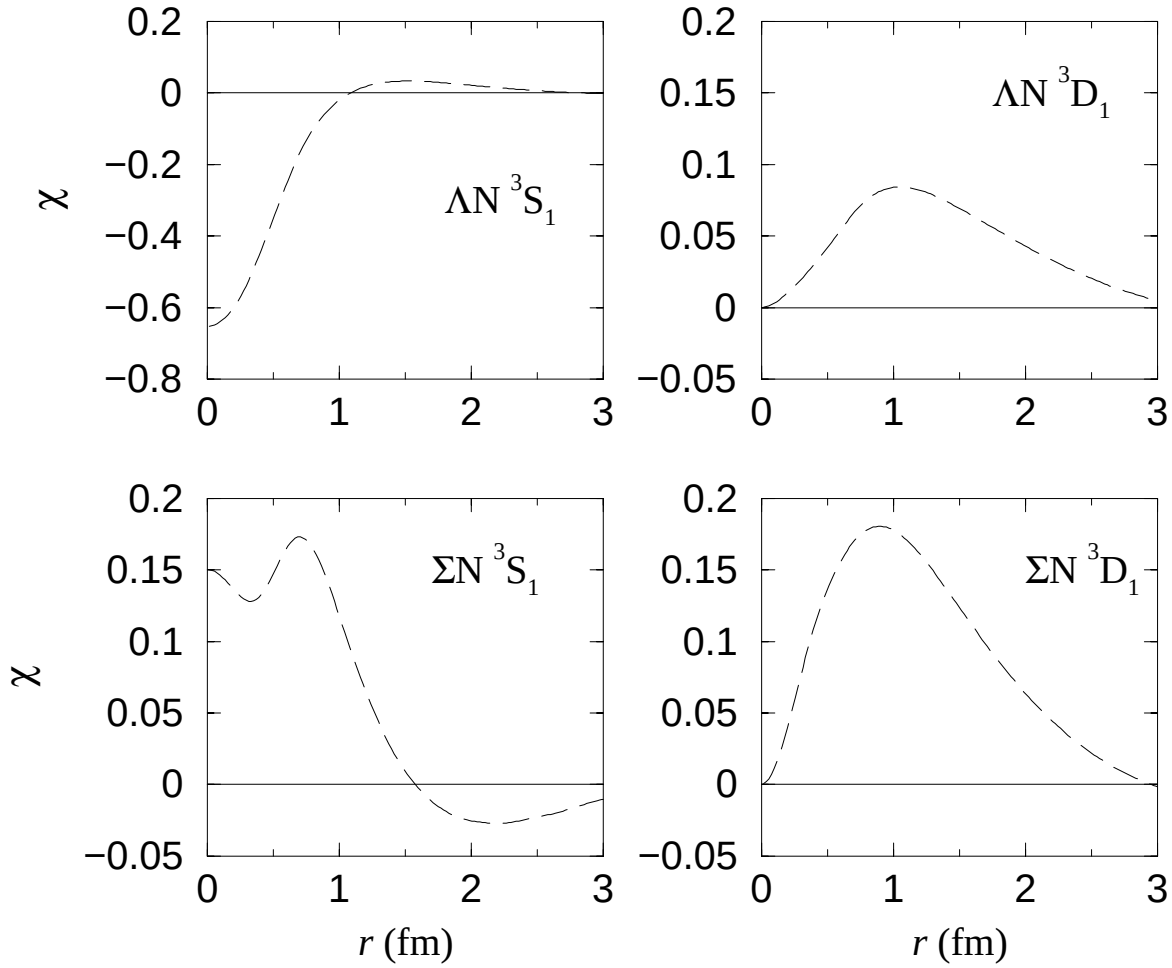

Figure 5.4: Defect wavefunction components of the correlated $\Lambda N\ ^3S_1$ state; evaluated at the average value of the ΛN relative momentum used in Section 4.2.1. For comparison, the uncorrelated wavefunction, $\phi(qr)$, is just a normalized spherical bessel function, $j_0(qr)$. Because of the small relative momentum, $q \sim 70$ MeV/c, $\phi(qr) \sim 0.8$ for the range shown.

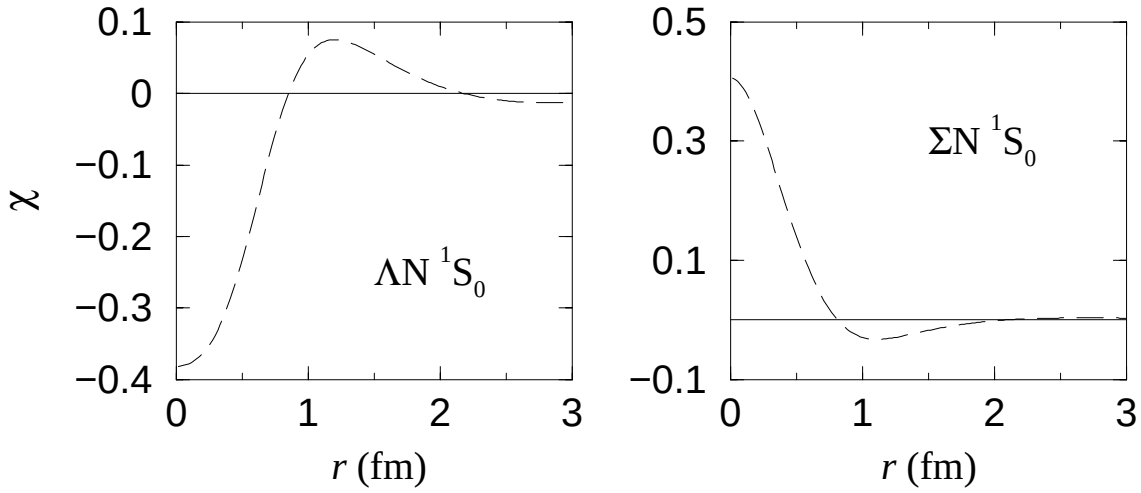

Figure 5.5: Defect wavefunction components of the correlated $\Lambda N\ ^1S_0$ state; evaluated at the average value of the ΛN relative momentum used in Section 4.2.1.

intermediate state are collected in Table 5.1. Also included is the amplitude for the direct decay, as would be expected from an uncorrelated state. The sum of these contributions determines the total decay amplitude for each channel.

For example, the first line of Table 5.1 breaks down the $^3S_1 \rightarrow {}^3S_1$ decay amplitude according to how much each portion of the correlated initial state contributes. The first column shows the decay amplitude in the absence of any correlations. The second column indicates a large reduction due to diagonal correlations, as would be observed with a simple correlation function, such as those discussed in Section 5.1. Likewise the first two entries in the second line show the uncorrelated decay amplitude for the direct tensor transition, $^3S_1 \rightarrow {}^3D_1$, and the small reduction caused by the diagonal SRC. The effects of these diagonal correlations is shown graphically in Figs. 5.6 and 5.7. Fig. 5.6 illustrates the large effect a wave-function depleted by correlations at short range has when paired with the very short range central potential. Conversely, Fig. 5.7 indicates the poor overlap between the "hole" in the correlated wave-function and the tensor potential, especially as modulated by the wavefunction for the final NN D-state. In general, Figs. 5.6-5.8 illustrate the similarity between the range over which the defect wave-function is non-zero and the range of the weak potential. This is a consequence of the fundamental similarities between the hypernuclear weak and strong interactions. Both share similar underlying meson-exchange structures which lead to comparable ranges. This range correspondence makes possible the significant

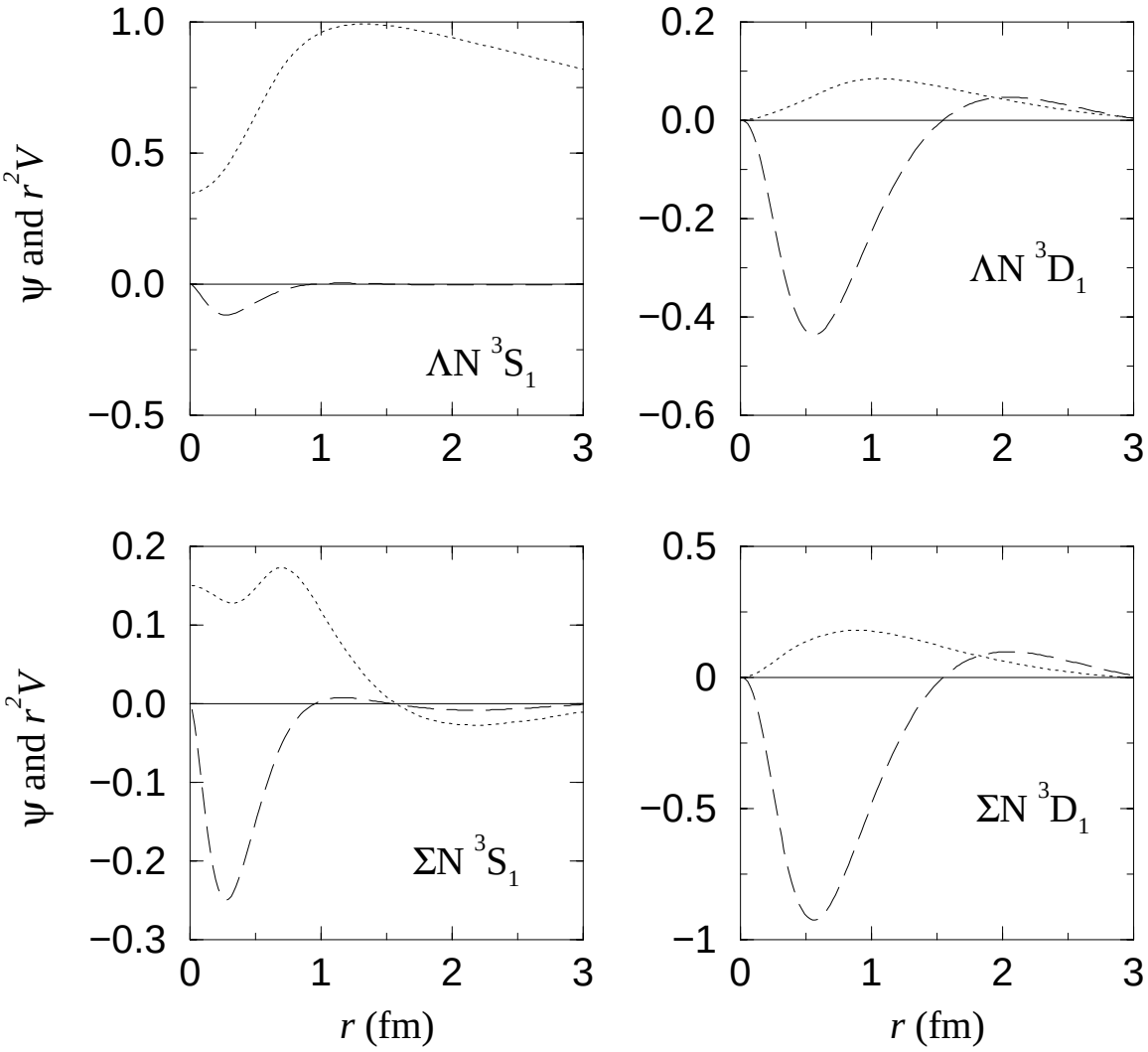

Figure 5.6: Product of the weak matrix element in r-space and the final state NN wavefunction, $\phi_0(qr)$, plotted together with correlated initial state wavefunctions. $\Lambda N\ ^3S_1 \to YN\ ^3L_1 \to NN\ ^3S_1$.

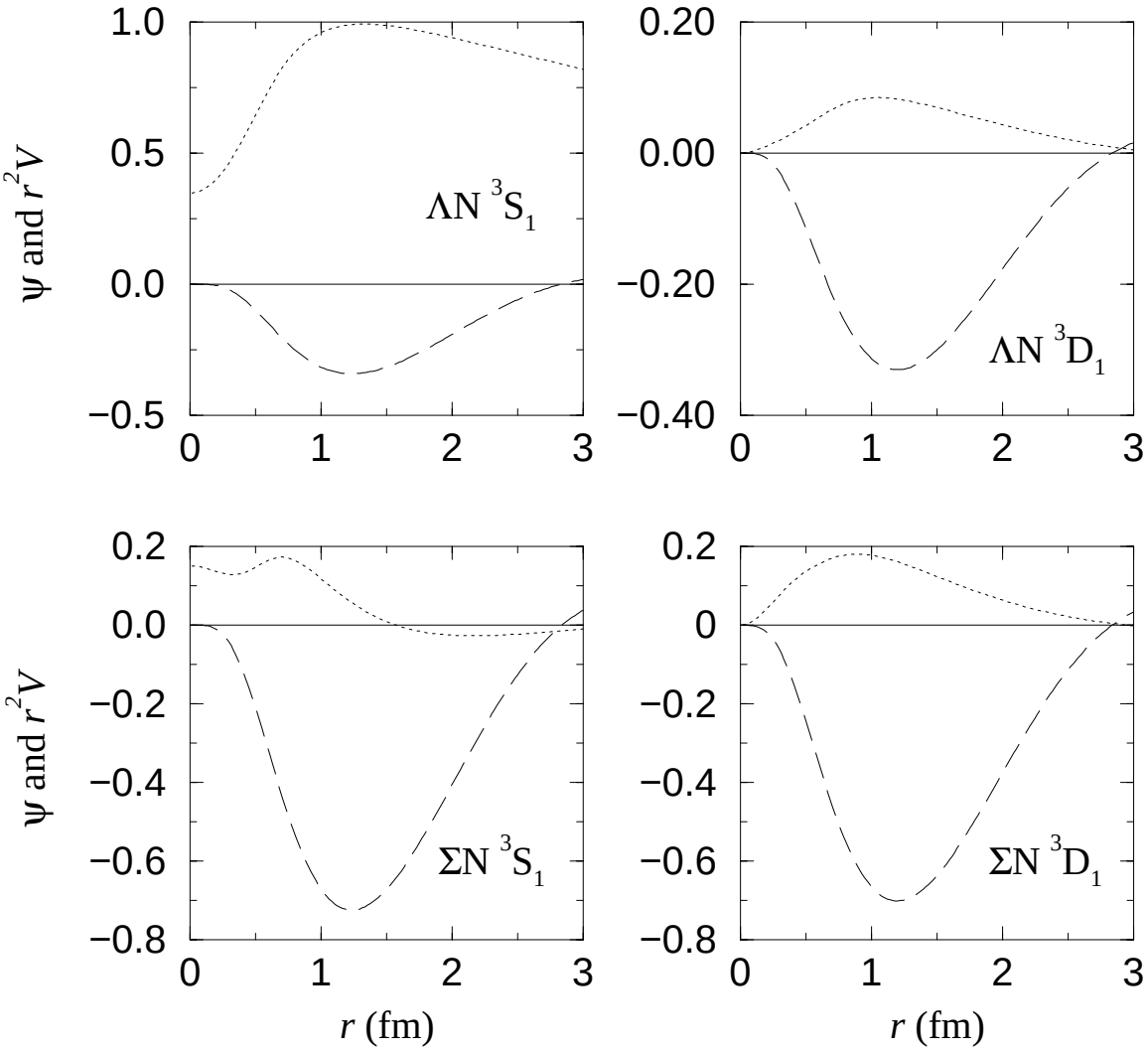

Figure 5.7: Product of the weak matrix element in r-space and the final state NN wavefunction, $\phi_2(qr)$, plotted together with correlated initial state wavefunctions. $\Lambda N\ ^3S_1 \to YN\ ^3L_1 \to NN\ ^3D_1$. Weak matrix elements have been scaled up by a factor of 3 relative to $S \to S$.

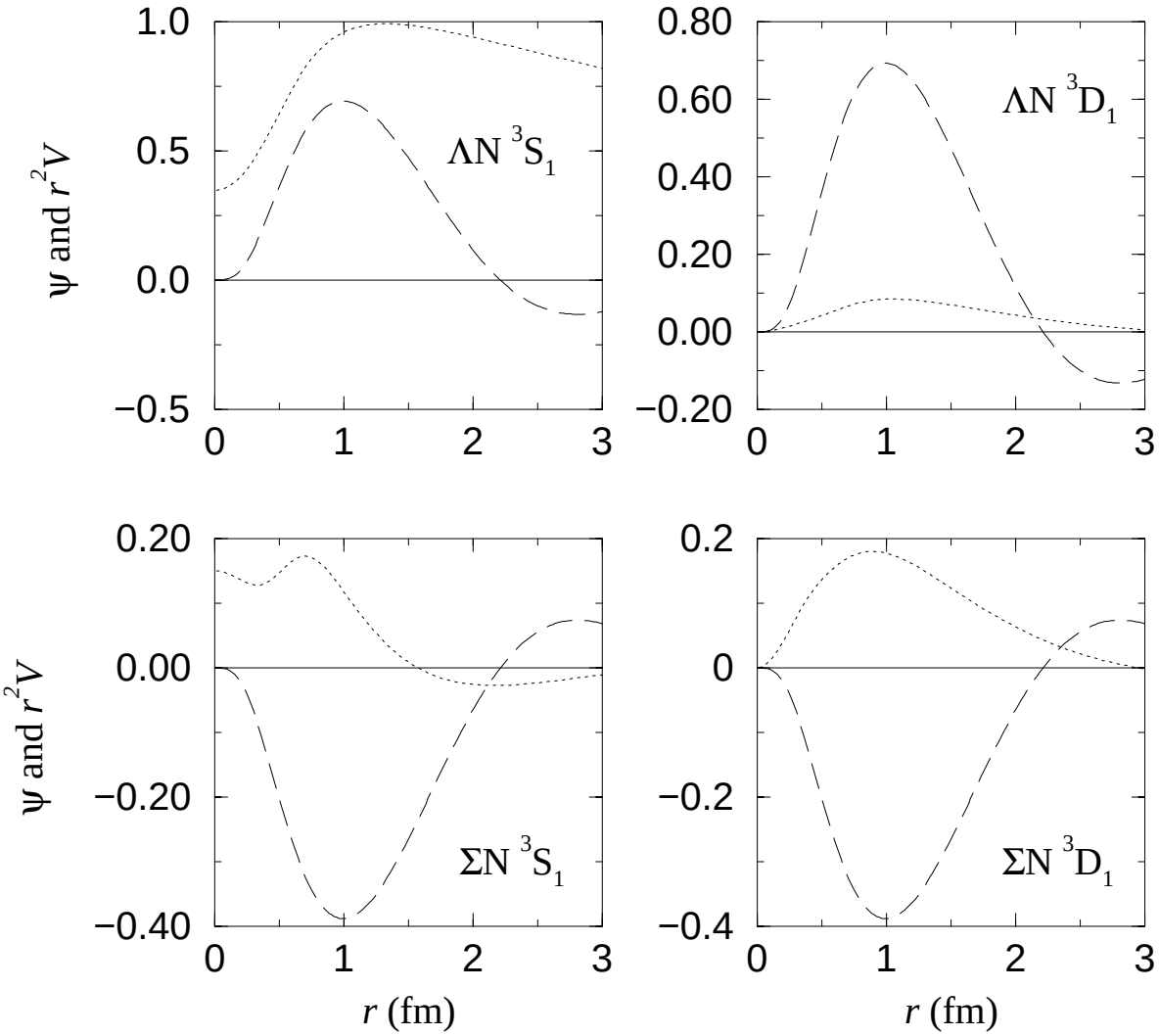

Figure 5.8: Product of the weak matrix element in r-space and the final state NN wavefunction, $\phi_1(qr)$, plotted together with correlated initial state wavefunctions. $\Lambda N\ ^3S_1 \rightarrow YN\ ^3L_1 \rightarrow NN\ ^1P_1$. Weak matrix elements have been scaled up by a factor of 10 relative to $S \rightarrow S$.

	No SRC	ΛN S	ΛN D	ΣN S	ΣN D	Total
${}^3S_1 \rightarrow {}^3S_1$	-2.82	1.29	-1.35	-0.84	-4.90	-8.62
${}^3S_1 \rightarrow {}^3D_1$	-7.73	0.20	-0.34	-0.93	-1.37	-10.16
${}^3S_1 \rightarrow {}^1P_1$	3.65	-0.29	0.43	-0.21	-0.44	3.13
${}^1S_0 \rightarrow {}^1S_0$	-2.82	0.81	0.00	0.49	0.00	-1.52
${}^1S_0 \rightarrow {}^3P_0$	2.11	-0.01	0.00	-0.07	0.00	2.03
${}^3S_1 \rightarrow {}^3P_1$	-1.72	0.14	0.10	0.49	-0.51	-1.50

Table 5.1: Each row corresponds to one of the six possible transitions from an initial ΛN S-state to a final NN state. For each channel, the matrix element for decay from an uncorrelated state is given first, and then the components of the effective weak matrix element corresponding to a transition through one of the four possible intermediate YN states, followed by the total. Matrix elements are given in units of $1.0\,\mathrm{x}10^{-13}$ MeV^{-2}.

contributions to the decay amplitude from decays proceeding through intermediate states as a result of SRC. As a result, at least some of the entries in Table 5.1 corresponding to correlation-induced transitions through intermediate YN states have large enough magnitudes to significantly impact the uncorrelated amplitudes.

5.2.4 Diagonal Correlations

The ΛN S-state column in Table 5.1 shows the effect of diagonal correlations on the decay amplitudes for each channel. As expected, these are substantial only for the $S \rightarrow S$ transitions where the weak potential and final state wavefunction are of shortest range. The decay amplitude in the ${}^3S_1 \rightarrow {}^3S_1$ channel is cut by almost 50% while the ${}^1S_0 \rightarrow {}^1S_0$ channel is cut by just under 30%. The difference is a result of the weaker correlations in the ${}^1S_0$ channel producing a smaller defect wavefunction.

5.2.5 Tensor Correlations

The strong tensor correlations present in the ΛN system lead to a small, relatively broad, D-state component in the initial state wavefunction as shown in Fig. 5.4. Although this piece of the correlated wavefunction is small, the tensor interaction coupling the intermediate D-state to the final S-state is considerably stronger than the corresponding central interaction as evidenced by Figs. 4.3 and 4.4. These offsetting factors combine to yield contributions to the decay amplitude of a magnitude similar to those arising from diagonal correlations but of opposite sign. The sign

difference is a result of the different origin of the ΛN S-state defect wavefunction compared to the other pieces of the correlated wavefunction. Diagonal correlations serve to cut strength from the initial channel, resulting in a negative amplitude for the defect wavefunction, and this strength subsequently reappears in the other coupled channels, manifest as wave function components with a positive amplitude. The result is that tensor correlations largely compensate the reductions brought about by diagonal correlations. Of course the tensor interaction does not operate in the $J = 0$ channels, so the $^1S_0$ channel still feels the effects of the diagonal correlations.

Including decays from the ΛN relative D-state leads to the "tensor" widths in Tables 4.5 and 4.6. Table 4.5 shows that decay widths cut by diagonal correlations are restored almost completely by tensor correlations. This is true for each of the composite channels ($S \to S$, $S \to D$ and $S \to P$) as well as the total decay width. Though diagonal correlations lower the total decay width by 15% from the uncorrelated value, inclusion of tensor correlations leaves a reduction of only 2-3%. To the extent that initial state correlations are important at all at the level of diagonal correlations, tensor correlations will be just as important, and work to counter any suppression of the decay amplitude caused by diagonal correlations. This confirms that the simple correlation function, as defined in Eq. (5.8) does not lead to an adequate representation of the correlated wavefunction. If initial state correlations in the ΛN system are important enough to be considered, then a more general method of including correlations, Eq. (5.7), should be implemented.

5.2.6 Decays from an Intermediate ΣN State

In the previous section, it was shown that tensor correlations in the ΛN sector are strong enough to demand a ΛN D-state component when constructing a correlated initial state wavefunction. Correlations are even stronger between the initial ΛN S-state and ΣN intermediate states. The ΣN components of the correlated initial state wavefunction are comparable to and even slightly larger than the ΛN D-state component (Fig. 5.4). Furthermore, the weak transition from these ΣN intermediate states is more than twice as strong as the corresponding $\Lambda N \to NN$ decay in several channels. The result is a large amplitude for decays proceeding through the ΣN intermediates, particularly for the $T = 0$ channels where the tensor interaction plays such a dominant role. Including decays from intermediate ΣN states leads to the

"sigma" widths in Tables 4.5 and 4.6. The key feature to note is a *doubling* of the total decay width when sigma correlations are included. Both the $S \to S$ and $S \to D$ channels see significant increases, especially the central channel, which now rivals the tensor channel. The central channel sees such a large boost from the presence of ΣN intermediates because of the *two* tensor transitions involved in the multi-step decay. Conversion to a ΣN intermediate via the strong tensor force is followed by a weak decay which also involves a tensor force,

$$\Lambda N\, {}^3S_1 \xrightarrow{s} \Sigma N\, {}^3D_1 \xrightarrow{w} NN\, {}^3S_1. \tag{5.11}$$

In contrast, the net $S \to D$ channel involves only a single tensor transition, weak or strong depending on whether the intermediate is an S-state or a D-state. Note that this increase comes from the $T = 0$ channels, and from Table 4.4 the $\Sigma N \to NN$ potential has the same sign as its $\Lambda N \to NN$ counterpart. As a result, amplitudes for decays in the two $T = 0$ channels add constructively.

5.3 Exchange of Heavy Mesons

5.3.1 Interference: Pion and Kaon

At the beginning of this chapter, non-mesonic decay via virtual pion exchange was discussed. If the exchange of heavier mesons is considered, the decay properties of the lambda can be altered. Strange mesons, in particular, are expected to contribute to a higher Γ_n/Γ_p ratio by virtue of their isospin structure. Table 5.2 shows that the kaon by itself has a ratio of over 1 before correlations are considered, and dropping only to 0.65 even after correlations have taken their toll. These values lie in a range comparable to experimental values (Table 5.6). This is in contrast to the pion-only results, which are substantially lower than both the kaon and experimental ratios, primarily because of the strong pionic tensor component. Unfortunately, hope of bridging the gap between the pion numbers and experimental decay parameters by adding kaon decay into the mix are hampered by the relative weakness of the kaon potential. Though the $T = 1$ decay channels are comparable to the $T = 0$ channels for the kaon, resulting in a relatively large Γ_n/Γ_p ratio, they are both dominated by the $T = 0$ channels of the pion, which are fed by its large tensor potential. This can be clearly seen in Fig. 5.11 where the pion dominates the kaon in the tensor channel,

Mesons	SRC	Γ_0	Γ_1	Γ_n/Γ_p
π	None	2.75	0.24	0.16
π	f_{SC}	2.39	0.18	0.14
π	tensor	2.87	0.17	0.11
π	sigma	6.36	0.15	0.05
κ	None	0.11	0.14	1.12
κ	f_{SC}	0.09	0.06	0.81
κ	tensor	0.11	0.06	0.68
κ	sigma	0.09	0.04	0.65
$\pi + \kappa$	tensor	4.10	0.23	0.11

Table 5.2: Partial decay widths in units of Γ_{free}, for the pion and kaon. A double monopole FF is used in all cases together with various choices for the initial state correlations. No final state correlations are included.

Meson	$S \to S$	$S \to D$	$S \to P$	Total
π	0.27	1.01	0.45	1.74
η	0.01	0.01	0.01	0.03
κ	0.19	0.04	0.05	0.27
ρ	0.13	0.04	0.03	0.20
ω	0.58	0.01	0.01	0.60
κ^*	0.48	0.03	0.21	0.72
ALL	5.06	0.66	1.50	7.22

Table 5.3: Partial decay widths in units of Γ_{free}, considering different meson-exchanges. A double monopole FF is used in all cases. No initial or final state correlations are included.

especially once convolution with the $l = 2$ final state wave function is considered (Fig. 5.15).

5.3.2 No Correlations

Before correlations are considered, mesons beyond the pion alter the decay widths significantly. As shown in Table 5.3, the central, $S \to S$, channels are increased the most by the new decays, raising this partial width by a factor of almost 20 from 0.27 for the pion alone to over 5.0 for the collection of mesons taken together. This strong constructive interference shows through in Fig. 5.9, where the weak potential for all mesons in the $T = 1$ central channel are plotted. The $T = 0$ central potentials are plotted in Fig. 5.10, though they do not contribute significantly to the total $S \to S$ decay width. In this case, destructive interference results in a contribution to the

decay width well below that of the pion alone. Many mesons have substantial decay widths in these channels, and they interfere constructively to dominate the overall decay in the absence of moderating SRC.

Though no individual meson approaches the strength of the the pionic tensor interaction, destructive interference cuts this partial width in half nonetheless (Fig. 5.10). Likewise for the parity violating channels (Figs. 5.12, 5.13 and 5.14), though here the κ^* meson does possess a strength comparable to the pion. The final result is that the central channels now dominate over the tensor channel and the total decay width is increased by over a factor of four. Note that this dominance of the decay width by the central channels, specifically the $T = 1$ channel, leads to a dramatic increase in the Γ_n/Γ_p ratio. The ratio increases to 1.01, seeming to validate the inclusion of mesons beyond the pion for the purpose of reaching an agreement between experiment and theory. However, it will be seen that this agreement only lasts until initial-state correlations are considered.

5.3.3 Diagonal Correlations

Inclusion of initial state correlations at the level of diagonal correlations changes this picture. Mesons heavier than the pion are likewise of shorter range than the pion, and feel the cut of SRC more strongly (Table 5.4). The result is a reduction in the partial width involving the central channels by more than a factor of 3, bringing them more in line with other contributing channels (tensor and PV). This is in contrast to the pion only case where diagonal correlations cut an already small central contribution. The parity-violating partial width is also reduced by a factor of 1/3 and the tensor width is essentially unaffected. Now the central channels are still the largest contribution, and the parity-violating (tensor) channels are still larger (smaller) respectively than for the pion-only case. The result of diagonal correlations is a reduction of the overall width by more than half, yet still leaving it more than twice the size of the decay width for the pion alone at this level of correlation.

5.3.4 Tensor Correlations

Tensor correlations have only a modest effect, as was the case for the pion alone.

Mesons	SRC	$S \to S$	$S \to D$	$S \to P$	Total
π	None	0.27	1.01	0.45	1.74
π	f_{SC}	0.11	0.96	0.39	1.46
π	tensor	0.21	1.05	0.43	1.69
π	sigma	1.30	1.75	0.35	3.40
ALL	None	5.06	0.66	1.50	7.22
ALL	f_{SC}	1.51	0.68	1.10	3.29
ALL	tensor	1.50	0.72	1.28	3.50
ALL	sigma	1.43	1.30	1.07	3.80

Table 5.4: Partial decay widths in units of Γ_{free}, considering different meson-exchanges. A double monopole FF is used in all cases together with various choices for the initial state correlations. Note that in the last line, decays from intermediate ΣN states are included only for those mesons for which appropriate coupling constants are available: π, κ, and κ^*. No final state correlations are included.

5.3.5 Sigma Correlations

Opening the $\Sigma N \to NN$ decay channel via the κ and κ^* mesons in addition to the direct path from the ΛN initial state also only has a modest affect on the overall decay width, unlike what is observed for the pion alone. The tensor decay width is increased by almost a factor of 2, even more than in the case of the pion alone, but the width derived from the central channels actually decreases. This is in contrast to the marked increase for the pion alone, which sees the central channel rise from insignificance to rival the tensor channel when decays from the ΣN intermediate are considered. The difference can be attributed to two things. Though the $\Sigma N \xrightarrow{\pi} NN$ decay is a very strong decay channel which serves to increase the tensor partial width, this channel is no longer dominant, so its increase does not affect the overall width as much. The central channel also feels this particular decay channel strongly, but interference with other mesons serves to wash out its contribution, unlike for the case of the pion alone. In the end, the overall decay width sees a modest 10% increase. This in comparison to the 100% jump this new channel brings to the pion decay mode.

5.3.6 Comparison: Finite Nuclei

Experimental results are available for medium and to a lesser extent heavy nuclei. Theoretical calculations have also been performed directly for finite systems, such

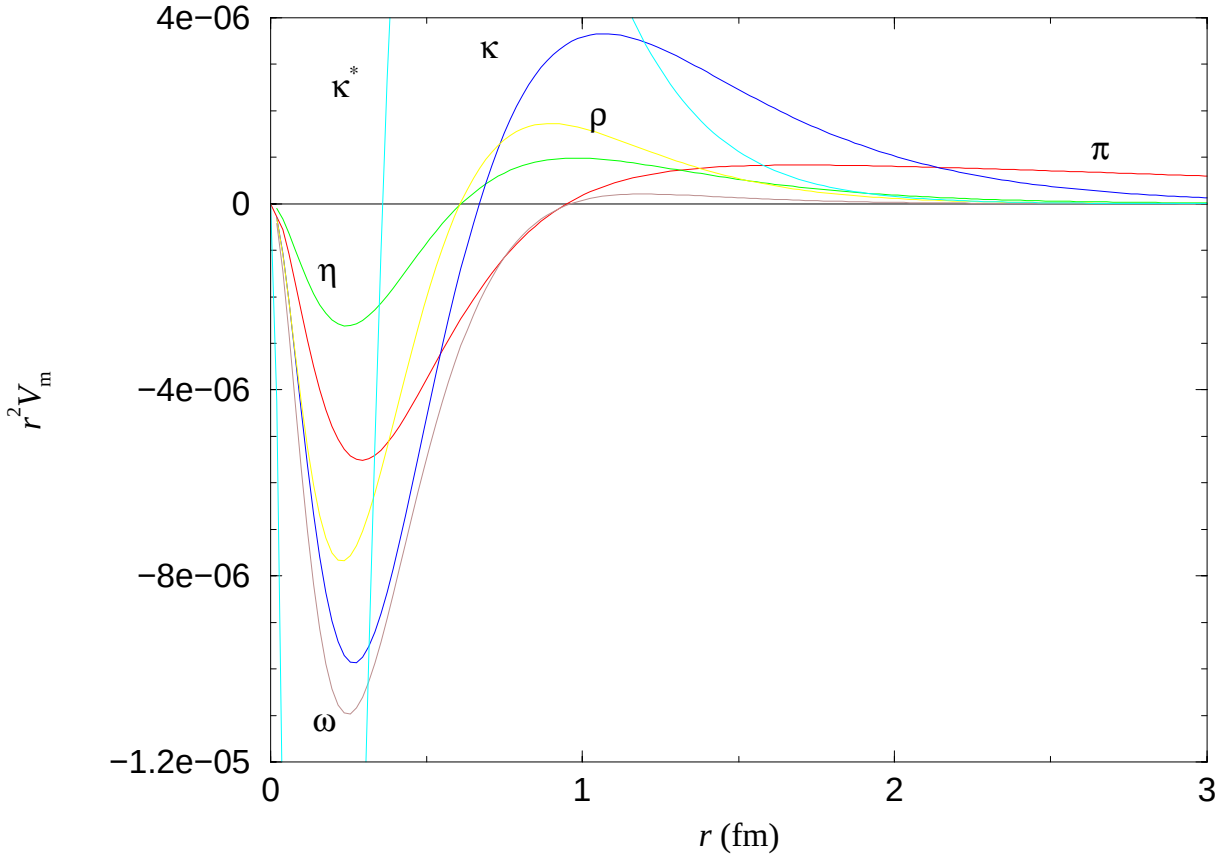

Figure 5.9: Weak Potential for all mesons in Central Channel. Weak potential for each meson in the central ${}^1S_0 \to {}^1S_0$ channel. Double monopole form factor included.

Mesons	SRC	Γ_0	Γ_1	Γ_n/Γ_p
π	None	2.75	0.24	0.16
π	f_{SC}	2.39	0.18	0.14
π	tensor	2.87	0.17	0.11
π	sigma	6.36	0.15	0.05
ALL	None	2.91	0.52	0.30
ALL	f_{SC}	2.26	0.42	0.31
ALL	tensor	2.90	0.38	0.23
ALL	sigma	5.20	0.49	0.17

Table 5.5: Partial decay widths in units of Γ_{free} for the case of the full complement of mesons compared with the pion alone. Note that for the last line, only the pion and strange mesons have ΣN decay components included. A double monopole FF is used in all cases together with various choices for the initial state correlations. No final state correlations are included.

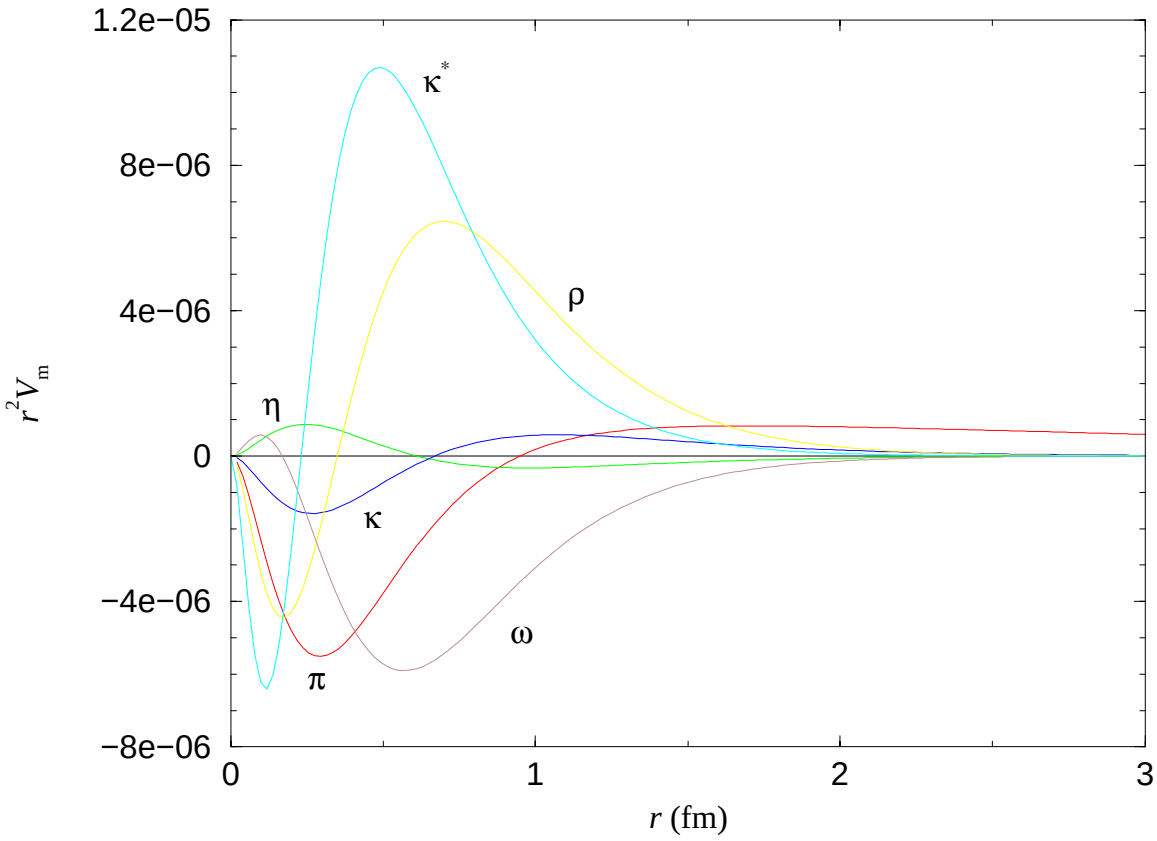

Figure 5.10: Weak Potential for all mesons in Central Channel. Weak potential for each meson in the central ${}^3S_1 \rightarrow {}^3S_1$ channel. Double monopole form factor included.

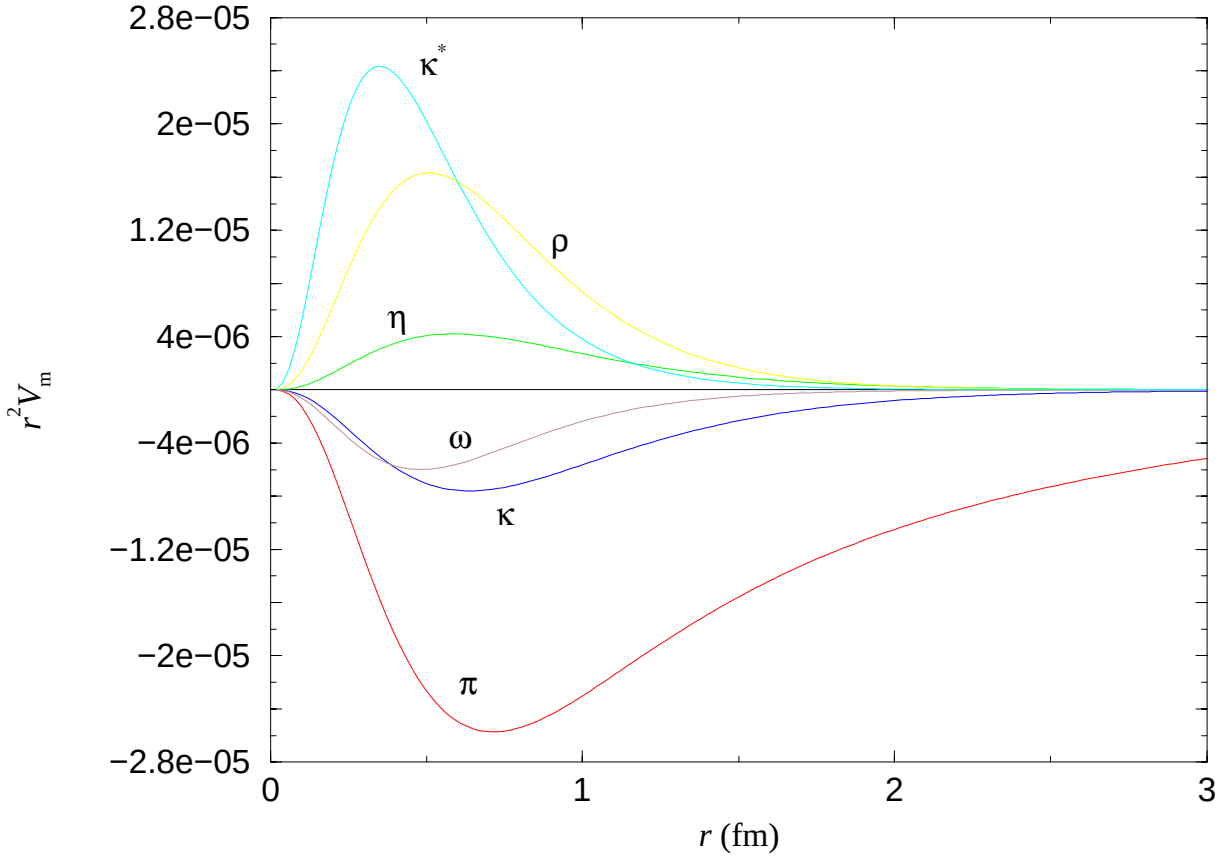

Figure 5.11: Weak Potential for all mesons in Tensor Channel. Weak potential for each meson in the tensor ${}^3S_1 \to {}^3D_1$ channel. Double monopole form factor included.

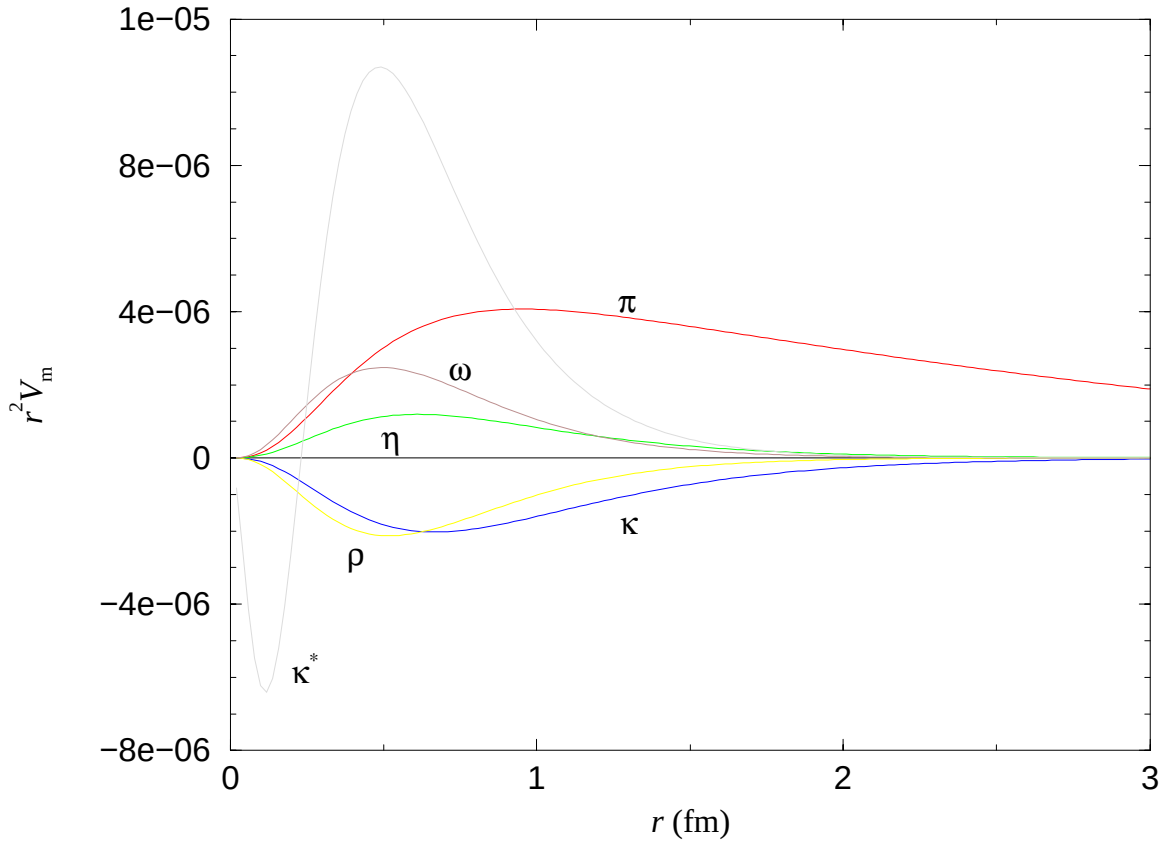

Figure 5.12: Weak Potential for all mesons in Parity-Violating Channel. Weak potential for each meson in the parity-violating ${}^1S_0 \to {}^3P_0$ channel. Double monopole form factor included.

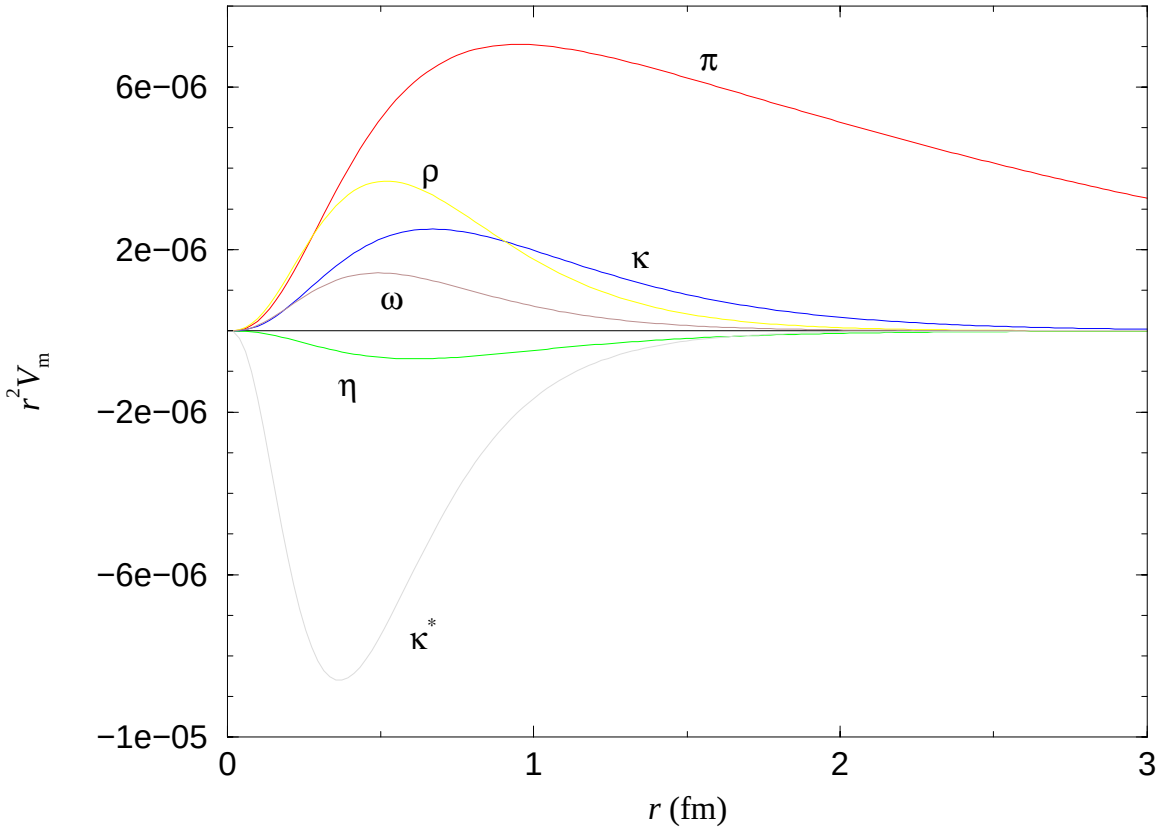

Figure 5.13: Weak Potential for all mesons in Parity-Violating Channel. Weak potential for each meson in the parity-violating ${}^3S_1 \to {}^1P_1$ channel. Double monopole form factor included.

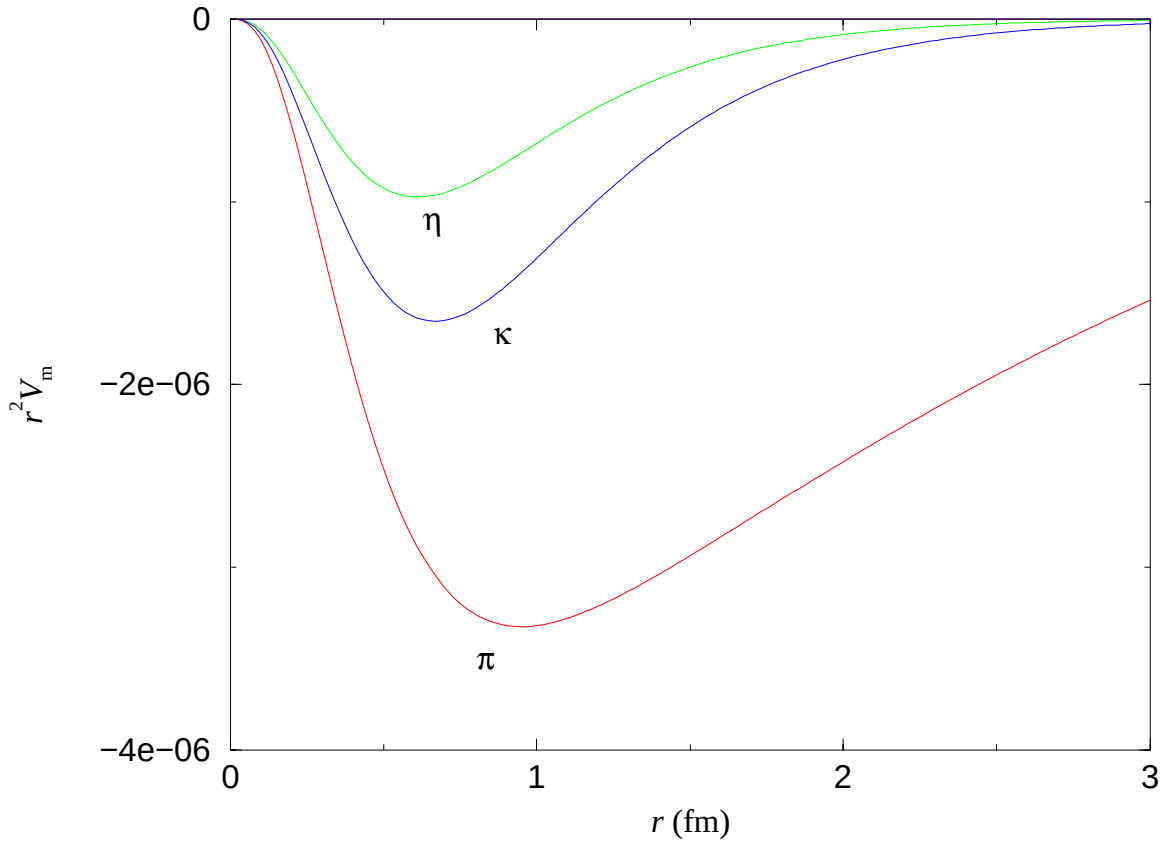

Figure 5.14: Weak Potential for all mesons in Parity-Violating Channel. Weak potential for each meson in the parity-violating ${}^3S_1 \rightarrow {}^3P_1$ channel. Only pseudoscalar mesons have non-zero potentials in this channel. Double monopole form factor included.

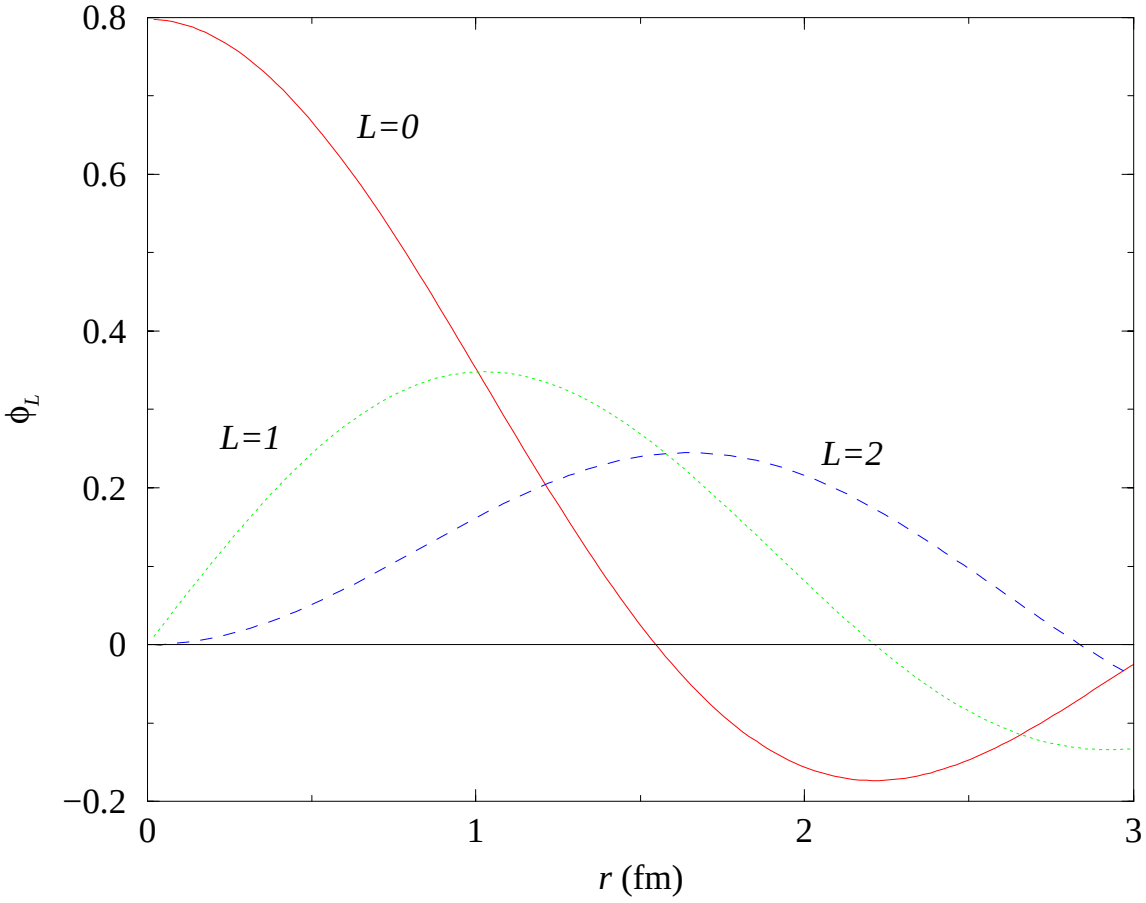

Figure 5.15: Final state NN wavefunctions for different channels. No final state correlations are included, so each is simply a normalized bessel function. The relative momentum for the NN state is $q_N = 400$ MeV/c.

as ${}^{12}_{\Lambda}C$ [51], and indirectly for heavier systems using a Local Density Approximation (LDA) [52]. Collisions of protons on heavy nuclei (Au, Bi, U) have been conducted recently and yield a measure of the lifetime of heavy Λ-hypernuclei [53]. This leads to a decay width of $\Gamma = 1.8$ for heavy hypernuclei. This compares with a value of close to 1 for a lighter hypernucleus such as ${}^{12}_{\Lambda}C$. Presumably, the total decay width measured for heavy hypernuclei should be directly comparable to a NM calculation. One caveat could be the fact that actual heavy hypernuclei have a N/Z ratio significantly larger than unity [54]. This of course depends on the Γ_n/Γ_p ratio. Another connection between the realms of high and low A hypernuclei can be forged with the aid of the LDA. This tool provides a rough but direct connection between results calculated for NM and relatively low mass hypernuclei which are more accessible both experimentally and for direct theoretical analysis. The total decay width for a system with an average density corresponding to ${}^{208}_{\Lambda}Pb$ is $\Gamma_{tot} = 1.59$ and for a system with a density profile approximating that of ${}^{12}_{\Lambda}C$, the width is $\Gamma_{tot} = 1.29$. These two methods give a decrease in total width of something in the neighborhood of 20-45% when one compares a heavy system with a light one. This connection allows finally a comparison between the nuclear matter results of this work and calculations performed directly for lighter finite nuclei such as ${}^{12}_{\Lambda}C$. A further caution concerning the comparison of nuclear matter results with those of a finite nucleus: the initial state wavefunction. The relative wavefunction between the interacting ΛN pair is different in nuclear matter compared with a finite system. In particular, the average lambda momentum is not zero as assumed in the nuclear matter calculations. Perhaps this increase in the average Λ momentum is washed out by the fermi distribution of momentum of the nucleons which stimulate the non-mesonic decay. Any trend could be simply investigated by varying the momentum of the decaying Λ-hyperon, though that has not been done in this work.

5.3.7 Γ_n/Γ_p: Experiment vs Theory

One of the primary observables associated with non-mesonic lambda decay is the ratio of the neutron induced partial width, $\Gamma_{\Lambda n \to nn}$, to the proton induced partial width, $\Gamma_{\Lambda p \to np}$. There is a longstanding discrepancy between theory and experiment concerning this ratio. Experimentally this value has been close to unity with large error bars which have recently narrowed in a new analysis [55]. Theoretically the

ratio has been significantly lower, a value of 0.1 typical for calculations dominated by pion exchange. The strong tensor force of the pion inevitably leads to a dominance of the $T = 0$ final states and a subsequently low Γ_n/Γ_p ratio. Invoking the $\Sigma N \to NN$ decay channel can not resolve the discrepancy with experiment because this decay is also dominated by the tensor interaction, resulting in a further boost to Γ_p. Likewise, uncertainty in the $\Lambda - \Sigma$ coupling strength cannot hope to improve agreement with experiment if decay is mediated by pions.

The literature contains a number of approaches to this problem. If the $\Delta I = 1/2$ rule is violated, then it may be possible to lessen the dominance of the pion's tensor channel [56]. Direct quark models which circumvent the $\Delta I = 1/2$ rule have also been proposed [57]. In addition to purely theoretical efforts, the models and assumptions used in the experimental analyses have been examined. Final state interactions affect the nucleon energy distribution, and charge exchange can shift the ratio of neutrons to protons found in the final state. Uncertainty concerning the impact of these processes casts a fuzzy shadow over the quoted experimental values for Γ_n/Γ_p. It is partly due to the employment of a monte carlo model [58] to account for FSI that error bars on this important observable have decreased recently [55]. Still, experiments new and old favor a value of $\Gamma_n/\Gamma_p \geq 1$ and discount a pion dominated decay.

It is natural to look to mesons other than the pion for contributions to the non-mesonic decay which might preferentially populate $T = 1$ final states. In particular, a meson lacking a strong tensor component would be a candidate for consideration. As an example, a simple examination of the kaon coupling constants leads to an expected ratio of $\Gamma_1/\Gamma_0 \approx 40$ considering only the two central channels. Using Eq. (4.71), this leads to a Γ_n/Γ_p ratio near the maximum possible value of 2. However, this estimate implicitly assumes that the central channels dominate the kaon mediated decay, which turns out not to be the case. Even before correlations are considered, the decay amplitude for the kaon tensor channel turns out to be comparable to the $T = 1$ central channel. Taking all channels together, including the non-negligible PV decay channels, the Γ_1/Γ_0 ratio is sharply reduced to a value of 1.27, yielding $\Gamma_n/\Gamma_p = 1.12$. Initial-state correlations lower this value to 0.81 for diagonal correlations and further to 0.65 at the level of sigma correlations. Though marginally lower than the experimental value, this shows that a meson with a different potential structure from the pion can positively affect the decay observables.

Theory/Expt.	Note	Γ_n/Γ_p	Source
theory	π	0.093	[51]
theory	$\pi + \kappa$	0.210	[51]
theory	all	0.181	[51]
expt.	1N and 2N	$0.96^{+0.10+0.22}_{-0.09-0.21}$	[55]
expt.	1N	$1.17^{+0.09+0.20}_{-0.08-0.18}$	[55]
expt.		$1.87 \pm 0.59^{+0.32}_{-1.00}$	[59]
expt.		$1.33^{+1.12}_{-0.81}$	[60]

Table 5.6: Γ_n/Γ_p for the ${}^{12}_{\Lambda}C$ hypernucleus. The 1N and 2N result assumes a value of $\Gamma_2/\Gamma_{nm} = 0.32$.

Finally, it is worth pointing out that while the most recent experimental values for the Γ_n/Γ_p ratio are more precise than in the past, they are also very model dependent. In particular, it is not clear how to reinterpret these results in light of a significant contribution from sigma decays.

Chapter 6

Conclusions

The spectral function for a Λ-hyperon is calculated for the first time in this work. The structure is very similar to what is found for a nucleon; a comparison which should be made more fully. The chief difference is the coupled channel element which gives rise to threshold effects in the lambda self-energy and spectral function. This behavior could be understood more fully by forging an analytic connection to established results for coupled channels in scattering theory. The details of the spectral distribution of a lambda can also have modest consequences for hypernuclear production probabilities and the mesonic decay width in a nuclear medium. The mesonic width, while Pauli suppressed in a nuclear environment despite strong correlations, may well show sensitivity to details of the lambda strength distribution.

For this work, only the nucleon energy spectrum is utilized. A more sophisticated calculation would include a detailed nucleon spectral function folded into the calculation of the lambda self-energy. A fully self-consistent calculation would be a logical, though considerably larger, step forward in terms of calculational complexity. In general, the more important correlations become for a system, and the farther afield from an independent particle description one ventures, the more necessary it becomes to embrace correlations in a fully self-consistent manner. It is not clear that the hypernucleus warrants this type of consideration.

Though nuclear matter calculations offer many technical advantages, in the end it is beneficial to make as close a comparison to experiment as possible. To this end, calculations for a finite system would be a logical next step. In the interest of a well-understood comparison to experiment, a reanalysis of ${}^{12}_{\Lambda}C$ decay taking into account decay from ΣN states would be welcome.

Finally, as has been noted, relatively new baryon-baryon potentials are available which explore the freedom one currently has in defining the Λ-Σ coupling. Inserting these new potentials into the present calculational framework would be a simple way to translate this freedom in the YN potentials to variability in the lambda decay observables.

Appendix A

Calculation of the G-matrix

A.1 Calculational Details

As mentioned previously, the natural sp basis for an infinite system consists of eigenstates of momentum, spin and iso-spin (Eq. 2.12),

$$|\alpha\rangle \equiv |\vec{k}\, sm_s\, tm_t; B\rangle, \tag{A.1}$$

where B denotes the species of baryon. The question of how to combine the individual Λ and N sp bases to form the ΛN two-particel basis is answered by considering the symmetries of the two-body interaction. The NSC89 interaction conserves total momentum,

$$\vec{Q} \equiv \vec{k}_\Lambda + \vec{k}_N, \tag{A.2}$$

total spin,

$$S \equiv s_\Lambda + s_N, \tag{A.3}$$

total iso-spin,

$$T \equiv t_\Lambda + t_N, \tag{A.4}$$

and total angular momentum,

$$J \equiv L_{rel} + S, \tag{A.5}$$

where L_{rel} refers to the relative orbital angular momentum of the two particles. These properties are used to reduce the dimensionality of the G-matrix integral equation prior to its numerical solution.

In terms of the product states,

$$|\vec{k}_Y \vec{k}_N\rangle \equiv |\vec{k}_Y\rangle \otimes |\vec{k}_N\rangle, \tag{A.6}$$

the diagrammatic G-matrix equation may be translated to

$$\begin{aligned}\langle \vec{k}_3\vec{k}_4; Y_3N_4|G(\Omega)|\vec{k}_1\vec{k}_2; Y_1N_2\rangle &= \langle \vec{k}_3\vec{k}_4; Y_3N_4|V|\vec{k}_1\vec{k}_2; Y_1N_2\rangle \\ &- \sum_{Y_5}\int\frac{d\omega_5}{2\pi i}\int\frac{d^3k_5}{(2\pi)^3}\int\frac{d^3k_6}{(2\pi)^3}\langle \vec{k}_3\vec{k}_4; Y_3N_4|V|\vec{k}_5\vec{k}_6; Y_5N_6\rangle g^0_{Y_5}(\vec{k}_5;\omega_5)g^0_{N_6}(\vec{k}_6;\Omega-\omega_5) \\ &\langle \vec{k}_5\vec{k}_6; Y_5N_6|G(\Omega)|\vec{k}_1\vec{k}_2; Y_1N_2\rangle.\end{aligned} \tag{A.7}$$

The conserved total energy, $\Omega \equiv \omega_1 + \omega_2$, has been introduced in Eq. A.7, and spin and isospin labels have been suppressed for clarity.

This equation may be formally simplified by introducing the reduced two-particle propagator for the intermediate YN state:

$$g^{II}_{Y_5N_6}(\vec{k}_5, \vec{k}_6; \Omega) \equiv -\int\frac{d\omega_5}{2\pi i}g^0_{Y_5}(\vec{k}_5;\omega_5)g^0_{N_6}(\vec{k}_6;\Omega-\omega_5). \tag{A.8}$$

Conservation of total momentum suggests a change of variables to total momentum,

$$\vec{Q} \equiv \vec{k}_1 + \vec{k}_2 = \vec{k}_3 + \vec{k}_4 = \vec{k}_5 + \vec{k}_6, \tag{A.9}$$

and relative momentum,

$$\vec{q}_i \equiv (\frac{\mu_Y}{m_N})\vec{k}_4 - (\frac{\mu_Y}{m_Y})\vec{k}_3 \tag{A.10}$$

$$\vec{q}_f \equiv (\frac{\mu_Y}{m_N})\vec{k}_2 - (\frac{\mu_Y}{m_Y})\vec{k}_1 \tag{A.11}$$

$$\vec{q}' \equiv (\frac{\mu_Y}{m_N})\vec{k}_6 - (\frac{\mu_Y}{m_Y})\vec{k}_5. \tag{A.12}$$

The reduced mass for the YN system has been introduced as

$$\mu_Y \equiv \frac{m_Y m_N}{m_Y + m_N}. \tag{A.13}$$

The single particle momenta may be expressed in terms of the new variables as

$$\vec{k}_1 = \vec{Q}_Y - \vec{q}_i \tag{A.14}$$

$$\vec{k}_2 = \vec{Q}_N + \vec{q}_i \tag{A.15}$$

$$\vdots \tag{A.16}$$

using the notation,

$$\vec{Q}_Y \equiv (\frac{\mu_Y}{m_N})\vec{Q} \tag{A.17}$$

$$\vec{Q}_N \equiv (\frac{\mu_Y}{m_Y})\vec{Q}. \tag{A.18}$$

In the new basis, the simplification of total momentum conservation,

$$\langle \vec{k}_f \vec{Q}_f; Y_3 N_4 | V | \vec{k}_i \vec{Q}_i; Y_1 N_2 \rangle = (2\pi)^3 \delta(\vec{Q}_f - \vec{Q}_i) \langle \vec{k}_f; Y_3 N_4 | V | \vec{k}_i; Y_1 N_2 \rangle, \tag{A.19}$$

serves to reduce the dimensionality of the G-matrix integral equation by half, leaving

$$\begin{aligned} \langle \vec{k}_f; Y_3 N_4 | G(\vec{Q};\Omega) | \vec{k}_i; Y_1 N_2 \rangle &= \langle \vec{k}_f; Y_3 N_4 | V | \vec{k}_i; Y_1 N_2 \rangle \\ &+ \sum_{Y_5} \int \frac{d^3 q'}{(2\pi)^3} \langle \vec{k}_f; Y_3 N_4 | V | \vec{q}'; Y_5 N_6 \rangle g^{II}_{Y_5 N_6}(\vec{q}', \vec{Q}; \Omega) \\ &\langle \vec{q}'; Y_5 N_6 | G(\vec{Q};\Omega) | \vec{k}_i; Y_1 N_2 \rangle. \end{aligned} \tag{A.20}$$

The next step is to perform a partial-wave decomposition of the relative momentum states,

$$|\vec{q}\rangle \rightarrow |q\, L\, M_L\rangle. \tag{A.21}$$

The G-matrix defined by Eq. A.20 can now be expressed in terms of a sum over matrix elements for each coupled partial-wave channel,

$$\langle \vec{k}_f | G(\vec{Q};\Omega) | \vec{k}_i \rangle = (2\pi)^3 \sum_{L M_L L' M'_L} \langle k_f L M_L | G(\vec{Q};\Omega) | k_i L' M'_L \rangle Y_{L M_L}(\hat{k_f}) Y^*_{L' M'_L}(\hat{k}_i). \tag{A.22}$$

Each term of Eq. A.22 has a simple angular dependence, ie. it is proportional to a product of spherical harmonics. Substitution of the Eq. A.22 expansion into Eq. A.20 permits the angular integration over $\hat{q}'$ to be performed explicitly using the orthogonality of the spherical harmonics. This works provided there is no angular dependence in $g^{II}_{YN}(\vec{q}', \vec{Q}; \Omega)$. In general this provision will not be met, so the two-particle propagator is angle-averaged.

In order to examine the $\hat{q}'$-dependence of the two-particle propagator, an explicit form is first obtained by inserting the following expressions for the non-interacting propagators,

$$g_Y^0(k_Y;\omega) = \frac{1}{\omega - \varepsilon_Y(k_Y) + i\eta} \tag{A.23}$$

$$g_N^0(k_N;\omega) = \frac{\theta(k_N - k_F)}{\omega - \varepsilon_N(k_N) + i\eta}, \tag{A.24}$$

into Eq. A.8. Performing the integration over energy leaves the simple expression:

$$g_{YN}^{II}(k_Y, k_N;\Omega) = \frac{\theta(k_N - k_F)}{\Omega - \varepsilon_Y(k_Y) - \varepsilon_N(k_N) + i\eta}. \tag{A.25}$$

The straight-forward approach to angle-averaging leads to

$$\bar{g}_{YN}^{II}(q', Q;\Omega) \equiv \frac{1}{4\pi}\int d\Omega_{\hat{q}'}\, g_{YN}^{II}(\vec{q}', \vec{Q};\Omega), \tag{A.26}$$

for the angle-averaged two-particle propagator. This definition suffers from two problems. First, the integral in Eq. A.26 can not in general be performed analytically. More of a problem, however, is the fact that Eq. A.26 no longer shares the simple analytic structure of the original two-particle propagator, Eq. A.25. The prescription of Eq. A.26 "smears" the simple pole, which creates problems later in the calculation of the G-matrix. For this reason, angle-averaging is implemented in a different way. Instead of averaging the entire two-particle propagator at once, the numerator and denominator of Eq. A.25 are angle-averaged separately. This leads to the new definition

$$\bar{g}_{YN}^{II}(q', Q;\Omega) \equiv \frac{\bar{\theta}(q', Q; k_F)}{\Omega - \bar{\varepsilon}_{YN}(q', Q; k_F) + i\eta}. \tag{A.27}$$

which makes use of a shorthand notation for the two-particle energy,

$$\varepsilon_{YN}(\vec{q}', \vec{Q}) = \varepsilon_Y(\vec{q}', \vec{Q}) + \varepsilon_N(\vec{q}', \vec{Q}). \tag{A.28}$$

An additional simplification of

$$\bar{\varepsilon}_B(k_B) \equiv \varepsilon_B(\bar{k}_B), \tag{A.29}$$

is made, where the sp momentum is angle-averaged instead of the energy. The sp momenta k_Y and k_N are functions of q' and Q through Eq. A.16,

$$k_B = k_B(q', Q; k_F). \tag{A.30}$$

The dependence on k_F arises because the Pauli restriction on allowed angles is taken into account even though the two parts of the two-particle propagator are angle-averaged separately [61].

Each matrix element in the partial-wave basis may now be calculated via a more tractable one-dimensional integral equation,

$$\begin{aligned}\langle k_f L_f M_{L_f}; Y_3 N_4 | G(\vec{Q};\Omega) | k_i L_i M_{L_i}; Y_1 N_2 \rangle &= \langle k_f L_f M_{L_f}; Y_3 N_4 | V | k_i L_i M_{L_i}; Y_1 N_2 \rangle \\ &+ \sum_{Y'} \sum_{L' M'_L} \int dq'\, q'^2 \langle k_f L_f M_{L_f}; Y_3 N_4 | V | q' L' M'_L; Y_5 N_6 \rangle \bar{g}^{II}_{Y'N}(q', Q; \Omega) \\ &\langle q' L' M'_L; Y_5 N_6 | G(\vec{Q};\Omega) | k_i L_i M_{L_i}; Y_1 N_2 \rangle. \end{aligned} \tag{A.31}$$

Aside from the necessity of angle-averaging the two-particle propagator, the price which must be paid for this simplification is the infinite number of partial-wave matrix elements required for the sum in Eq. A.22. In practice, only a few terms in the the partial-wave expansion make up the bulk of the contribution and the sum may be truncated to good approximation.

A.1.1 Coupling to total angular momentum

The NSC89 interaction possesses a strong tensor force which can couple states of different orbital angular momentum, L. The tensor force is primarily the result of pion exchange and is strongest for the $\Lambda N - \Sigma N$ channel. Pion exchange is nominally forbidden for the $\Lambda N - \Lambda N$ channel because iso-spin cannot be conserved at the $\Lambda\Lambda\pi$ vertex for a Λ with zero isospin. Charge-symmetry breaking voids this restriction to some extent, but the tensor force in this channel remains relatively weak. The strong interaction does not violate parity, so the total spin, S, of the YN state is still a good quantum number and L can only change by 0 or 2 units. Under these conditions, it is natural to make another basis change; this time to eigenstates of total angular

momentum, $J = L + S$. In the new basis, the G-matrix is given by

$$\begin{aligned}
&\langle k_f J(L_f ST); Y_3 N_4 | G(\vec{Q};\Omega) | k_i J(L_i ST); Y_1 N_2 \rangle \\
&\quad = \langle k_f J(L_f ST); Y_3 N_4 | V | k_i J(L_i ST); Y_1 N_2 \rangle \\
&\quad + \sum_{Y_5} \sum_{L'} \int dq' \, q'^2 \langle k_f J(L_f ST); Y_3 N_4 | V | q J(L' ST); Y_5 N_6 \rangle \bar{g}^{II}_{Y' N}(q, Q; \Omega) \\
&\qquad \langle q J(L' ST); Y_5 N_6 | G(\vec{Q};\Omega) | k_i J(L_i ST); Y_1 N_2 \rangle, \qquad \text{(A.32)}
\end{aligned}$$

where a label for the total iso-spin, T, has been included for completeness. The operators which define the potential matrix elements are all scalars in J and T. This means that the matrix elements defined by Eq. A.32 are independent of M_J and M_T.

The integral equation for the G-matrix is now in its final incarnation, even though Eq. A.32 does not represent a closed form solution. A standard method for solving such a one-dimensional integral equation is to discretize the integral and invert the resulting matrix equation [50]. The discrete momentum mesh must be chosen with some care, taking into consideration the q'-dependence of both the potential matrix elements and the angle-averaged two-particle propagator.

The potential matrix elements are quite smooth functions of the relative momentum in all important partial wave channels. The strong short-range part of the YN interaction couples low momentum states to intermediate states with very high momentum. As a result, it is necessary to choose a q'-mesh which adequately covers the high q' region.

The q'-dependence of the two-particle propagator arises from two sources. The Pauli θ-function in the numerator serves mainly to cut off q' below a minimum, ${q'}_{min}(Q)$, defined by

$${q'}_{min}(Q) \equiv \begin{cases} k_F - Q_N & Q_N < k_F \\ 0 & otherwise. \end{cases} \qquad \text{(A.33)}$$

For Ω above a certain threshold, $\Omega_{min}(Q)$, there will be a pole in the angle-averaged two-particle propagator (Eq. A.27). This pole occurs for a value, q'_0, of the relative momentum defined by

$$\Omega = \bar{\varepsilon}_{YN}(q'_0, Q; k_F). \qquad \text{(A.34)}$$

The pole location, q'_0, as well as the cutoff value, q'_{min}, are different for the two YN channels. This means that separate q'-meshes must be constructed for each channel.

A.1.2 Λ Self-energy

For either of the $L = 0$ partial-wave channels, the self-energy is given in terms of the G-matrix and the nucleon-hole spectral function as

$$\Sigma_\Lambda(k_\Lambda;\omega) = \sum_J (2J+1) \int dQ\, Q^2 \int \frac{d\xi_Q}{2} \int d\omega' \tag{A.35}$$

$$\times \langle qJ(LS)T;\Lambda N|G(Q;\omega+\omega')|qJ(LS)T;\Lambda N\rangle S_N^h(k_N;\omega'). \tag{A.36}$$

The relative momentum, q, and the nucleon momentum, k_N, are functions of the Λ momentum, k_Λ, and the integration variables,

$$q = q(k_\Lambda, Q, \xi) = ({Q_\Lambda}^2 + {k_\Lambda}^2 - 2Q_\Lambda k_\Lambda)^{1/2} \tag{A.37}$$

$$k_N = k_N(k_\Lambda, Q, \xi) = (Q^2 + {k_\Lambda}^2 - 2Qk_\Lambda)^{1/2}. \tag{A.38}$$

For the case of mean-field nucleons,

$$S_N^h(k_N;\omega') = \delta(\omega' - \varepsilon_N(k_N)), \tag{A.39}$$

and the self-energy becomes

$$\Sigma_\Lambda(k_\Lambda;\omega) = \sum_J (2J+1) \int dQ\, Q^2 \int \frac{d\xi_Q}{2}$$

$$\times \langle qJ(LS)T;\Lambda N|G(Q;\omega+\varepsilon_N(k_N))|qJ(LS)T;\Lambda N\rangle. \tag{A.40}$$

The self-energy is solved for numerically by discretizing the integrals in Eq. A.40.

Appendix B

Breakdown of the Quasi-particle Approximation

In this appendix, a quantitative measure of the validity of the QPA is presented. The self-energy is expanded about the qp-energy as in Eq. 2.59 but now terms up to order $(\omega - \varepsilon_{qp})^2$ are included for the imaginary part as well as the real part:

$$\begin{aligned} \text{Re } \Sigma(k;\omega) &\simeq \text{Re } \Sigma(k;\varepsilon_{qp}(k)) + \frac{\partial \text{Re } \Sigma(k;\varepsilon_{qp}(k))}{\partial\omega}(\omega - \varepsilon_{qp}(k)), \\ &\equiv R + R'(\omega - \varepsilon_{qp}), \qquad \text{(B.1)} \\ \text{Im } \Sigma(k;\omega) &\simeq \text{Im } \Sigma(k;\varepsilon_{qp}(k)) + \frac{\partial \text{Im } \Sigma(k;\varepsilon_{qp}(k))}{\partial\omega}(\omega - \varepsilon_{qp}(k)), \\ &\equiv I + I'(\omega - \varepsilon_{qp}). \qquad \text{(B.2)} \end{aligned}$$

In this "extended" QPA the spectral function takes the form

$$S_{qpx}(\omega) = \frac{-1}{\pi}\frac{z^2[I + I'(\omega - \varepsilon_{qpx})]}{(\omega - \varepsilon_{qpx})^2 + (zI)^2}, \qquad \text{(B.3)}$$

where terms proportional to I'^2 and R'^2 have been neglected. This function peaks at a slightly different energy,

$$\varepsilon_{qpx} \equiv \varepsilon_{qp} - zII', \qquad \text{(B.4)}$$

than the usual qp-approximation, but it is the new energy dependent term in the numerator which spoils the simple lorentzian shape and causes the qp-approximation to eventually breakdown. This breakdown occurs when one moves far enough from

the peak such that

$$|I| \sim |I'(\omega - \varepsilon_{qpx})|. \tag{B.5}$$

This occurs at an energy, $\omega \simeq \varepsilon_{qpx} \pm \delta$, where

$$\delta \equiv |I/I'|. \tag{B.6}$$

It is reasonable to say that the simple QPA ($I' = 0$) is valid at the x-percent level if a fraction, x, of the qp-strength is located within δ of ε_{qpx}.

In the energy range about ε_{qp} where the QPA is valid, the spectral function has a lorentzian shape. For this form of the spectral function, it can be shown that a fraction, x, of the qp-strength is located within a range,

$$\delta \equiv |zI \tan(x\pi/2)|, \tag{B.7}$$

of ε_{qp}. In other words,

$$\int_{\varepsilon_{qp}-\delta}^{\varepsilon_{qp}+\delta} \partial\omega S_{qp}(k;\omega) = xz(k). \tag{B.8}$$

Combining the conditions specified in Eq. B.6 and Eq. B.7 yields

$$|I/I'| = |zI \tan(x\pi/2)| \tag{B.9}$$

and finally

$$x = \frac{2}{\pi} \tan^{-1}(1/zI') \tag{B.10}$$

for the fraction of qp-strength accurately described within the QPA. Note that this result is independent of the width, I, of the qp-peak.

The k-dependent parameters, z and I', determine x and hence the validity of the QPA as a function of momentum. In the limit $k \to 0$, $I' \to 0$ and so $x \to 1$. This is just another confirmation that the QPA becomes exact for $k \to k_F$. The breakdown in the QPA as k increases is documented graphically in Fig. B.1.

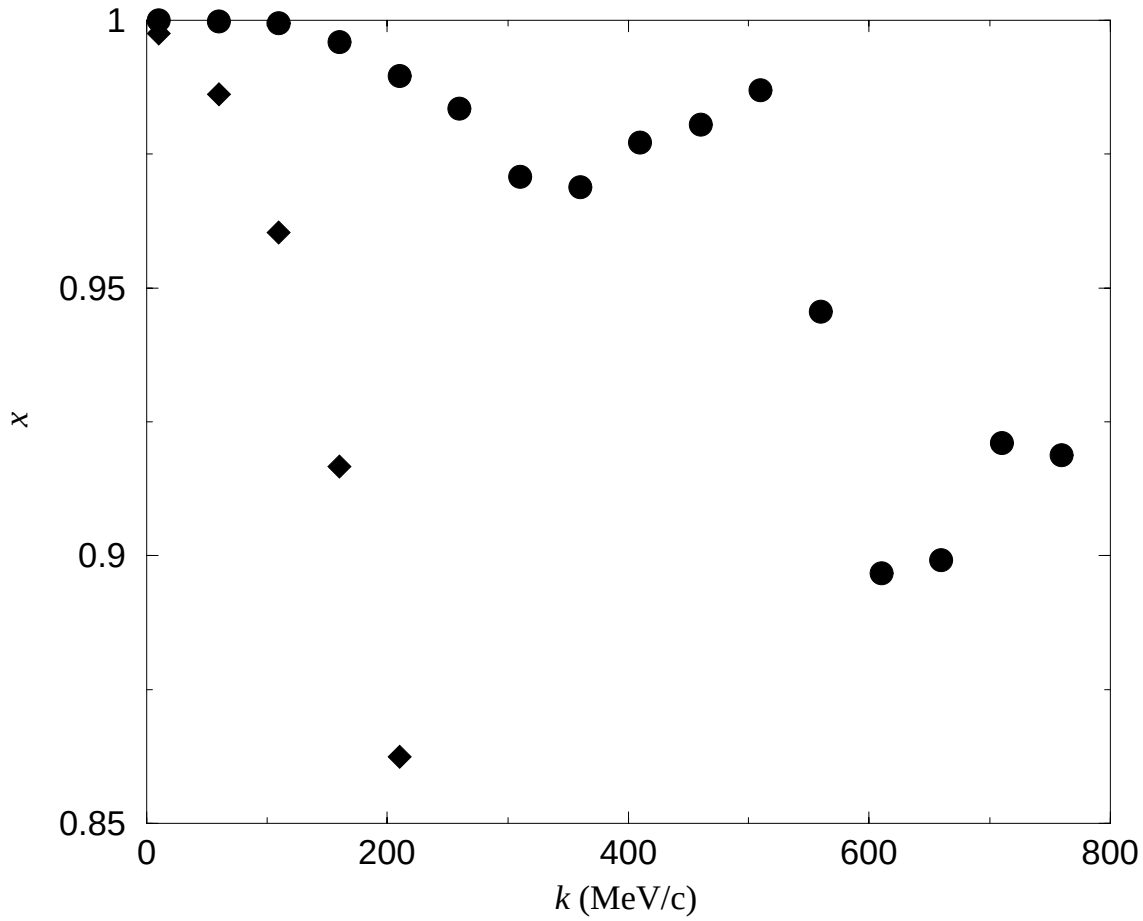

Figure B.1: Fraction of qp-strength accurately described within the QPA for the lambda (circles) and nucleons [32] (diamonds).

Appendix C

Isospin Structure of Spurions

In this appendix, details of the sigma spurion formalism are presented in Section C.1, followed by a detailed manipulation of the reduced decay amplitudes for the lambda and sigma hyperons in Sections C.2 and C.3 respectively.

C.1 Sigma Spurion

Similar to Eq. (4.37), the isospin structure of the sigma spurion states is

$$\begin{aligned} |\tilde{\Sigma}\rangle &\equiv |\tfrac{1}{2}\,-\tfrac{1}{2}\rangle \otimes [\gamma_{m_\Sigma}|1\,m_\Sigma\rangle], \\ &= \gamma_{m_\Sigma}[|\tfrac{1}{2}\,m_\Sigma-\tfrac{1}{2}\rangle\langle\tfrac{1}{2}\,m_\Sigma-\tfrac{1}{2}|\tfrac{1}{2}\,-\tfrac{1}{2};1\,m_\Sigma\rangle \\ &+ |\tfrac{3}{2}\,m_\Sigma-\tfrac{1}{2}\rangle\langle\tfrac{3}{2}\,m_\Sigma-\tfrac{1}{2}|\tfrac{1}{2}\,-\tfrac{1}{2};1\,m_\Sigma\rangle]. \end{aligned} \tag{C.1}$$

The factor,

$$\gamma_m = \begin{cases} -1 & m = 1 \\ 1 & \text{otherwise,} \end{cases} \tag{C.2}$$

is included with the sigma states to ensure that Σ^+ and Σ^- are antiparticles. Evaluating the Clebsch-Gordon coefficients explicitly, this works out to

$$|\tilde{\Sigma}^+\rangle = \sqrt{\frac{2}{3}}|\tfrac{1}{2}\,\tfrac{1}{2}\rangle - \frac{1}{\sqrt{3}}|\tfrac{3}{2}\,\tfrac{1}{2}\rangle, \tag{C.3}$$

$$|\tilde{\Sigma}^0\rangle = -\frac{1}{\sqrt{3}}|\tfrac{1}{2}\,-\tfrac{1}{2}\rangle + \sqrt{\frac{2}{3}}|\tfrac{3}{2}\,-\tfrac{1}{2}\rangle, \tag{C.4}$$

$$|\tilde{\Sigma}^-\rangle = |\tfrac{3}{2}\,-\tfrac{3}{2}\rangle \tag{C.5}$$

for the various charge states.

C.2 Reduced Amplitudes: Lambda

Amplitudes for the two lambda decay channels may be expressed in terms of a "reduced" amplitude,

$$a(\Lambda \to N\pi) \equiv \langle \tilde{\Lambda} | \vec{\tau} \cdot \vec{\phi} | N\pi \rangle \tilde{a}(\Lambda \to N\pi), \tag{C.6}$$

which excludes the isospin dependence. In order to easily evaluate the isospin dependent factor in Eq. 4.41, it is convenient to write the scalar product,

$$\vec{\tau} \cdot \vec{\phi} = -\tau_1 \phi_{-1} - \tau_{-1} \phi_1 + \tau_0 \phi_0, \tag{C.7}$$

in terms of pion creation/annihilation operators,

$$\phi_{-1} = \phi_- \qquad \phi_1 = -\phi_+ \qquad \phi_0 = \phi_0, \tag{C.8}$$

$$\phi_-|\pi^+\rangle = |0\rangle \quad \phi_+|\pi^-\rangle = |0\rangle \quad \phi_0|\pi^0\rangle = |0\rangle, \tag{C.9}$$

and isospin raising/lowering operators,

$$\tau_1 = -\sqrt{2}\tau_+ \quad \tau_+|n\rangle = |p\rangle \quad \tau_+|p\rangle = |0\rangle \tag{C.10}$$

$$\tau_{-1} = \sqrt{2}\tau_- \quad \tau_-|n\rangle = |0\rangle \quad \tau_-|p\rangle = |n\rangle \tag{C.11}$$

$$\tau_0 = \tau_0 \quad \tau_0|n\rangle = -|n\rangle \quad \tau_0|p\rangle = |0\rangle, \tag{C.12}$$

which results in the expression,

$$\vec{\tau} \cdot \vec{\phi} = \sqrt{2}(\tau_+ \phi_- + \tau_- \phi_+) + \tau_0 \phi_0. \tag{C.13}$$

The lambda decay amplitudes in terms of the reduced amplitude are

$$\begin{aligned} a(\Lambda \to p\pi^-) &= \langle \tilde{\Lambda} | \vec{\tau} \cdot \vec{\phi} | p\pi^- \rangle \tilde{a}(\Lambda \to N\pi) \\ &= \langle \tilde{\Lambda} | \sqrt{2}\tau_- \phi_+ | p\pi^- \rangle \tilde{a}(\Lambda \to N\pi) \\ &= \sqrt{2}\langle n | \tau_- | p \rangle \tilde{a}(\Lambda \to N\pi) \\ &= \sqrt{2}\tilde{a}(\Lambda \to N\pi), \end{aligned} \tag{C.14}$$

$$\begin{aligned} a(\Lambda \to n\pi^0) &= \langle \tilde{\Lambda}|\vec{\tau}\cdot\vec{\phi}|n\pi^0\rangle \tilde{a}(\Lambda \to N\pi) \\ &= \langle \tilde{\Lambda}|\tau_0\phi_0|n\pi^0\rangle \tilde{a}(\Lambda \to N\pi) \\ &= \langle n|\tau_0|n\rangle \tilde{a}(\Lambda \to N\pi) \\ &= -\tilde{a}(\Lambda \to N\pi). \end{aligned} \tag{C.15}$$

C.3 Reduced Amplitudes: Sigma

The contribution to the sigma decay amplitudes which correspond to decay from the $T = 1/2$ portion of the spurion state are related to a $T = 1/2$ reduced amplitude in the same way as Eqs. 4.42 and 4.43 for the lambda. The isospin factor for the $T = 3/2$ component of the amplitude may be found by writing the scalar product, $\vec{T}\cdot\vec{\phi}$, in terms of pion creation/annihilation operators,

$$\vec{T}\cdot\vec{\phi} = -T_1\phi_{-1} - T_{-1}\phi_1 + T_0\phi_0, \tag{C.16}$$

as was done in Eq. C.13. Now, using the Wigner-Eckart theorem, the isospin factor appearing in the second term of Eq. 4.44 may be found by evaluating matrix elements of the form

$$\langle \tfrac{3}{2}\, m_{\tilde{\Sigma}}|T_k|\tfrac{1}{2}\, m_N\rangle = \langle \tfrac{1}{2}\, m_N; 1\, m_k|\tfrac{3}{2}\, m_{\tilde{\Sigma}}\rangle \left[\frac{\langle \frac{1}{2}||T||\frac{3}{2}\rangle}{\sqrt{2(\frac{1}{2})+1}}\right]. \tag{C.17}$$

The expression in square brackets is a constant for all $\Sigma \to N\pi$ decays, so any variation due to isospin is accounted for by the Clebsch-Gordon coefficient. Because the term in square brackets is channel independent, it is arbitrary in a sense, and may be conveniently subsumed in the reduced amplitude. This is not necessary of course, but produces the nice result of Eq. 4.50 for the purely $T = 3/2$ decay. As an example, the amplitude for the decay $\Sigma^+ \to p\pi^0$ may be written in terms of the reduced amplitudes as follows:

$$\begin{aligned} a(\Sigma^+ \to p\pi^0) &= \langle \tilde{\Sigma}^+|\vec{\tau}\cdot\vec{\phi}|p\pi^0\rangle \tilde{a}^{(1/2)}(\Sigma \to N\pi) + \langle \tilde{\Sigma}^+|\vec{T}\cdot\vec{\phi}|p\pi^0\rangle \tilde{a}^{(3/2)}(\Sigma \to N\pi) \\ &= \langle \tilde{\Sigma}^+|\tau_0\phi_0|p\pi^0\rangle \tilde{a}^{(1/2)}(\Sigma \to N\pi) \\ &+ \langle \tilde{\Sigma}^+|T_0\phi_0|p\pi^0\rangle \tilde{a}^{(3/2)}(\Sigma \to N\pi) \\ &= \sqrt{\frac{2}{3}}\langle p|\tau_0|p\rangle \tilde{a}^{(1/2)}(\Sigma \to N\pi) \end{aligned}$$

$$
\begin{aligned}
- \quad & \frac{1}{\sqrt{3}}\langle\Delta^+|T_0|p\rangle\tilde{a}^{(3/2)}(\Sigma\to N\pi) \\
= \quad & \sqrt{\frac{2}{3}}\tilde{a}^{(1/2)}(\Sigma\to N\pi) \\
- \quad & \frac{\sqrt{2}}{3}\tilde{a}^{(3/2)}(\Sigma\to N\pi). \qquad \text{(C.18)}
\end{aligned}
$$

The other decay channels may be similarly determined,

$$
\begin{aligned}
a(\Sigma^+\to n\pi^+) &= \frac{2}{\sqrt{3}}\tilde{a}^{(1/2)}(\Sigma\to N\pi) \\
&+ \frac{1}{3}\tilde{a}^{(3/2)}(\Sigma\to N\pi), \qquad \text{(C.19)} \\
a(\Sigma^0\to p\pi^-) &= -\sqrt{\frac{2}{3}}\tilde{a}^{(1/2)}(\Sigma\to N\pi) \\
&+ \frac{\sqrt{2}}{3}\tilde{a}^{(3/2)}(\Sigma\to N\pi), \qquad \text{(C.20)} \\
a(\Sigma^0\to n\pi^0) &= \frac{1}{\sqrt{3}}\tilde{a}^{(1/2)}(\Sigma\to N\pi) \\
&+ \frac{2}{3}\tilde{a}^{(3/2)}(\Sigma\to N\pi), \qquad \text{(C.21)} \\
a(\Sigma^-\to n\pi^-) &= \tilde{a}^{(3/2)}(\Sigma\to N\pi). \qquad \text{(C.22)}
\end{aligned}
$$

Appendix D

Wound Integral

Wound Integrals

The volume integral of the defect wavefunction is a measure of the combined strength and range of the strong interaction and defines a "correlation volume",

$$V_C \equiv \sum_i \int d^3r |\langle \vec{r} | \chi_i \rangle|^2. \tag{D.1}$$

The wound integral, κ, is defined as the ratio of V_C to the volume per particle,

$$V_0 \equiv \frac{1}{\rho} = \frac{3\pi^2}{2{k_F}^3}. \tag{D.2}$$

The concept of the wound integral was introduced by Brandow [62] in the context of the Brueckner-Bethe-Goldstone theory of NM as an expansion parameter for a cluster expansion. It is tempting to argue that correlations are not important if $\kappa \ll 1$, because particles will not, on average, be within interaction range. The wound integral does provide a means of comparing the relative strength of correlations among different potentials. A "partial" κ_{ij} for each channel can be defined by

$$\kappa = \sum_{ij} \kappa_{ij} \tag{D.3}$$

All of the "partial" wound integrals for an initial ΛN S-state are presented in table D.1 along with values for the RSC interaction [63] for comparison. Table D.1 shows that wound integrals for the NSC89 potential are of comparable size to their

Channel		$\kappa^{JS}_{Y'L';YL}$	
Initial	Intermediate	NSC89	RSC
$\Lambda N\ ^1S_0$	$\Lambda N\ ^1S_0$	0.007	0.022
$\Lambda N\ ^1S_0$	$\Sigma N\ ^1S_0$	0.002	—
$\Lambda N\ ^3S_1$	$\Lambda N\ ^3S_1$	0.028	0.031
$\Lambda N\ ^3S_1$	$\Sigma N\ ^3S_1$	0.034	—
$\Lambda N\ ^3S_1$	$\Lambda N\ ^3D_1$	0.028	0.068
$\Lambda N\ ^3S_1$	$\Sigma N\ ^3D_1$	0.094	—

Table D.1: Wound integrals.

nuclear counterparts. These results clarify the importance of the coupling to ΣN states by the strong interaction in the weak decay of the lambda as considered in Chapter 5.

Bibliography

[1] A. L. Fetter and J. D. Walecka. *Quantum Theory of Many-Particle Systems.* McGraw-Hill, 1971.

[2] R. D. Mattuck. *A Guide to Feynman Diagrams in the Many-Body Problem.* McGraw-Hill, 2 edition, 1976.

[3] M. M. Nagels, T. A. Rijken, and J. J. de Swart. *Phys. Rev. D*, 12:744, 1975.

[4] M. M. Nagels, T. A. Rijken, and J. J. de Swart. *Phys. Rev. D*, 15:2547, 1977.

[5] M. M. Nagels, T. A. Rijken, and J. J. de Swart. *Phys. Rev. D*, 20:1633, 1979.

[6] P. M. M. Maessen, T. A. Rijken, and J. J. de Swart. *Phys. Rev. C*, 40:2226, 1989.

[7] T. A. Rijken, V. G. J. Stoks, and Y. Yamamoto. *Phys. Rev. C*, 59:21, 1999.

[8] A. Ramos, A. Polls, and W. H. Dickhoff. *Nucl. Phys. A*, 503:1, 1989.

[9] O. Benhar, A. Fabrocini, and S. Fantoni. *Nucl. Phys. A*, 505:267, 1989.

[10] O. Benhar, A. Fabrocini, and S. Fantoni. *Nucl. Phys. A*, 550:201, 1992.

[11] C. B. Dover, D. J. Millener, and A. Gal. *Phys. Rep.*, 184:1, 1989.

[12] J. Cohen. *Prog. Part. Nucl. Phys.*, 25:139, 1990.

[13] B. F. Gibson and E. V. Hungerford III. *Phys. Rep.*, 257:349, 1995.

[14] W. M. Alberico and G. Garbarino. *Phys. Rep.*, 369:1, 2002.

[15] J. Carlson, V. R. Pandharipande, and R. B. Wiringa. *Nucl. Phys. A*, 401:59, 1983.

[16] H. Lehmann. *Nuovo Cimento*, 11:342, 1954.

[17] B. D. Day. *Rev. Mod. Phys.*, 39:719, 1967.

[18] V. M. Galitski. *Sov. Phys. JETP*, 7:104, 1958.

[19] K. A. Brueckner, C. A. Levinson, and H. M. Mahmoud. *Phys. Rev.*, 103:1353, 1954.

[20] R. V. Reid. *Ann. Phys.*, 50:411, 1968.

[21] E. P. Roth. *Ph.D. Thesis*. Washington University, 2000.

[22] S. Paul and et. al. *Nuovo Cimento A*, 192:379, 1989.

[23] H. T. Bando, T. Matobo, and J. Žofka. *Intern. J. Mod. Phys.*, 5:4021, 1990.

[24] M. Schmidt, G. Röphe, and H. Schulz. *Ann. Phys.*, 202:57, 1990.

[25] E. Feenberg. *Phys. Rev.*, 40:40, 1932.

[26] W. H. Dickhoff, C. C. Gearhart, E. P. Roth, A. Polls, and A. Ramos. *Phys. Rev. C*, 60:064319, 1999.

[27] J. C. Wheatley. *Rev. Mod. Phys.*, 47(415), 1975.

[28] M. Hjorth-Jensen, A. Polls, A. Ramos, and Muther. *Nucl. Phys. A*, 605:458, 1996.

[29] Q. N. Usmani and A.R. Bodmer. *Phys. Rev. C*, 60:055215, 1999.

[30] H. J. Schulze, M. Baldo, U. Lombardo, J. Cugnon, and A. Lejeune. *Phys. Rev. C*, 57:704, 1998.

[31] J. M. Luttinger. *Phys. Rev.*, 121:942, 1961.

[32] B. E. Vonderfecht, W. H. Dickhoff, A. Polls, and A. Ramos. *Phys. Rev. C*, 44:R1265, 1991.

[33] K. Hagiwara et al. (Particle Data Group). *Phys. Rev. D*, 66:010001, 2002.

[34] B. C. Pearce and B. F. Gibson. *Phys. Rev. C*, 40:902, 1989.

[35] B. E. Vonderfecht, W. H. Dickhoff, A. Polls, and A. Ramos. *Nucl. Phys. A*, 555:1, 1993.

[36] A. Polls, A. Ramos, J. Ventura, S. Amari, and W. H. Dickhoff. *Phys. Rev. C*, 49:3050, 1994.

[37] R. N. Silver and P. E. Sokol, editors. *Momentum Distributions*. Plenum, 1989.

[38] P. Fernández de Córdoba and E. Oset. *Nucl. Phys. A*, 528:736, 1991.

[39] E. Oset, P. Fernández de Córdoba, L. L. Salcedo, and R. Brockmann. *Phys. Rep.*, 188:79, 1990.

[40] B. H. J. McKellar and B. F. Gibson. *Phys. Rev. C*, 30:322, 1984.

[41] A. Parreño, A. Ramos, and C. Bennhold. *Phys. Rev. C*, 56:339, 1997.

[42] J. F. Donoghue, E. Golowich, and B. R. Holstein. *Dynamics of the Standard Model*. Cambridge Univ. Press, 1992.

[43] J. D. Bjorken and S. D. Drell. *Relativistic Quantum Fields*. McGraw-Hill, 1965.

[44] Review of Particle Properties. *Phys. Lett. B*, 239:1, 1990.

[45] S. Gasiorowicz. *Elementary Particle Physics*. John Wiley & Sons, Inc., 1966.

[46] G. E. Brown. *Phys. Reports*, 22c(6), 1975.

[47] B. Holzenkamp, K. Holinde, and J. Speth. *Nucl. Phys. A*, 500:485, 1989.

[48] H. Bandō, Y. Shono, and H. Takaki. *Intern. Jour. of Mod. Phys. A*, 3:1581, 1988.

[49] D. Halderson. *Phys. Rev. C*, 48:581, 1995.

[50] M. I. Haftel and F. Tabakin. *Nucl. Phys. A*, 158:1, 1970.

[51] A. Parreño and A. Ramos. *Phys. Rev. C*, 65:015204, 2002.

[52] D. Jido, E. Oset, and J. E. Palomar. *Nucl. Phys. A*, 694:525, 2001.

[53] W. Cassing and et. al. *Euro. Phys. Jour. A*, 16:549, 2003.

[54] Z. Rudy and et. al. *Euro. Phys. Jour. A*, 5:127, 1999.

[55] O. Hashimoto and et al. *Phys. Rev. Lett.*, 88:042503, 2002.

[56] A. Parreño, A. Ramos, C. Bennhold, and K. Maltman. *Phys. Lett. B*, 435:1, 1998.

[57] T. Inoue, M. Oka, T. Motoba, and K. Itonaga. *Nucl. Phys. A*, 633:312, 1998.

[58] A. Ramos, M. J. Vicente-Vacas, and E. Oset. *Phys. Rev. C*, 55:735, 1997.

[59] H. Noumi and et al. *Phys. Rev. C*, 52:2936, 1995.

[60] J. J. Szymanski and et al. *Phys. Rev. C*, 43:849, 1991.

[61] K. A. Brueckner and J. L. Gammel. *Phys. Rev.*, 109:1023, 1958.

[62] B. H. Brandow. *Phys. Rev.*, 152:863, 1966.

[63] P. J. Siemens. *Nucl. Phys. A*, 141:225, 1970.